

**IN-SITU TEM INVESTIGATION OF RAPID
SOLIDIFICATION OF ALUMINUM AND
ALUMINUM COPPER ALLOYS**

by

Kai Zweiacker

Diplom Ingenieur, Technische Hochschule Mittelhessen, 2009

Submitted to the Graduate Faculty of
the Swanson School of Engineering in partial fulfillment
of the requirements for the degree of

Doctor of Philosophy

University of Pittsburgh

2015

UNIVERSITY OF PITTSBURGH
SWANSON SCHOOL OF ENGINEERING

This dissertation was presented

by

Kai Zweiacker

It was defended on

March 27, 2015

and approved by

Jörg M.K. Wiezorek, Ph.D., Professor

Department of Mechanical Engineering and Materials Science

John A. Barnard, Ph.D., Professor

Department of Mechanical Engineering and Materials Science

Jung-Kun Lee, Ph.D. Associate Professor

Department of Mechanical Engineering and Materials Science

Paul W. Leu, Ph.D. Associate Professor

Department of Industrial Engineering

Dissertation Director: Jörg M.K. Wiezorek, Ph.D., Professor

Department of Mechanical Engineering and Materials Science

IN-SITU TEM INVESTIGATION OF RAPID SOLIDIFICATION OF ALUMINUM AND ALUMINUM COPPER ALLOYS

Kai Zwiack, PhD

University of Pittsburgh, 2015

Measuring and observing rapidly evolving interfaces of irreversible transient states such as rapid solidification have been a long time standing problem in materials science as characterization techniques that deliver the necessary requirements, i.e. nanosecond temporal and nano-meter spatial resolution, have not been present. Dynamical TEM utilizes a process initiation photon laser pulse coupled with a timed electron pulse train to observe transient states of rapidly evolving phase transformations. Nanoscale spatio-temporal resolution in-situ TEM revealed growth mode changes and enabled quantitative measurements of locally resolved instantaneous and averaged interface velocities for pure Aluminum and hypo-eutectic Aluminum-Copper alloys. Post-mortem TEM was employed to gain insights on micro-structural evolution morphology regarding texture, morphology changes, grain size and grain size development, phase formation and orientations relationships during the laser processing. Post-mortem TEM studies revealed that resultant microstructures found in thin film solidification are equivalent with microstructures found in bulk sample experimentation utilizing CW-lasers. DTEM allows systematical studies of far-from equilibrium phase transformation and were employed to investigate PL initiated directional rapid solidification in Al and Al-Cu alloys.

Keywords: Rapid Solidification, RS, Dynamical TEM, Diffraction, Aluminum, Al-Cu, Precession Electron Diffraction.

TABLE OF CONTENTS

PREFACE	ix
1.0 INTRODUCTION	1
1.1 Objectives	4
2.0 BACKGROUND	6
2.1 Thin Film Growth by Evaporation	6
2.2 Rapid Solidification	8
2.2.1 Surface Laser Assisted Remelting	12
2.2.1.1 Solidification Microstructure Selection Maps for Al-Cu	13
3.0 EXPERIMENTAL PROCEDURES AND MATERIALS	15
3.1 Preparation of Thin Films	15
3.2 Pulsed Laser Irradiation	15
3.3 Precession Electron Diffraction and the OIM System	18
3.4 Scanning Transmission Electron Microscopy (STEM)	23
3.5 In-situ Irradiation and Observation utilizing Dynamic Transmission Electron Microscopy	24
4.0 RESULTS	29
4.1 Pure Aluminum	29
4.1.1 As-deposited State: Aluminum Thinfilms	29
4.1.1.1 PED Investigation of Thin Films in as-deposited State	31
4.1.2 Ex-situ Irradiation Results of Aluminum Thin films	33
4.1.2.1 PED Investigation of Ex-situ Modified Al Thin Films	38
4.1.3 Insitu TEM Pulsed Laser Irradiation of Aluminum Thin-films	47

4.1.3.1	High Spatio-Temporal Resolution Insitu TEM Observation of Melting and Solidification	47
4.1.3.2	Melting of Aluminum ThinFilms	49
4.1.3.3	Pulsed Laser induced Solidification of Al Thin-Films	61
4.1.3.4	Low Spatio-Temporal Insitu DTEM Observation of Melting and Solidification	64
4.1.3.5	PED Studies of In-situ DTEM PL modified Microstructure	78
4.1.4	Summary and Discussions	85
4.2	Hypoeutectic Al-04Cu alloy	86
4.2.1	As -deposited State: Al-04Cu Thin films	86
4.2.2	In-situ and Ex-situ PL irradiated Al-Cu Thin films	93
4.2.3	PED Studies of the in-situ PL irradiated hypoeutectic Al-Cu Alloy	104
4.2.4	Composition Analysis of the Growth Mode Transition Zone	116
4.2.5	In-situ DTEM PL Irradiation of hypoeutectic Al-Cu Alloy	119
4.2.6	Summary and Discussion	129
5.0	ACHIEVEMENT AND OUTLOOK	132
5.1	Achievement	132
5.2	Outlook	133
	BIBLIOGRAPHY	134

LIST OF FIGURES

2.1	Overview of grain structure evolution during deposition of polycrystalline thin films	7
2.2	Flim growth thin films	9
2.3	Solidification Microstructure Selection Map for Al-Cu alloys	14
3.1	Ex-situ laser melting setup and a typical melt pool, schematic of the ex-situ laser melting setup and an example of the observed resolidified microstructure	17
3.2	Precession Electron Diffraction Setup	19
3.3	Schematics of PED assisted Orientational and Phase Mapping	21
3.4	Demonstration of the possibilities of the the PED OIM	21
3.5	Signal detector setup for a Scanning Transmission Electron Microscope	22
3.6	Dynamic Transmission Electron Microscope	26
3.7	Comparison between Conventional and DTEM image	27
3.8	Pulse Train Approach in the DTEM	28
4.1	Bright-Field (BF) of Aluminum thin films	30
4.2	Inverse Pole Figure of the starting condition	32
4.3	Ex-situ laser melting setup and a typical meltpool	36
4.4	Example cross section of an ex-situ irradiated Aluminum thin film	37
4.5	PED OIM of HAZ and Growth Zone (FN)	40
4.6	PED OIM of HAZ and Growth Zone along heat extraction direction	41
4.7	PED OIM of HAZ and Growth Zone perpendicular to heat extraction direction	42
4.8	HAZ Grain size analysis	43
4.9	PED OIM of the Growth zone	46

4.10	Post-mortem acquired Bright-Field images of an in-situ irradiated thin-film .	48
4.11	Observation of the melting process between -200ns and 1600ns	53
4.12	Observation of the melting process between 1us and 3us.	53
4.13	Observation of the evolving flat solid liquid interface	55
4.14	Observation of the evolving flat solid liquid interface.	55
4.15	Summary of the melt stages of Aluminum thin film.	60
4.16	Observation of the beginning of planar growth in pure aluminum thin-films .	63
4.17	Observation of planar growth near the central region of the melt pool	63
4.18	Observation of the last 660ns of solidification	72
4.19	Specimen setup and proposed irradiation locations	73
4.20	Solidification sequences	74
4.21	Summary of the 2.6us images for different locations	75
4.23	Velocity evaluation for the experimental observation in Figure 20	77
4.24	PED investigation of zone 1,2 and 3	79
4.25	Investigation of the growth zone of in-situ irradiated Al thin film	81
4.26	Grain size evaluation of the HAZ	83
4.27	Grain size evaluation of the HAZ (statistics)	84
4.28	Bright Field observation Evaporated Alloy Film	88
4.29	Annular Dark Field image and EDS of the alloy film	90
4.30	PED OIM scan of the starting condition	92
4.31	Texture analysis of the Starting condition	92
4.32	Comparision between in-situ and ex-situ irradiated resulting Microstructures	100
4.33	Grain size analysis of HAZ	101
4.34	Statistics for individual evaluated segments of Figure 4.33	102
4.34	... continued	103
4.35	PED results of HAZ	106
4.36	Texture analysis of HAZ	108
4.37	PED of grain in the growth zone (lower spatial resolution)	110
4.38	PED of grains in the growth zone (higher spatial resolution)	113
4.39	PED image of the Left Grain	114

4.40	PED image of the Right Grain	115
4.41	EDS of the transition between Zone 1 and Zone 3	118
4.42	Low Spatio-temporal resolution DTEM observation and resulting velocity plot	122
4.43	High spatio-temporal observations of occurring growth mode changes	128

PREFACE

I would like to thank my advisor, Dr. Jörg Wiezorek, for taking me on as one of his graduate students for the endless patience, inspiration, and confidence he provided. Thanks given to Dr. Bryan Reed, Dr. Thomas LaGrange, and Dr. Joseph McKeown for the extraordinary opportunity to experience the forefront of ultra-fast electron microscopy and materials science. I also want to thank all of my group members and all the friends I have made while at the University of Pittsburgh for their support and encouragement. Further, I want to thank everyone back home for their love and support throughout this experience, especially my family: Anneliese and Erik. Finally, I want to thank Kelsey for sticking by me through the final stages of this demanding endeavor. I love you all very much.

1.0 INTRODUCTION

Electron microscopy has had a tremendous effect on our understanding of materials. By exploring the processing - structure - properties - performance links down to the Ångstroem level it is now possible to modify microstructures of many materials to obtain a desired set of properties [1]. Conventional transmission electron microscopy (CTEM) can provide almost all structural, phase, and crystallographic data that allows us to establish microstructure based understanding of processing-structure-property-relationships. The newly developed Dynamical Transmission Electron Microscope (DTEM) allows us to probe by direct observations transient states of irreversible transitions, including phase transformations. The DTEM enables acquisition of TEM images or diffraction patterns with nanoscale spatio-temporal resolution [2]. Solidification is one of the fundamental processes in materials fabrication, especially as it concerns metal and alloys of metallic elements. The mechanisms and the parameters affecting it, such as temperature distribution, heat extraction rates and alloying content, determine the resultant microstructure and properties. Solidification processes under near equilibrium conditions, e.g. as in typical casting operations, have been studied extensively and are very well understood both regarding practices in production and regarding associated theory development. However, establishment of truly predictive models and detailed theoretical understanding of solidification processes under far-from-equilibrium, driven conditions, e.g. as in rapid solidification RS processing, is still an on-going effort with competing models being discussed in the recent literature [3, 4, 5, 6, 7]. Partly, the development of theory and empirical models is hampered by the lack of experimental data and observations that can be used for validation. The DTEM offers nanoscale spatio-temporal resolution in the range of micrometers to nanometers and microseconds to nanoseconds and appears to be uniquely suitable to address the apparent need for experimental data on the

dynamics and structural details of the transformation interface responsible for the formation of the microstructures in metals and alloys under rapid solidification conditions. The rapid extraction of thermal energy including latent heat and super-heat, during the transition from liquid to solid can cause high undercooling as high as $\approx 100K$, leading to cooling rates and solidification behavior that deviates from known more general casting methods. Heat extraction rates greater than $10^4 K/s$ permits large deviations from equilibrium and the occurrence of various meta-stable effects that can be categorized as being constitutional or microstructural. Rapid Solidification (RS) of alloys offers advantages over conventional solidification processing, such as extension of solid-liquid solubility, enhanced composition flexibility, formation of non-equilibrium crystalline phases from the melt through alternative phase selection pathways, allowing the incorporation of desirable second-phase dispersoids, particles or phases. It is even possible to retain disordered crystalline structures in normally ordered materials and inter-metallic compounds. Typically desired changes in grain morphology, refinement of features, such as grain shape and size, can be accomplished. Under extreme conditions of high heat extraction rates and high undercoolings, growth at solid-liquid interfaces can be essentially barrier-less, limited only by the kinetic attachment of atoms to the growing solid phase or phases. Solidification front velocity and interface morphology determine the defect concentration, grain size, and morphology of the solidification microstructure [8]. Solidification processing in general is important step in the fabrication of metals and alloys, which are used in engineering components and systems for application in electronic, electro-magnetic, and electro-optical micro-devices, as well as bio-medical, petrochemical, energy, and transportation technologies RS enables synthesis of materials with unique properties. Numerous RS processing methods have been developed to produce the required high rate of transformation and have become a compelling set of fabrication techniques [9]. Hence, the growth dynamics during and the micro-structures established in RS processed materials are scientifically interesting and technologically important. The basic criterion that governs classification of a given fabrication path as a RS processing method is based on the presence of common physical features among the different phases encountered in the resulting material, while the most pertinent unifying feature common to all RS processes is rapid heat extraction, which drives transformation to very high rates.

Conditions suitable for RS are accomplished by utilizing very effective heat sinks or highly under-cooled melts. In prior experimentation on RS processes, typically either high temporal or high spatial resolution had to be selected. Empirical studies of rapid phase transformations is inherently difficult due to the combination of extremely fast transformation front velocities (1-10m/s) and resulting meso-scale features of the evolving solid. Rapidly evolving meso-scale features require experimental setups that can capture material processes with very high temporal and spatial resolution. To date most available characterization techniques offer either excellent temporal resolution (e.g. X-Ray techniques) or excellent spatial resolution (e.g. electron beam based techniques, SEM or TEM). Therefore, it has proven difficult to observe RS processes on the sub-micron length scale with the sufficient temporal resolution. As a result, validation of nanoscale predictions from computer modeling or theory, which now can treat small but significant volumes at the times scales comparable to those of some ultra-fast transformations remain difficult [10]. Given the unique spatio-temporal resolution offered by the DTEM instrumentation it appears warranted to explore its use for in-situ experimentation for the study of to date inaccessible aspects of RS transformations in metals and alloys. In order to overcome problems associated with the inherent trade-offs between spatial and temporal resolution of prior experimental studies of RS, here, in this investigation the unique dynamic transmission electron microscope (DTEM) will be used to facilitated observations, measurements and discovery with unprecedented nanoscale spatio-temporal resolution. The study of RS phenomena in metals and alloys in response to pulsed laser processing is compatible with the probing by the imaging or diffraction information providing electron beam of the DTEM. The transformation phenomena expected to be induced by the pulsed laser (PL) irradiation of the metals and alloys include the photon induced initial melting and subsequent solidification. Thin films are the ideal specimen for the experimentation proposed here, namely PL processing and combined dynamic in-situ TEM and post-mortem TEM analyses. The use of electron beam transparent thin film geometries allows direct observation of the response of the materials to PL irradiation with appropriate nanoscale spatio-temporal resolution by state of the art in-situ TEM experiments. Capturing the kinetics of the microstructural evolution by direct observation based measurements will yield information on the solidification front velocity that can be directly correlated with its

morphology and changes thereof, compositional gradients, grain size, grain orientation and defect concentration. Recording such unique data sets under different conditions would facilitate determination of processing-structure relationships, which could be extended to include properties as well by additional property measurements. For this first study of PL induced RS processes in thin films using the DTEM and post-mortem TEM Aluminum (Al) and Aluminum-Copper (Al-Cu) alloys are selected, because considerable literature exists on RS processing in these systems for comparison and benchmarking [11, 12, 13]. Thus, this study will provide experimental observation and measurements that cannot be obtained otherwise. Furthermore, this study will contribute to the development of experimental in-situ TEM techniques to study transient phenomena at the nano-scale, which will allow development of direct observation based understanding of thermally activated rapid phase transitions in metallic systems.

1.1 OBJECTIVES

This study aims to develop and establish an experimental approach to investigate thermally activated rapidly evolving phase transformation phenomena utilizing as key instrumentation the dynamical in-situ TEM (DTEM). This study delivers the experimental setup and methodology to obtain reproducible results of laser pulse initiated rapid solidification in pseudo free-standing and electron-beam transparent metal thin films. DTEM will capture real-space images of the details on the melting and solidification of Al and Al-Cu alloys. This promises to provide experimental data and insights to support validation and corroboration of theoretical and modeling predictions related to the transient phenomena occurring under extreme conditions of high transformation rates. Establishing the methodologies suitable for in-situ TEM experimentation of these irreversible transition phenomena represents a pioneering effort in condensed matter and alloy transformation related science and engineering. More specifically, objectives of this study include the following items:

- Evaluate whether thin film based PL induced rapid solidification in free standing metal thin films is feasible.

- Evaluate the potential equivalence of the microstructures evolving in RS processed thin films that are suitable for DTEM experiments and those microstructures reported for RS processed bulk form alloys.
- Direct observation of the morphology, morphology evolution, measurements of the velocity and velocity evolution of the liquid-solid interface for Al and Al-Cu alloys.
- Direct observations of solid-state transitions subsequent to the rapid solidification completion in the different metal and alloy thin films.
- Determine the role of key microstructural parameters of the as-deposited condition of the nanoscale metal and alloy thin films in terms of crystal orientation, texture, grain size, composition and solute segregation which might influence details of the rapid solidification process and resulting microstructures.
- Determine the velocity functions for the transformation interface to predict growth mode changes.
- Observe the growth mode changes predicted by prior work [13] and gaining insights on the kinetics of the interface utilizing the high spatio-temporal resolution DTEM instrumentation and experimental methods developed here

2.0 BACKGROUND

2.1 THIN FILM GROWTH BY EVAPORATION

Dual electron beam evaporation was utilized to deposit high purity metal and alloy thin films onto Si_3N_4 -substrates. In the used evaporation configuration electrons are thermally emitted from a heated filament that is shielded from direct line of sight of both the evaporant and substrate. The cathode potential is biased negatively with respect to a nearby grounded anode and serves to accelerate the electrons. A transverse magnetic field is applied that serves to deflect the electron beam in a 270° circular arc and focus it on the hearth and evaporator charge at ground potential. The vapor can be approximated as a high-pressure viscous cloud of very hot evaporant. The complex energy transfer between electronic excitation and translational motion of vapor atoms leads emitting of atoms from the dense high pressure cloud towards the substrate. The vapor atoms transverse towards the substrate and a progression of events that starts with the condensation of isolated atomic clusters on a bare substrate, continues with film thickening due to additional deposition, and ends with fully developed epitaxial single-crystal, polycrystalline, or amorphous films and coatings. Figure 2.1 displays the fundamental process on how the grain structure of a poly crystalline thin film develops during the stages of the film formation. Once formed, nuclei grow into the external phase, as well as laterally in directions lying in the plane of the interface. Lateral growth kinetics will lead to impingement and coalescence (Fig. 2.1b) of crystals, ultimately resulting in the formation of grain boundaries and defining the initial grain-structure characteristics of the newly formed thin-film (Fig. 2.1c2.1d). If grain boundaries are mobile, the grain structure continues to evolve during film thickening. This often results in a more equiaxed structure in which the in-plane grain size tends to be approximately the same as and scale with the film

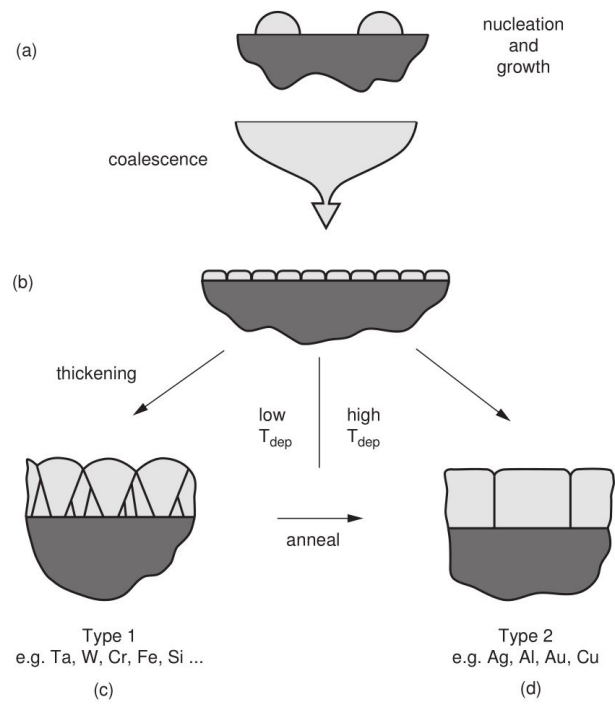


Figure 2.1: Overview of grain structure evolution during deposition of polycrystalline thin films

thickness, resulting in structures in which most grain boundaries are through the thickness of the film, schematically illustrated in Figure 2.1d, the average in-plane grain size is uniform. Very often polycrystalline films exhibit a crystallographic texture, in that the crystals from which they are composed tend to have specific crystallographic directions normal to the plane of the film. For example, it is common for films of fcc-metals to have a preferred crystallographic orientations where the $\{111\}$ planes are parallel to the plane of the film. In this case the films exhibit a $\{111\}$ texture. The distribution of grain orientations is affected by all the processes that affect grain size and is also strongly affected by processing techniques and conditions.[15]

2.2 RAPID SOLIDIFICATION

Laser induced melting and subsequent rapid solidification (RS) of thin foils differs greatly from equilibrium solidification processes. Figure 2.2a shows the geometrical layout used in this investigation. Fig. 2.2b-2.2d shows an idealized solidification process and temperature development which creates a setup for lateral rapid solidification. A single excimer laser pulse with ≈ 28 ns duration is applied to thermally stimulate a sample. The energy is sufficient enough to melt a uniform thin region of the specimen. After termination of the photon pulse solidification starts at the edge of the melt pool and continuous laterally towards the center. The result is a solidification morphology formed with an initially zero velocity but accelerated towards the center. The S-L interface moves laterally towards the center. During this process the heat from the melt pool is transported away from the S-L interface and heat of crystallization is released at the interface, so that super- and under-cooling of the melt can occur. The interface velocity will behave according to the RS relationship: [16, 17]

$$v_{interface} \approx \mu(T_{interface} - T_m) = \mu\Delta T_{undercooling} \quad (2.1)$$

Rapid solidification will terminate when the opposing solidification fronts consumed all melt and meet in the central region of the melt pool leaving a heavily changed microstructure behind. With the shown setup it is possible to achieve high cooling rates ($10^3 K/s$) that allow

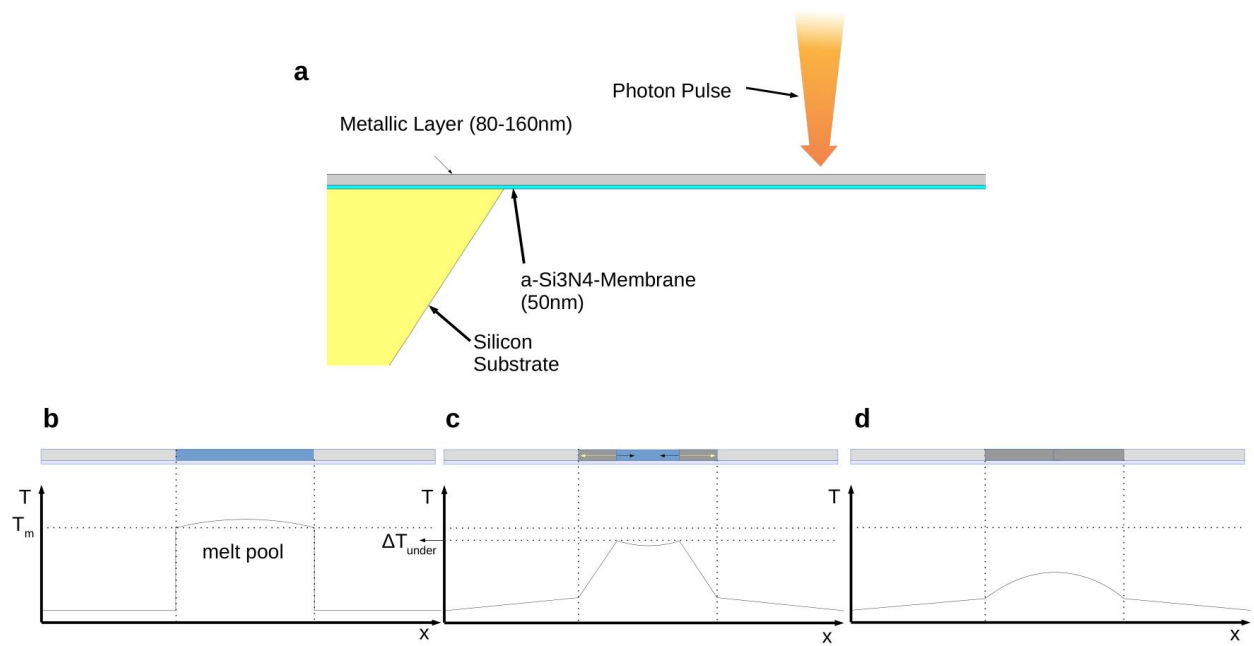


Figure 2.2: **a** geometrical layout for in-situ and ex-situ irradiation experiment "almost" free standing metal film, **b-c** meltpool development leading to directional rapid solidification

high solid- liquid interface velocity ($v_{SL} > 0.01m/s$) and large thermal gradients ($10^{12}K/m$). These conditions alter the physics with respect to those established for equilibrium solidification processes (i.e. atomic redistribution near the interface) and non-equilibrium phases can form as a result of being favored kinetically over equilibrium phases. This can result in constitutional changes and differences in morphology and scale of micro-structures resulting from rapid solidification. In a multi component solidification process the phase selection, growth velocity, chemical compositions, long and short range order, and micro-structure of a growing phase, is highly dependent on the local conditions at the crystal-melt interface, which are temperature, composition, orientation, curvature and interface structure. Kinetic models have been proposed to develop understanding of these dependencies and assist with materials development and production and ultimately to predict micro-structures under near-equilibrium as well as non-equilibrium conditions. At slow solidification rates, the assumption of local equilibrium at the crystal/melt interface is valid. However, local equilibrium at the interface is not maintained during rapid solidification [18], for which models of non-equilibrium interface kinetics are proliferate but definite measurements required for validation of theory and models are rare. Substantial deviations from local equilibrium for solidification set in as the interface approaches the diffusive speed v_D – the ratio of the diffusion coefficient across the interface to the inter-atomic spacing.[19] Diffusive speeds are on the order of $10m/s$ [19, 20] For two component alloys the non equilibrium interface response functions [21] predict the mole-fraction of solute X_s (Composition) of the growing solid and the velocity v_i of the interface in terms of the interface temperature T_i and composition of the liquid at the interface X_l . For dilute alloys the velocity function becomes indistinguishable from that of the pure solvent [22] and the solute trapping function can be described by a velocity dependent but temperature and composition independent ratio, the solute segregation coefficient $k = X_s/X_l$. In this limit the solute trapping function has been measured extensively [23]. However, in non-dilute alloys the velocity function is unresolved or only partially defined. Some experiments, i.e. transient conductance and reflectivity measurements or laser drag experiments have been employed to measure average interface velocities. Disregarding growth-mode change or are only suitable for specific set alloys e.g. *AlSi*. A more general characterization technique has not been established yet. For model-

ing of solidification micro-structures reliable phase diagram information is essential but not sufficient, phase equilibria and transformation kinetics need to be determined, understood and included in calculations. In case of rapid solidification the movement of the interface approach is the most important variable and determination is crucial. Other phenomena such as the inter-facial under-cooling, the extension of solubility and the stability of a planar interface are explicit functions of the velocity. Pure Metals usually solidify with an atomically rough interface and the velocity-under-cooling function in the low velocity regime is fitted linearly by a temperature dependent kinetic coefficient.

Most models attempt to extend the velocity-under-cooling function towards the non-linear high velocity regime as well as towards alloys. This relation has been extended to alloys using a sharp interface and continuum models. The sharp interface models include the Aziz-Kaplan or continuous growth model (CGM) with and without solute drag [24] as well as the Ågren [25] model, continuum approaches include the Hiller-Sundman (H-S) [26, 27] and the Baker models [28].

Continuum growth mode models and other sharp interface models describing the main interface response functions of a two component system by two inter-dependent interface response functions. One is the interface partition coefficient and the other the interface velocity.

$$X_s^i = k_e(v, X_L^i, T_i)X_L^i \quad (2.2)$$

$$k_e = \frac{X_S}{X_L} \quad (2.3)$$

$$v = v(v, X_L^i, T) = v_0[1 - \exp(\frac{-\Delta G}{RT})] \quad (2.4)$$

Both functions depend strongly on temperature (T), solute content in the liquid (X_L^i) and solute content in the solid (X_S^i). The development of numerous time-resolved measurement technique has permitted the quantitative analysis of melting and solidification process. [29, 30, 31] State of the art measurement of interface velocities utilize the transient conductive technique which measures the changing transverse electrical resistance of a thin-film on an insulating substrate during a laser introduced re-solidification process. Alternatively, surface laser remelting studies have been conducted which permit control of external velocity of the

laser relative to the specimen surface (velocity of the heat source or beam v_b). Subsequent, post-mortem, characterization of the solidification microstructures enables evaluation of the solidification or crystal growth velocity. [32]

2.2.1 Surface Laser Assisted Remelting

Alternatively, it is possible to deduce growth velocities from post-mortem micro-structural characterization of alloy and metal specimen after laser induced bulk surface remelting. Such treatments utilize high-energy laser or electron beams that are continuously irradiating a surface region of a sample of typically bulk form. The sample is moved relative to the stationary beams at an adjustable velocity v_b . In surface resolidification, the local growth rate can be obtained by careful inspection of the microstructural features longitudinal sections through the center-line of the remelted trace. Specifically, quantitative measurement of the orientation of the directionally solidified grains in the resolidified microstructure permit correlations of the apparent local crystal growth rate v_c to the externally imposed relative beam displacement velocity v_b . The microstructure in the central region of the re-solidified volumes tends to be perpendicular to the local solid-liquid interface, with respect to the direction of beam displacement. The relationship between the beam displacement rate v_b and the local growth rate v_s is defined by

$$v_s = v_b \cdot \cos(\Theta) \quad (2.5)$$

This experimental approach to rapid solidification related microstructure evolution studies has also some disadvantages. The laser assisted surface remelting approach explored very successfully in a set of previous studies based entirely on post-mortem microstructural inspections and measurements. While the externally controlled parameters, such as the laser power density and relative beam displacement rate, v_b are quite well controlled, measurements of the v_c derived from the microstructural post-mortem characterization are associated with uncertainty of 20% to 30%. Furthermore direct observation of the crystallization solidification interface morphology are not possible. Hence, while changes in the growth mode during alloy rapid solidification can be determined from their signatures in the resulting re-solidified volumes, correlating them with velocity change is difficult and mechanistic details

rely heavily on speculations. This approach was used to create Solidification Microstructure Selection Maps (SMSM) for the Al and Al_2Cu system and the result will serve as the benchmark for the here presented investigation.

2.2.1.1 Solidification Microstructure Selection Maps for Al-Cu A microstructure is defined by the phases and growth morphologies. Depending on the alloy composition, temperature gradient and growth rate, stable or meta-stable phases may develop in the form of various growth morphologies, such as plane front, cells, or dendrites of single-phase material or multi-phase eutectic micro-constituent. The transition from one phase to another or from one growth morphology is essentially a lowest free energy / phase-stability problem and quantification of such non-linear phenomena are not present. However, a heuristic approach has been successfully applied to predict microstructural selection and the results are summarized in Fig. 2.3. For directional growth Aluminum Copper alloys in laser assisted remelting the phase and morphology which, under a given local solidification condition grows at the highest temperature is the preferred one. Figure 2.3 shows an experimentally determined microstructure selection map for the Al- Al_2Cu system from Gill and Kurz [33].

This present study set out to investigate Al-04 at. %Cu (i.e., Al-09 wt. %Cu) alloys. The microstructure found typically consists out of α -cells, arising from low interface velocities, and bands, consistent of dendritically grown precipitate free supersaturated solid solution α -phase (light) bands and precipitated planar grown (dark) bands, when the critical velocity of $v_a = 2ms^{-1}$ is surpassed.

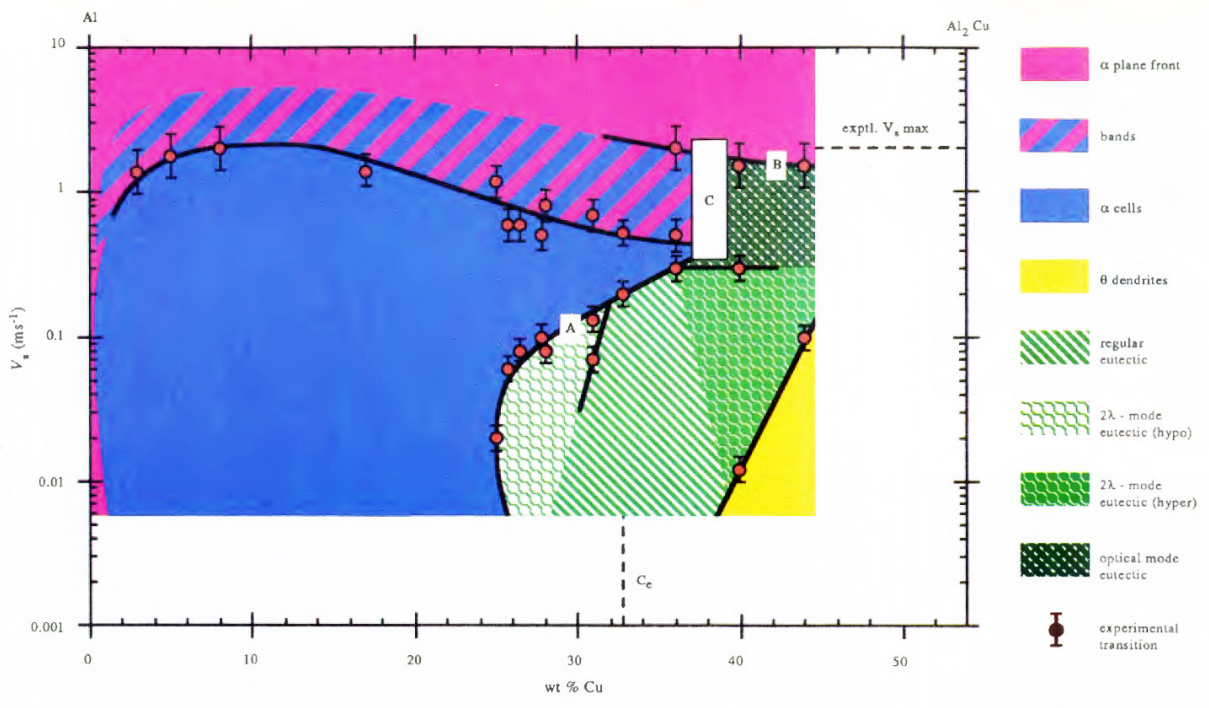


Figure 2.3: Solidification Microstructure Selection Map for Al-AlCu alloys

3.0 EXPERIMENTAL PROCEDURES AND MATERIALS

3.1 PREPARATION OF THIN FILMS

A dual electron beam evaporation system (Pascal System) was used to deposit Al-04 at. %Cu thin films. Al (99.999%) and Cu (99.999%) as source materials are located in two individual crucibles. Silicon Nitride Support Film TEM Grids from Ted Pella, Inc were used as substrates. During deposition, the chamber pressure was set to be below $5 \cdot 10^{-8}$ Torr and the substrate temperature at $\approx 25^\circ\text{C}$. The Cu concentration in the deposited films was controlled by adjusting the electron beam current for the Cu crucible while the electron beam current for Al crucible was kept constant. The chemical composition of the films was measured utilizing a JOEL TEM 2100F equipped with a Gatan EDAX detector. A surface profilometer was used to measure the thickness of the Films.

3.2 PULSED LASER IRRADIATION

With the ex-situ setup samples can be irradiated with a single pulse from a 248 nm (*KrF*) excimer laser, projected through a single-slit *Cu*-mask with a five times demagnification. The mask is used to define the shape and dimensions of the laser beam at the sample and thus the size of the resulting melt pool. A very small central area of the laser beam profile emitted by the *KrF*-excimer system is selected and ensures a highly uniform energy profile. The laser projection system is configured to provide localized and complete melting of metal thin films over area approximately $40\mu\text{m}$ wide and $130\mu\text{m}$ long. With termination of the pulse, the liquid cools and directional solidification commences with quenching rates of about 10^7

– $10^{10}K/s$. The sample can be irradiated while being held at different temperatures ranging from $-170^{\circ}C$ to $500^{\circ}C$. This varies the heat extraction rates. The ex-situ experimental setup and a typical melt pool of a $Al-07at.\%Cu$ thin film irradiated at room temperature is shown in Fig. 4.3.

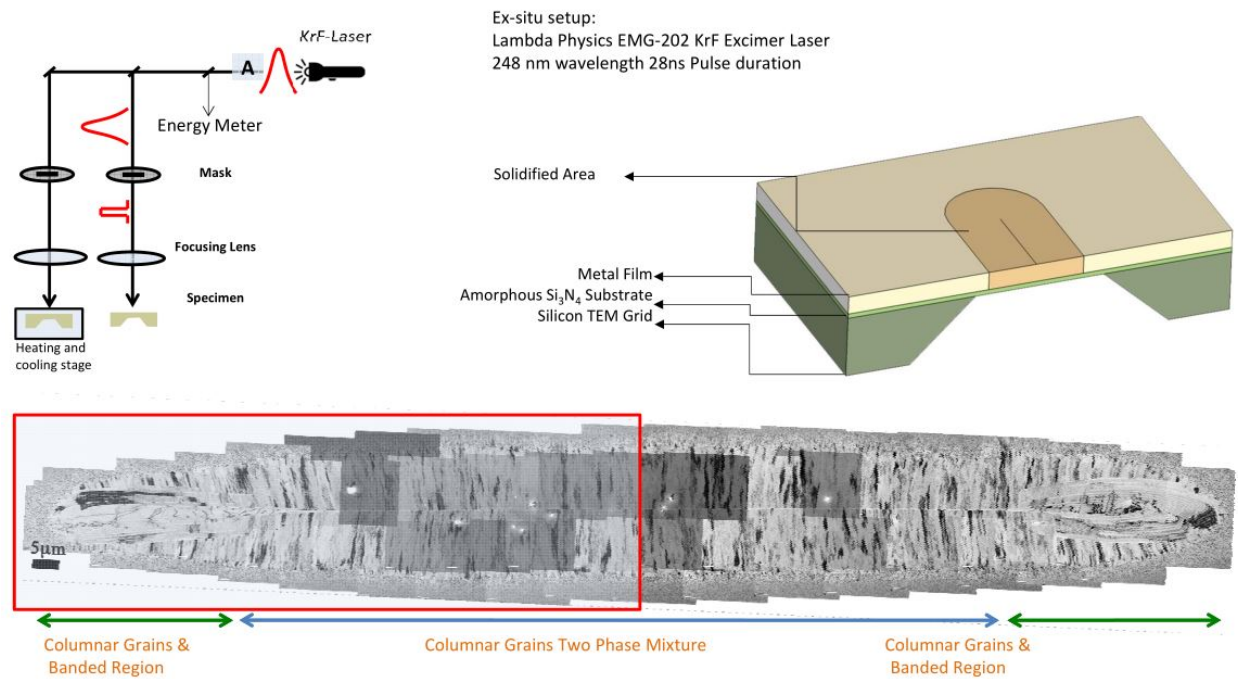


Figure 3.1: Ex-situ laser melting setup and a typical melt pool, schematic of the ex-situ laser melting setup and an example of the observed resolidified microstructure

3.3 PRECESSION ELECTRON DIFFRACTION AND THE OIM SYSTEM

Precession electron diffraction is a new promising technique for electron diffraction pattern collection under quasi-kinematical conditions (as in X-Ray diffraction [34]), which enables “ab-initio” solving of crystalline structures of nanosized crystals. The precession electron diffraction techniques can be used in an TEM instrument operated at 200 *kV*. This new technique can be used for high magnification ultra-fast mapping of variable crystal orientations and phases, similarly to what is achieved with the Electron Back-scattered Diffraction (EBSD) technique in a Scanning Electron Microscope (SEM). In contrast to conventional TEM DF imaging, where a parallel incident beam is used (Fig. 3.2), PI-HCDF imaging uses a converged and precessed beam for illumination of the specimen in the TEM (Fig. 3.2). Computer controlled precession illumination is realized with the help of the ASTAR precession tool by Nano-Megas, which uses the condenser lens system to precess a spread (for PI-HCDF imaging) parallel incident beam with angles up to 4.7°. The system uses the condenser lens shift deflectors (CL A1) to deflect the beam away from the optical axis. The deflection amplitude dialed in with the CL A1 determines the maximum precession angle. The condenser tilt deflectors (CL A2) are used to realign the precessed beam with the optical axis of the TEM instrument. In an ideally aligned state the principal axis of the precession cone of illumination coincides with the optical axis of the microscope and the apex point is on the sample surface. The interaction with the sample gives rise to an intermediate hollow cone diffraction ring, the precession system uses the objective lens shift deflectors OL SD to focus the rings into a pseudo kinematic diffraction pattern. The PED patterns possess more reflections than the acquired images from CTEM (SAED or NBED) and contain more crystal structure information. The enhanced structural information content is caused by a superposition of a multitude of individual recorded diffraction patterns that differ from each other by their primary electron beam direction within the hollow illumination cone of the diffraction geometry, Fig. 3.2. The NanoMEGAS system combines scanning with the collection of precession illumination diffraction pattern and matching which results in a system similar to orientation imaging microscopy in the SEM EBSD but in the TEM. With this system electron diffraction spot patterns are collected sequentially with an ultra-fast optical

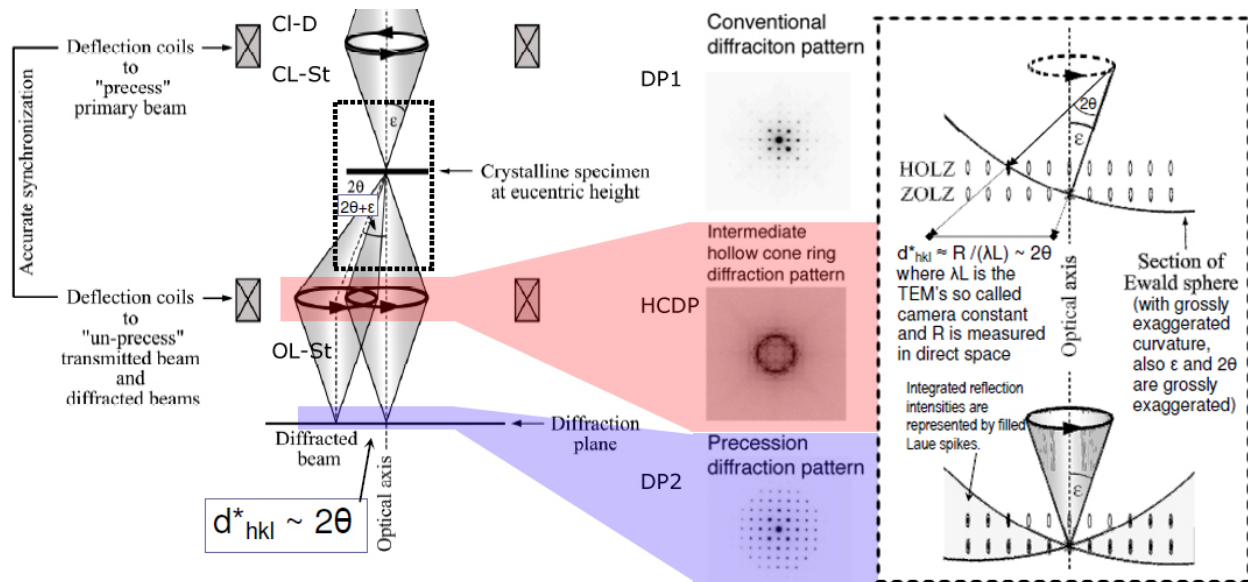


Figure 3.2: Setup of precession electron diffraction: Direct space representation of the PED mode. The dash-boxed area around the specimen is shown in reciprocal space on the far right. DP1 shows difference in intensities due to dynamical effects, these effects are minimized by this method, the diffraction pattern collected is pseudo kinematical DP2 [35]

CCD camera (Fig. 3.3) while an area on the sample is simultaneously being scanned by the TEM focused electron beam, which is also being precessed around the direction of incidence at each point. Beam scanning and precessing is controlled by a dedicated external device, which also allows control of beam pivot points and de-scan pivot points. The external ultra fast optical CCD camera, with 8 bit dynamical range and 250x250 pixel image size, mounted in front of the TEM screen is used for the diffraction pattern image collection. This camera records the rapidly changing patterns appearing on the fluorescent screen of the TEM and is the key to a high collection speed since it may work as fast as 180 frames/sec, although fluorescent screen remanence slightly slows down this performance. During the scanning and precessing of the primary electron beam, thousands of ED spot patterns are recorded and stored in the memory of a dedicated computer [36]. In order to proceed with nanocrystal orientation and/or phase identification, each one of the experimental ED spot patterns is compared to one or several sets of computer generated ED spot patterns, also referred as templates. The software technique for the comparison is based on optimal template matching using cross-correlation (Fig. 3.3). A TEM Microscope fitted with a Field Emission Gun can achieve spot sizes of $4nm$, considering a recommended step sizes of $2nm$ is very feasible, thus identifying features of $10 \times 10nm$ size using the TEM OIM is possible. Template generation is done on the basis of unit cell dimensions and geometry as well as inherent atomic positions, for each of the known phases present in the examined sample. Using this data a complete spatial set of ED spot patterns is generated under purely kinematical conditions. The comparison of these templates with experimental ED spot patterns is run searching a maximum match for spot positions and their relative intensities, and the parameter quantifying the match is called the correlation index. Figure 3.4 shows the possibilities of the TEM OIM system, the regular TEM BF image shows the microstructure and the TEM OIM reveals the orientations of the crystallites.[37] The orientation image in Fig. 3.4b shows grains in the order of $200nm$ as well as grains in the order of $20nm$.

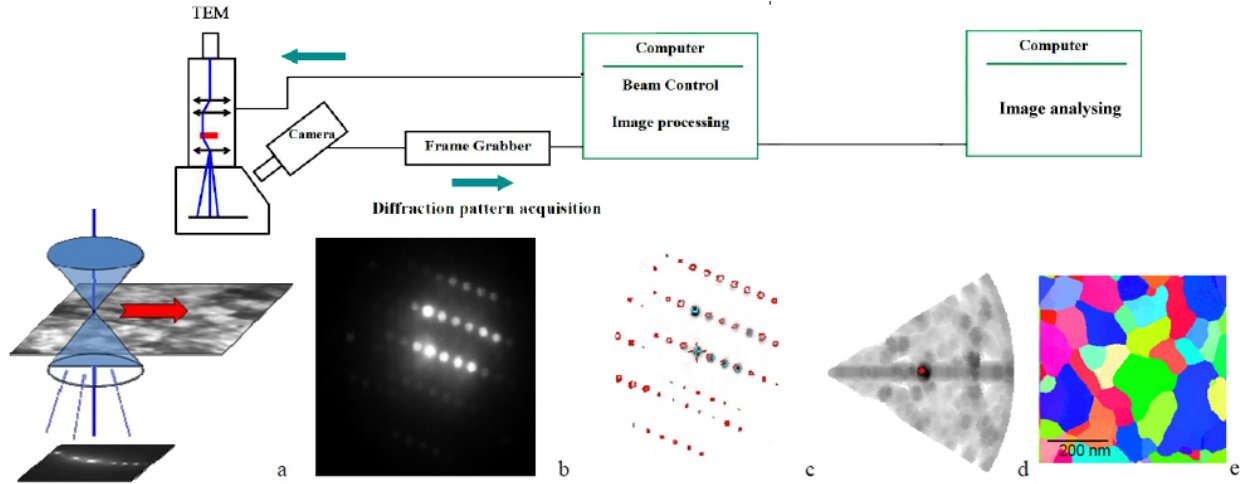


Figure 3.3: Schematics of PED assisted Orientational and Phase Mapping: **a** beam scanning with DigiSTAR over a user-defined sample area combined with precession **b** experimental spot PED pattern serial recording in computer memory **c** superposition of individual ED template (red dot pattern) which best matches experimental PED pattern (grey dot pattern), and **d** orientation directional map with grey intensity plot of matching index for the experimental spot PED pattern. [37, 35]

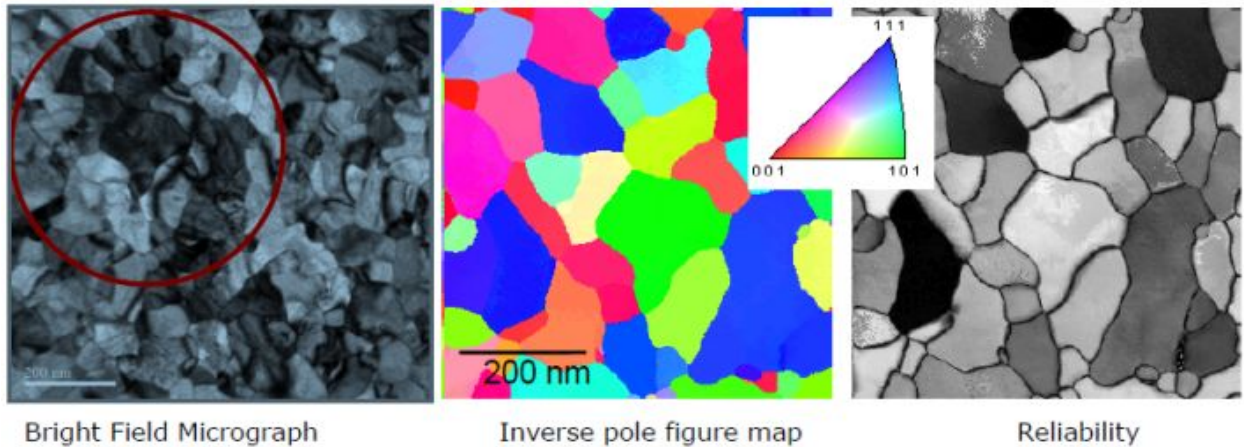


Figure 3.4: Demonstration of the possibilities of the the PED OIM system: **a** CTEM image of nanocrystalline tungsten **b** TEM OIM image for a sample area **c** reliability map **d** orientation stereographic triangle [37]

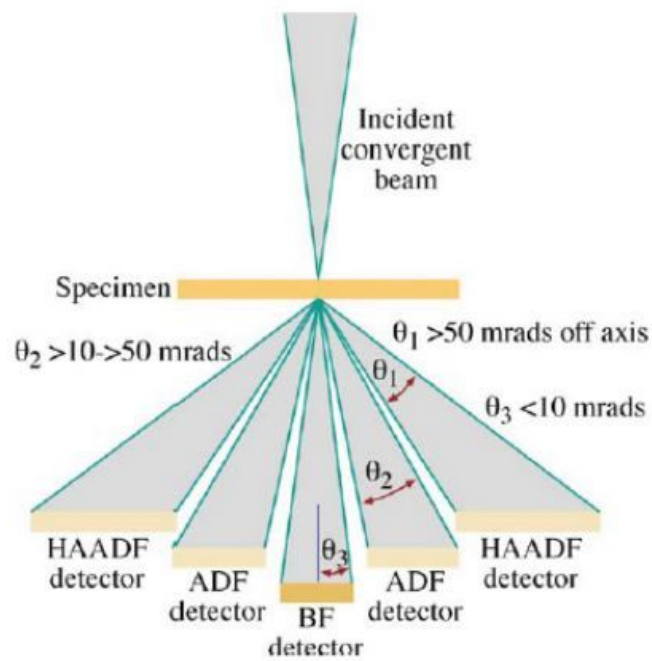


Figure 3.5: Signal detector setup for a Scanning Transmission Electron Microscope

3.4 SCANNING TRANSMISSION ELECTRON MICROSCOPY (STEM)

STEM is distinguished from conventional transmission electron microscopes (CTEM) by focusing the electron beam into a narrow spot which is scanned over the sample in a raster. The rastering of the beam across the sample makes these microscopes suitable for analysis techniques such as mapping by energy dispersive X-ray (EDX) spectroscopy, electron energy loss spectroscopy (EELS) and annular dark-field imaging (ADF). Fig. 3.5 shows the converged beam specimen interaction. These signals can be obtained simultaneously, allowing direct correlation of image and quantitative data. To use the different imaging modes in a TEM, as well as in a STEM one needs brief understanding of contrast formation, for this research the mass-thickness contrast and diffraction contrast formation are needed. Both contrasts are forms of amplitude contrast. Both arise because of electron interaction with the specimen, namely scattering. The interpretation of mass-thickness contrast is simple in comparison to diffraction contrast. Some characteristics of mass-thickness contrast are:

1. Areas of greater Z or greater specimen thickness (t) scatter electrons more strongly, and therefore appear dark in BF imaging and bright in DF images
2. TEM mass-thickness contrast images are of better quality (lower noise and higher resolution), digital STEM images can be processed to show higher contrast than analog images
3. STEM mass-thickness contrast images are most useful for thick or beam sensitive specimens
4. Z-contrast (HAADF) images can show atomic-level resolution for very thin specimens

The diffraction contrast characteristics can be summarized:

1. Diffraction contrast arises when the electrons are Bragg scattered
2. To form a diffraction-contrast image in TEM the objective aperture selects one Bragg scattered Beam. Often the STEM detectors gather several Bragg beams which reduce diffraction contrast
3. Diffraction-contrast images in STEM are noisier than CTEM Images

Z-Contrast images (high- angle annular dark-field, HAADF) are formed from incoherent elastically scattered electrons. The scattered intensities and the forming contrast can be understood as a sum of independent scattering events from individual atoms. Z-Contrast images are formed by collecting high-angle (75-150 mrad) elastically scattered electrons with an annular dark-field detector, this detector captures sufficient intensities to provide an efficient dark-field imaging mode. Although incoherent, the high angle scattering is nearly elastic. Owing to its high δk , however, it does involve "multi-phonon scattering" involving small energy transfers to phonon's. In order to be scattered nearly elastically at high angle, the high-energy electron must pass close to the nucleus. These electrons are scattered at high angles because of their interaction with the nucleus of the atoms. These kind of interactions are described by Rutherford scattering of electrons produced by the nucleus, which follows, approximately, a Z^2 dependence. These scattered electrons hold compositional information through the Z-dependence of the scattering cross section. Thus, BF and DF STEM images contain Z-dependent information and atomic-resolution compositional maps can be generated.

3.5 IN-SITU IRRADIATION AND OBSERVATION UTILIZING DYNAMIC TRANSMISSION ELECTRON MICROSCOPY

The DTEM at LLNL combines a standard JOEL 2000FX TEM with two laser systems (see Fig. 3.6). The column of the TEM has been modified to allow laser access to the sample and the photo cathode. The DTEM can operate in a single-shot sequence as well as in pulse train mode. The Laser system is divided into two segments which allows creation of two separated and time delayed events. In the single shot mode, a 10 ns full-width at half-maximum (FWHM) specimen-pump laser pulse (Nd:YAG laser with $\lambda = 1064$ nm) incident at a 45° angle illuminates an area on the electron transparent sample, providing a thermal stimulus with heating rates up to 1000 K/s. Thus, a sample drive laser pulse can be used to melt the metal or alloy thin film. The second event starts with a user-controlled time delay as short as 15 ns, by the use of the cathode drive laser (Nd: YLF laser with fifth

harmonic, 11 nm; 10 ns FWHM). The cathode drive laser photo-excites a 15-50 ns FWHM electron pulse from the laser-pulse-driven photo cathode. Each electron pulse emitted from the photo cathode has a total charge greater than $10^9 e^-$ and thus an instantaneous current of 10 mA ensuring the rose criterion for a contrast forming image [2]. The electron pulse is used to either form a diffraction pattern or an image which is collected by the CCD camera. The DTEM in its current configuration can acquire images with better than 10 nm spatial resolution. Figure 3.7 is an example illustrating the current spatial resolution. The figure compares a conventional TEM with a 15 ns single shot DTEM image. The alternating layers, carbon (light) and gold (dark), in the cross-sectional TEM images, with a thickness of 9 nm, are clearly distinguishable in the single-shot image. To better illustrate the resolution limit the line profile intensity across the multi-layer was measured and plotted. Further, Figure 3.7 demonstrates the capability of identifying crystal defects from images acquired in the single shot mode. Grain boundaries, twin boundaries and dislocations are clearly discernible. The DTEM can capture consecutive series of images when operated in pulse-train mode. With a dialed in time delay after the sample drive provided the stimulus to activate the irreversible transitions in the specimen are of interest, the cathode drive laser illuminates the photo-electron cathode with up to nine (9) 10 ns FWHM pulses in a pulse train. Thus, nine photo excited electron pulses with a pre-selected temporal resolution ranging from as small as 5 ns to 10 μ s result. The time delay between the individual pulses or inter-frame time can be varied from 25 ns to 250 μ s. Each of the electron pulses of the formed pulse train subsequently interacts with the specimen and formed diffraction contrast images or diffraction patterns are captured with a 2k by 2k single-electron sensitive CCD camera utilizing a high voltage electrostatic deflector. (see Fig. 3.8)

In pulse train mode nine separate observations (frames) are collected from a single irreversible transition with nano-scale spatial resolution at an appropriate temporal resolution of nano- to micro- seconds per frame for total observation times ranging from micro- to milli-seconds.

DTEM adds two laser systems to a conventional 200 keV TEM to enable:

- ✓ Driving sample events with **high**-spatio(nm) temporal (12ns) temperature gradients ($\sim 10^{11}\text{K/s}$)
- ✓ Real-space imaging and diffraction with ~ 15 ns exposures ($=$ *temporal resolution*)
- ✓ **Enough signal in one exposure to form an image (up to 2×10^9 electrons)**

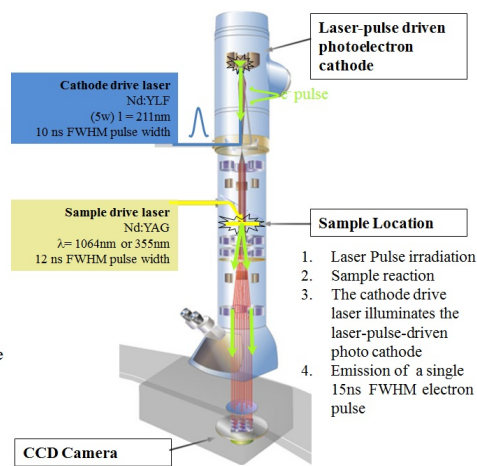


Figure 3.6: The Dynamic Transmission Electron Microscope (DTEM) in a Single-Shot mode [2]

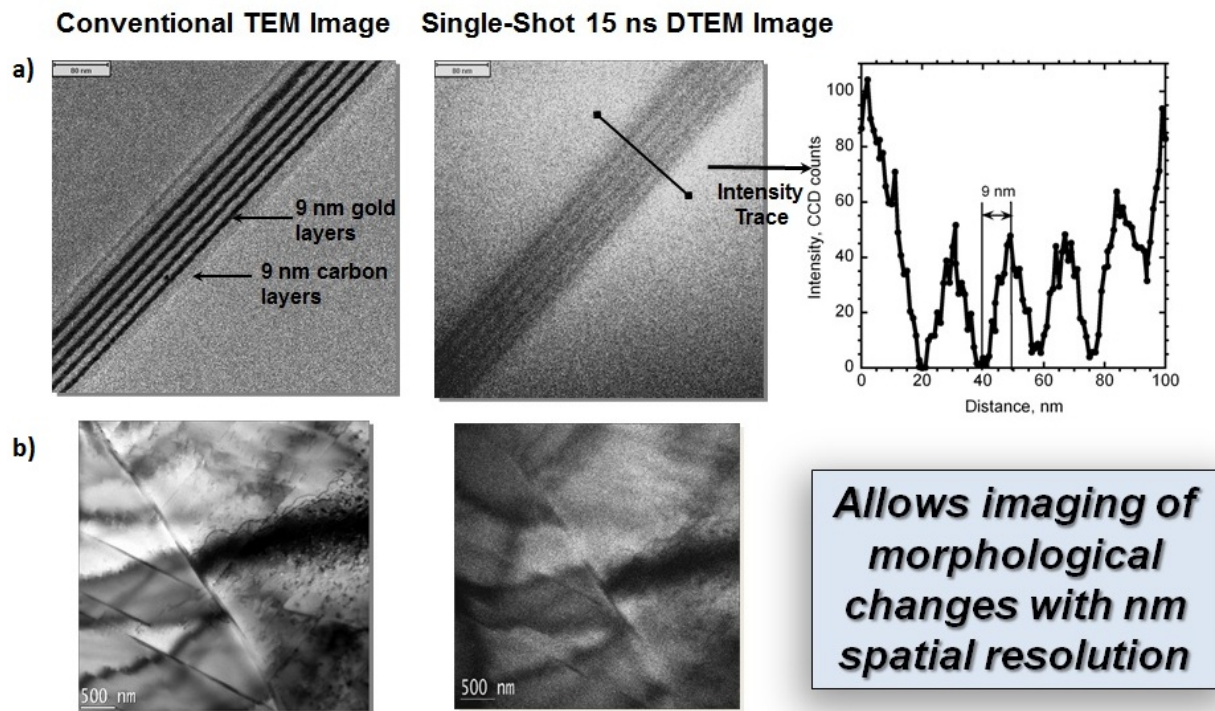


Figure 3.7: **a** showing a conventional bright-field TEM image alongside a single-pulse (15ns) to demonstrate the *nm* spatial resolution achieved with the DTEM, the line-profile shows the distinct regions of the Au(dark)-C(light) layered structure. **b** example images showing achievable diffraction contrast (i.e. stacking faults and dislocations) with the single shot approach in comparison with the conventional TEM image [38]

Pulse Train – Series of Images

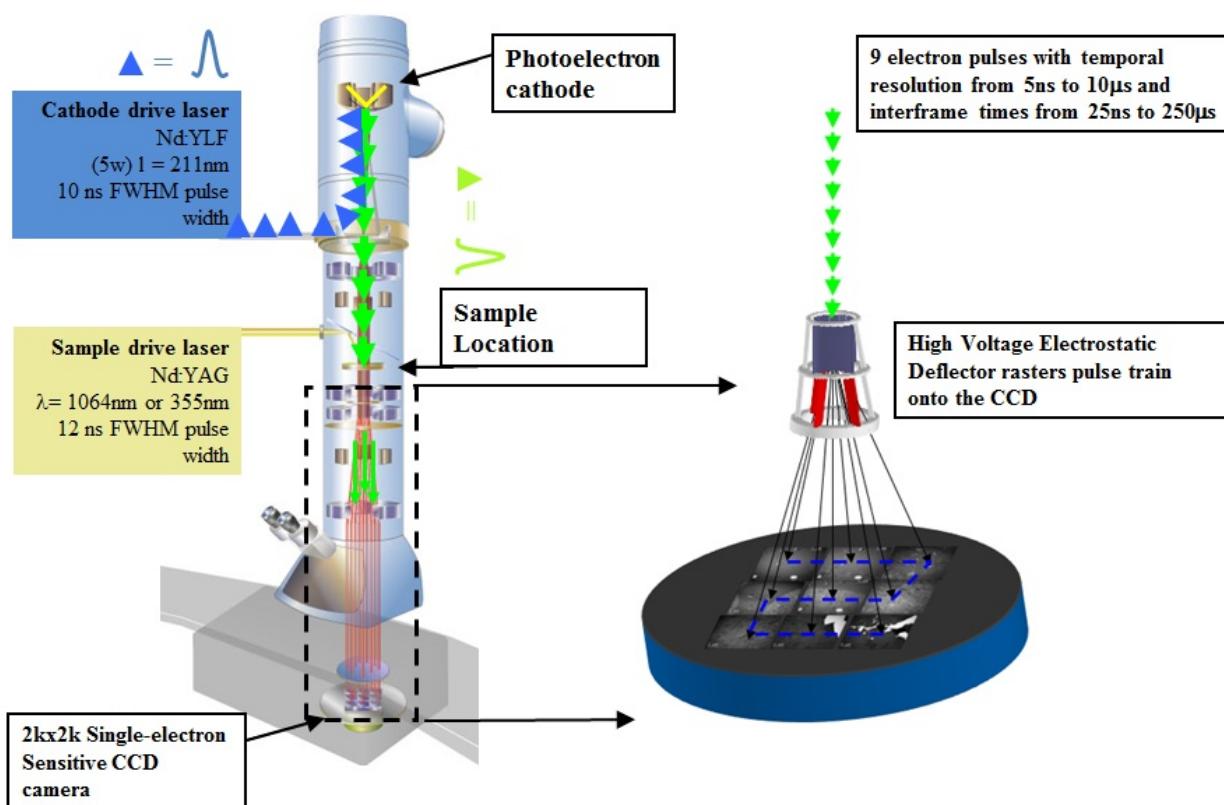


Figure 3.8: DTEM setup for Pulse-train Operation [2]

4.0 RESULTS

4.1 PURE ALUMINUM

4.1.1 As-deposited State: Aluminum Thinfilms

For an evaluation of the microstructural changes accompanying the phase transformations subsequent to pulsed laser irradiation induced melting it is necessary to determine the microstructural characteristics of non-irradiated specimens. Here the microstructure of Al thin film after deposition and prior to pulsed laser irradiation has been characterized using TEM methods regarding metrics, such as grain size, grain-size distribution, film thickness, and possible underlying texture. Figure 4.1 shows a BF TEM image of pure Al thin film prior to the pulsed laser irradiation experiment. The contrast features are associated with orientation changes and therefore, reveal that the initial state of the film is of nano-crystalline nature with an average grain size of ≈ 150 nm. The field of view of the micrograph in Figure 4.1a is circular because of the inserted selected area aperture. Figure 4.1 clearly illustrates the scale of the area (diameter of $7.5\ \mu\text{m}$) and the large number of grains in the volume of the thin film specimen used to form corresponding selected area diffraction patterns (SADP) shown in Fig. 4.1b,4.1c. The two SADP in Fig. 4.1b have been obtained for two different tilt orientations of the thin film relative to the incident electron beam, namely for the untitled condition at 0° (Fig. 4.1b top panel) and a significant axial tilt at -25° (Fig. 4.1b bottom panel). Figure 4.1d displays the sum intensity associated with the diffraction rings in the SADP for the two different specimen tilts as azimuthal integrated diffraction pattern profiles (PASAD). The SADP's in Fig. 4.1b can be indexed as (fcc)-Al. However the $\{111\}$ and the $\{200\}$ rings in the SADP for the 0° -tilt conditions exhibit unusually weak intensity as

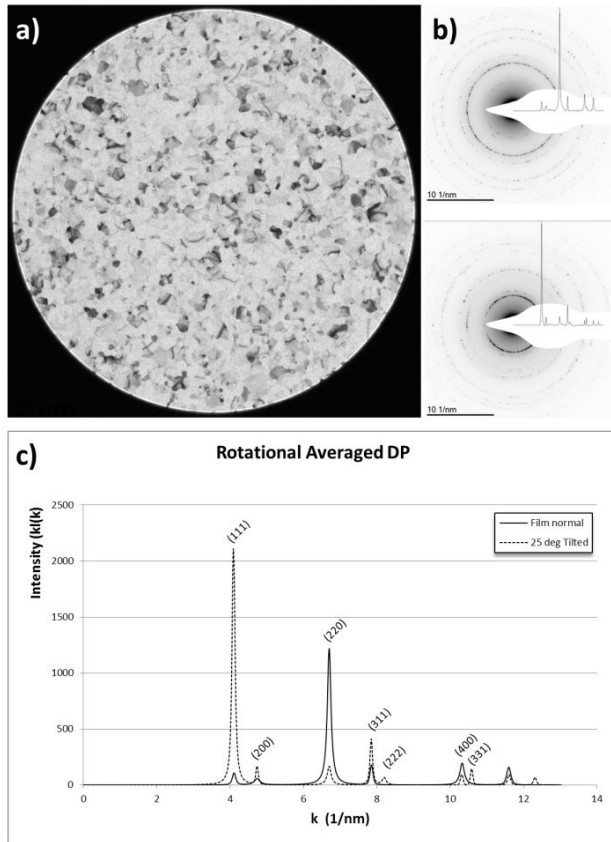


Figure 4.1: Bright-Field (BF) image of an example nano-crystalline microstructure **a** top: Ring-type selected area diffraction pattern obtained at 0° specimen tilt and, **b** bottom: at a -25° specimen tilt from the same area as shown in **c** Rotational integrated intensity plot for the two selected area diffraction patterns in (intensity vs. k) **b**).

compared to the rather strong intensity of the $\{220\}$ ring, e.g see Fig. 4.1b, and perhaps more clearly illustrated in the intensity profiles shown Fig. 4.1d. The diffraction intensity profiles plots displayed in Fig. 4.1c, which are plots of intensity vs. the diffraction vector magnitude $|\vec{k}|$, have been obtained by azimuthal integration and appropriate background subtraction. The deviation from the intensity ratios expected for a random orientation or powder sample of (fcc)-Al observed here would be consistent with an underlying $\{111\}$ texture. A $\{111\}$ -film texture with preferential alignment of the normals to the $\{111\}$ planes of the Al crystal parallel to the thin film normal is quite common for thin films of fcc metals under the growing condition with $T_S/T_M \approx 0.3$, where T_S is the substrate temperature and T_m is the melting point of the evaporated substance [39]. Furthermore the expected grain size, under growth conditions of $T_M/T_S \approx 3$, is expected to be between 25 nm and 250 nm [39]. The texture manifests upon tilting intensity shift from the $\{220\}$ peak position to the $\{111\}$ peak in the SADP and is accompanied by peak broadening. Furthermore, strong arcing becomes apparent in the tilted SADP itself (compare Fig. 4.1b top and Fig. 4.1b bottom panel). Based on the conventional TEM investigation of the thin films after deposition it can be concluded that the films are continuous, polycrystalline aggregates, comprise of nanoscale grains of equiaxial shape and exhibit a preferred texture with the $\{111\}$ planes parallel to the film plane.

4.1.1.1 PED Investigation of Thin Films in as-deposited State The conventional TEM imaging and SAD analyses indicated the presence of a $\{111\}$ -fiber type macro-texture for the microstructure of the Al thin films in the as-deposited state. Precession electron diffraction orientation image mapping (PED-OIM) allows sequential collection and indexing of diffraction patterns in a scanning fashion with nanometer spatial resolution (see section PED). An orientation map for the as-deposited aluminum thin film is displayed in Figure 4.2. Here, Figure 4.2a plots a PED-OIM map or inverse pole figure base orientation map (IPF map for short), where the film normal is parallel to the incident electron beam for the untilted specimen and the crystal poles parallel to the film normal in each grain are colored coded according to the unit stereographic triangle based legend, (see Fig. 4.2a). The IPF map legend indicates that shades of blue correspond to orientations near the $\{111\}$ corner,

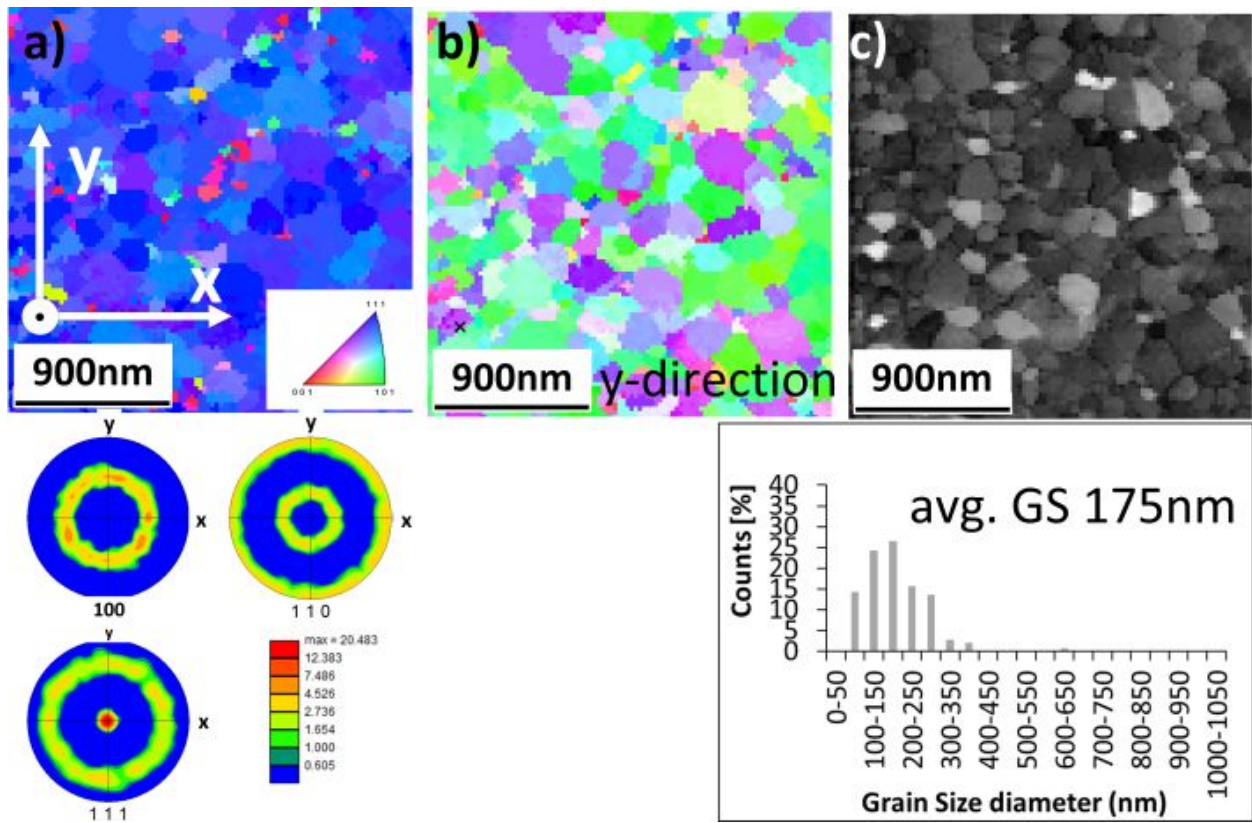


Figure 4.2: Inverse Pole Figure (IPF) based orientation maps and associated 100-, 110- and 111-pole figures for the Al thin film with 160nm thickness **a** FN **b** y-direction **c** virtual Bright field

shades of red to orientations close to $\{001\}$ and shades of green to orientations close to $\{110\}$ orientation. From the color coding in Figure 4.2a a strong $\langle 111 \rangle$ fiber or film texture is clearly apparent. The complementary rotations into the in-plane directions, here denoted x- and y- direction are displayed in the IPF-maps of Fig. 4.2b and Fig. 4.2c, respectively. Further the complementary pole figures for Figure 4.2b and Fig. 4.2c show that the $\langle 110 \rangle$ directions are randomly oriented about $\langle 111 \rangle$ -fiber parallel to the film normal. The virtual bright-field (vBF) image shown in Figure 4.2d displays the grain-size and -shape very convincingly and effectively. The resulting grainsize distribution obtained by computer-based numerical image analysis for the $2\ \mu\text{m}$ by $2\ \mu\text{m}$ scan are of Fig. 4.2 is plotted below the vBF image the average grainsize of around $175\ \text{nm} \pm 20\ \text{nm}$ is also indicated. The PED-OIM scan was performed with a $20\ \text{nm}$ step size and a $5\ \text{nm}$ probe size leading to the $20\ \text{nm}$ error bar, equating to to the lateral spatial resolution. For thin films with a thickness of $160\ \text{nm}$ by electron beam evaporation at a temperature equal to $T_s \approx 0.3 * T_m$ an average grain size of around $160\ \text{nm}$ is expected. Together with equiaxed cross-section columnar grains with dense grain boundaries, and some grains are expected being on the order of three times the film thickness and surrounded by smaller grains.

4.1.2 Ex-situ Irradiation Results of Aluminum Thin films

After deposition of the metallic thin films, the samples have been irradiated with a single pulse from a $248\ \text{nm}$ wavelength (KrF) excimer laser, projected through a single-slit Cu-mask with a five times demagnification in the ex-situ melting setup, Fig. 4.3a. The mask is used to define the shape and dimensions of the laser pulse that is projected onto the electron transparent window of the thin film sample (Fig. 4.3b). A very small central area of the much larger laser beam profile emitted by the KrF-excimer laser system is selected to ensure a highly uniform energy profile in the sample modifying laser pulse. The laser projection system is configured to provide localized and complete melting of metal thin films over area approximately $20\ \mu\text{m}$ wide and $200\ \mu\text{m}$ long. A post-mortem BF TEM image collage of a solidified melt pool of an Al-08 at.%Cu thin film is displayed in Figure 4.3c. The distinct and high-aspect ratio elliptical shape of the melt pool allows the investigation of two very different

heat extraction geometries along the major and minor axis respectively. At the co-vertices (along minor axis) the curvature of the ellipse is minimal, and thus the heat extraction is assumed to be the lowest, while at the vertices (along major axis) the curvature is maximum and thus the heat-extraction is the highest. In order to achieve full melting on the scale on the order of the melt pool melt pool presented in Figure 4.3c required conducting of subsequent sequences of separate pulsed laser (pl) irradiation induced solidification experiments. These sequences of experiments involved systematically increasing the fluence of the laser pulse from low to high energy. At low energy fluences the metal film was often only partially melted (PM) and melt pool dimensions were much smaller than the beam shaping aperture projection. With increasing energy the metal dimensions increased until the metal film was found to melt through thickness, established melt pool with the dimensions close to the five times demagnified aperture dimensions of the Cu-mask. When the laser beam energy (fluence values) in excess of the critical values were high the metal thin film would exhibit de-wetting from the underlying amorphous Si_3N_4 membrane substrate or the membrane of amorphous $500\ \mu\text{m}$ by $500\ \mu\text{m}$ electron transparent Si_3N_4 window region would rupture. A representative solidification section for pure Al along the minor axis of the elliptical melt pool with dimensions of about $20\ \mu\text{m}$ to $200\ \mu\text{m}$ corresponding to the mask dimensions provided by the laser projection system is depicted in the scanning TEM (STEM) micrographs of Figure 4.4. The post-mortem BF STEM image in Fig. 4.4 shows a zone of a re-solidified Al thin film superimposed with a schematic top hat laser pulse profile, which provides an illustration of the association of the morphologically different microstructural zones and the laser profile. Identified in the image are three distinct regions, Zone 1 through 3, which are defined as follows:

Zone 1 - The heat affected zone (HAZ): This regions consists of equiaxed grains that decrease in size with increasing distance from the melt-pool edge. Thermally activated, diffusional grain growth occurs dominantly in the thin film plane due to the dominant in-plane heat flux geometry provided for the thermal energy deposited into the film by the photon field from the laser pulse.

Zone 2 - The transition zone between fully solid and fully liquid (melted): Here, solidification of the pulse laser irradiated metal commences when the temperature of the liquid

in the melt-pool decreased sufficiently to reach the Al metal melting point $T_M = 660\text{ }^\circ\text{C} \approx 933\text{K}$. Solidification initiates at the unmelted pre-existing poly-crystalline grains composing the interface between the granular single phase solid and the single phase liquid metal of the melt-pool. In the transition zone, adjacent grains grow into the melt, mostly anti-parallel to the unidirectional long-range thermal gradient, but also laterally, expanding their width in a competitive growth mode. Hence, some grains expand wider in the plane of the film at the expense of their neighbors. As a result many grains are occluded and prevented from further crystal growth in the beginning of the solidification process forming Zone 2 in Figure 4.4.

Zone 3 - The unidirectional growth zone: The grains that successfully emerged from the transition zone advance along the growth direction (GD) towards the center of the melt-pool, anti-parallel to the pre-dominant heat flux and resulting far-field thermal gradient. The resultant columnar or long ribbon-like morphology grains forming Zone 3 maintain an approximately uniform width until all melt is consumed.

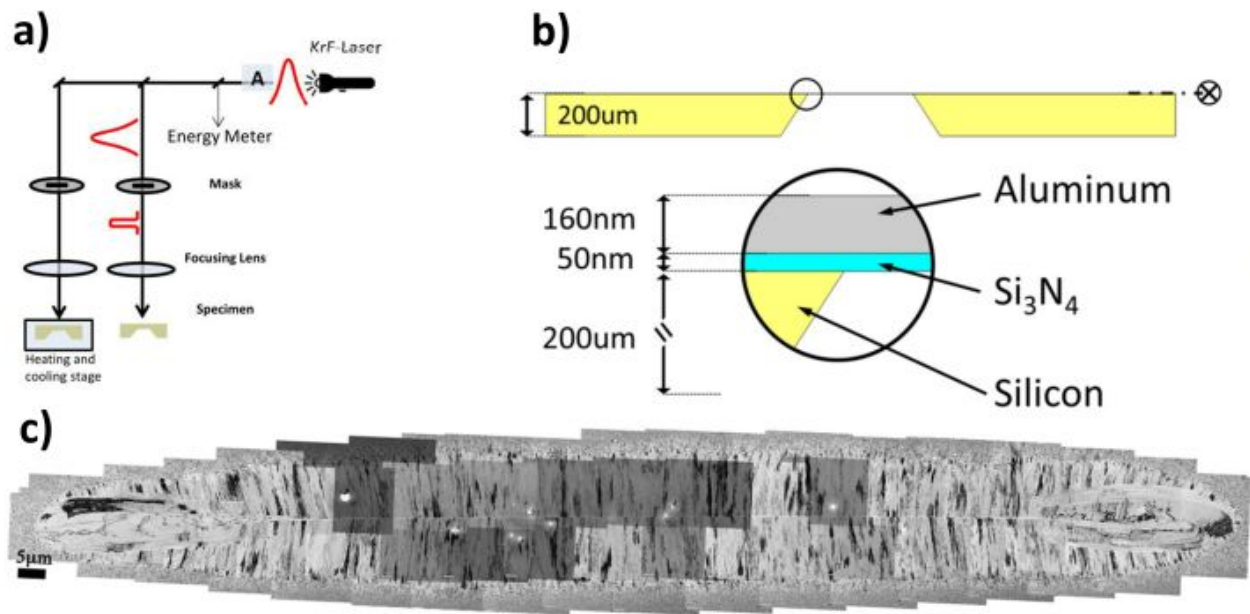


Figure 4.3: i) Schematic of the ex-situ melting stage, ii) sample geometry iii) Example melt-pool

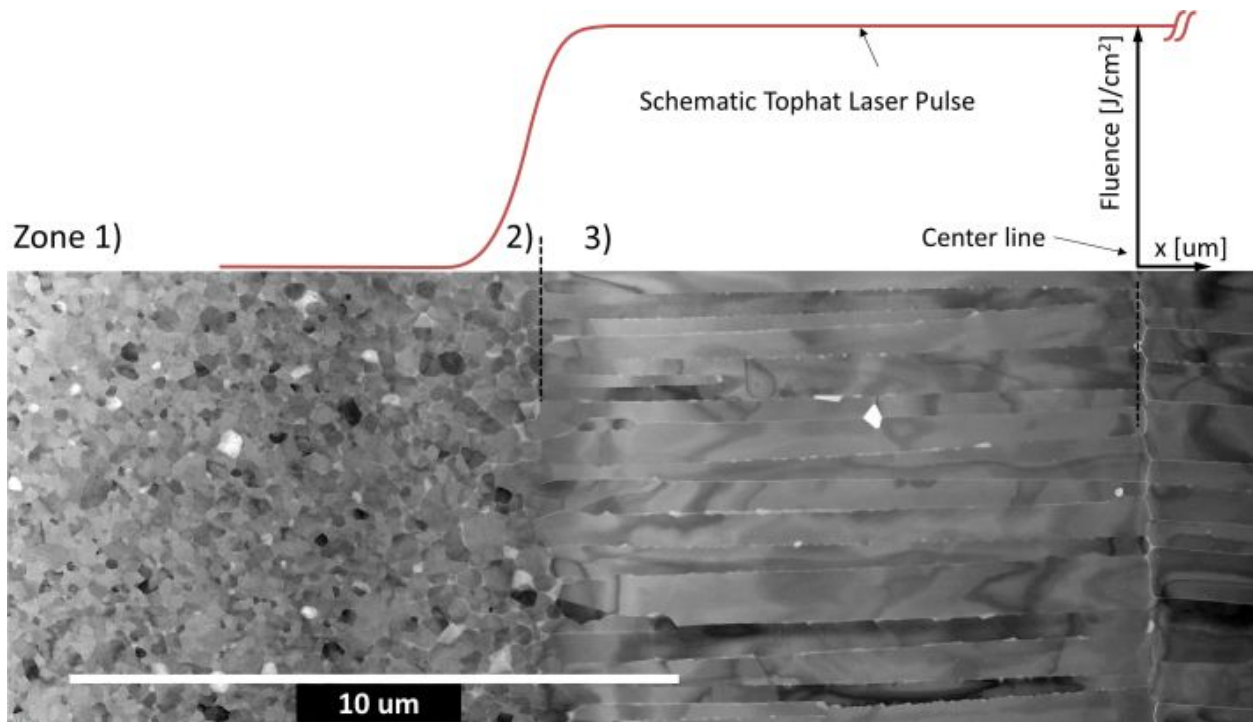


Figure 4.4: Example cross section of an ex-situ irradiated Aluminum thin film revealing 3 distinct regions 1) Heat affected Zone 2) a transition Zone 3) a directionally solidified zone. Indicated is a spacial distribution profile for the associated ns- melt-pulse profile, that initiates melting and subsequent solidification

4.1.2.1 PED Investigation of Ex-situ Modified Al Thin Films Thin-films exposed uniformly to thermal energy exhibit an isotropic grain morphology. The mechanisms that alter the grain size scale in polycrystalline thin films are associated closely with reduction in surface free-energy differences, and overall reduction in total excess interfacial free energy. In the single PL irradiation experiments a spatio-temporally non-uniform heat treatment locally raises temperatures well above the melting point of the metal that alter the grain morphology significantly. The thermally induced modification of the microstructure can lead to a distribution of grain orientations that differ from those present in the polycrystalline aggregate solid prior to melting, establishing new solidification or crystal growth textures. The PL irradiation produces various locally different microstructures ranging from long parallel crystallites to a fine equiaxed microstructure depending on the amount of thermal energy deposited into the film by the photon field from the ns-laser pulse. Thus, the location dependent deposited thermal energy invokes several different energy releasing mechanisms ranging from re-crystallization to reorientation to selective grain melting. Precession electron diffraction orientation image mapping (PED-OIM) allows sequential collection and indexing of diffraction patterns in a scanning fashion with nanometer spatial resolution (see section PED). PED OIM allows collection of locally resolved, qualitative and quantitative information on grain size, orientation, shape, and grain-boundary character. The IPF-map in Figure 4.5 has been obtained from PED-OIM utilizing a stepsize of ≈ 20 nm with a ≈ 5 nm probe size corresponding to 50 diffraction patterns per micro meter ($50 \text{ DP's } \mu\text{m}^{-1}$). Each pixel in Figure 4.5 corresponds to an orientation that was determined by indexing the pseudo-kinematically acquired PED pattern crystal direction or piles oriented parallel to the film normal. Again the pole orientations are colored coded according to the unit stereographic triangle based legend, (Fig. 4.5). The overwhelming dominance of the near blue $\langle 111 \rangle$ corner, shaded orientations is consistent with a strong $\langle 111 \rangle$ -film or fiber texture. More detailed analysis of the texture using the $\langle 111 \rangle$ -polefigure plotted in From the color coding a strong $\langle 111 \rangle$ fiber texture is clearly apparent. Pole figures have been obtained from the PED-OIM data sets. The $\langle 111 \rangle$ pole figure plotted in Fig. 4.5 shows that the $\langle 111 \rangle$ poles are, within a 12.5° parallel, or 70° inclined, to the film normal direction. Furthermore, the $\langle 110 \rangle$ pole figure shows that the majority of grains are randomly rotated about the $\langle 111 \rangle$ axis. The

heat deposited into the metal film by the photon field is dissipated predominantly along in-plane direction of the metallic film, denoted as x-direction in Figure 4.5. To explore the effect of the strongly directional heat transport through the metallic film on grain orientation and grain size of the PL irradiation induced transformation product microstructure, a rotation of the orientation data set obtained by PED-OIM for the Al thin film has been performed such that the crystal plane normal direction oriented parallel to the uni-axial heat extraction direction can be displayed in a color coded IPF-map (e.g. Fig. 4.6). Figure 4.6 clearly shows that no obvious preferred growth orientation exists for the directionally solidified, columnar morphology grains of Zone 3 in Al. However, the pole figures obtained from the large PED-OIM scan data sets shown in Figure 4.6 contains the averaged orientation information of all the different morphological zones affected by the photon field of the ns-laser pulse. In order to evaluate quantitatively changes in the microstructural metrics associated with the morphologically different microstructural zones that can be distinguished after the PL irradiation induced transformation it is necessary to explore relevant sections/segments obtained from the large field of view of the PED OIM scan separately. Figure 4.7 displays the segmented areas of the HAZ, Zone 1, adjacent to the directionally solidified microstructural constituent, Zone 3, together with the associated pole-figure plots for the heat flow direction which is perpendicular to the perimeter of the melt pool pool boundary, labeled z in Figure 4.7. As the distance from the melt pool edge increases from left-to-right, from Fig. 4.8a to Fig. 4.7f, it is apparent from the set of corresponding $\{100\}$, $\{110\}$ and $\{111\}$ pole figures that the texture of the grains in the HAZ remains essentially constant. Moreover, the pole figures indicate that no obvious preferred orientation is present with respect to the heat extraction direction in the HAZ, since the $\langle 111 \rangle$ poles remain parallel to the film surface normal and the $\langle 110 \rangle$ poles are evenly distributed over all possible orientations with respect to the heat flux direction, implying random grain orientations of the directions in the film plane. This shows that the $\langle 111 \rangle$ fiber texture of the as-deposited state of the Al film is inherited by the PL irradiation affected microstructure in Zone 1 (Figure 4.7a to Fig. 4.7f). The pole figures also indicate that the top-hat shaped pulsed laser irradiation induced directional heat-flux does not change the texture present in the zones leading away from the melt pool, i.e., Zone 1,2. (Fig. 4.7 and Fig. 4.8). Figure 4.8 summarizes the

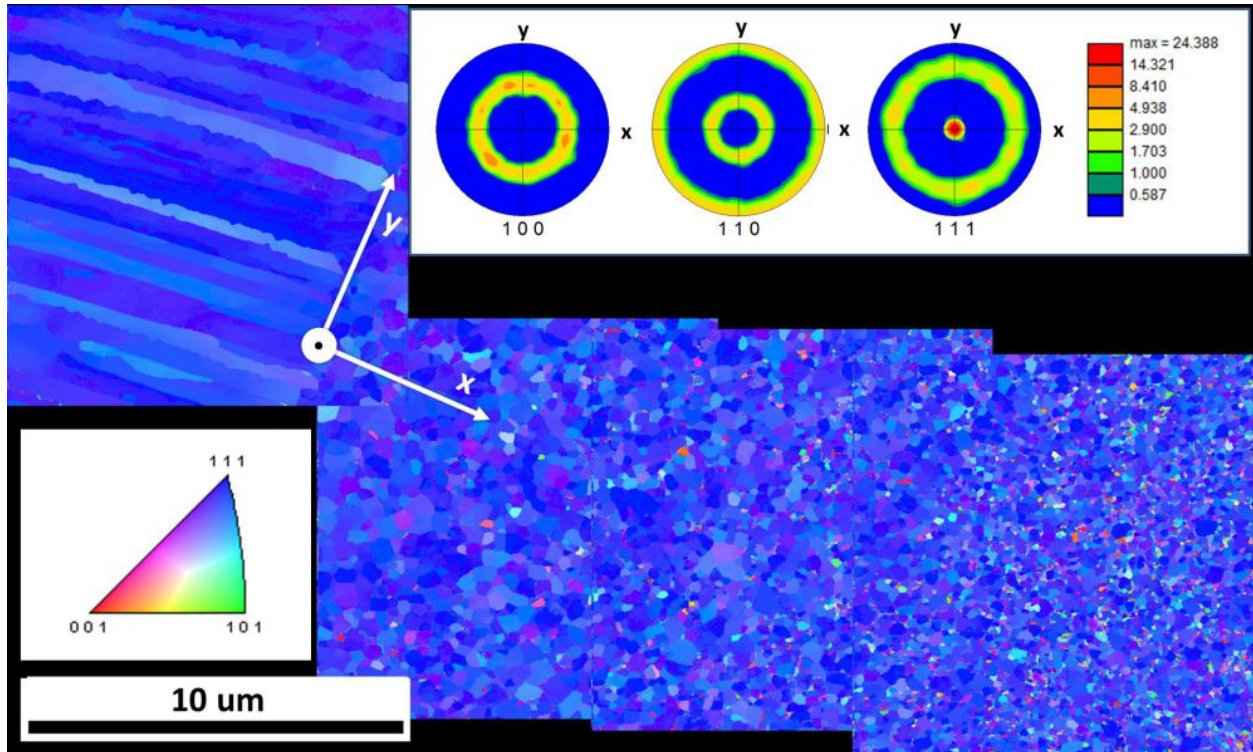


Figure 4.5: PED OIM scan of the strongly modified microstructure of the metallic thin film, from weakly heat-affected-zone to the growth zone to detect changes in texture. Plotted is the film normal [FN] here denoted as \vec{z}

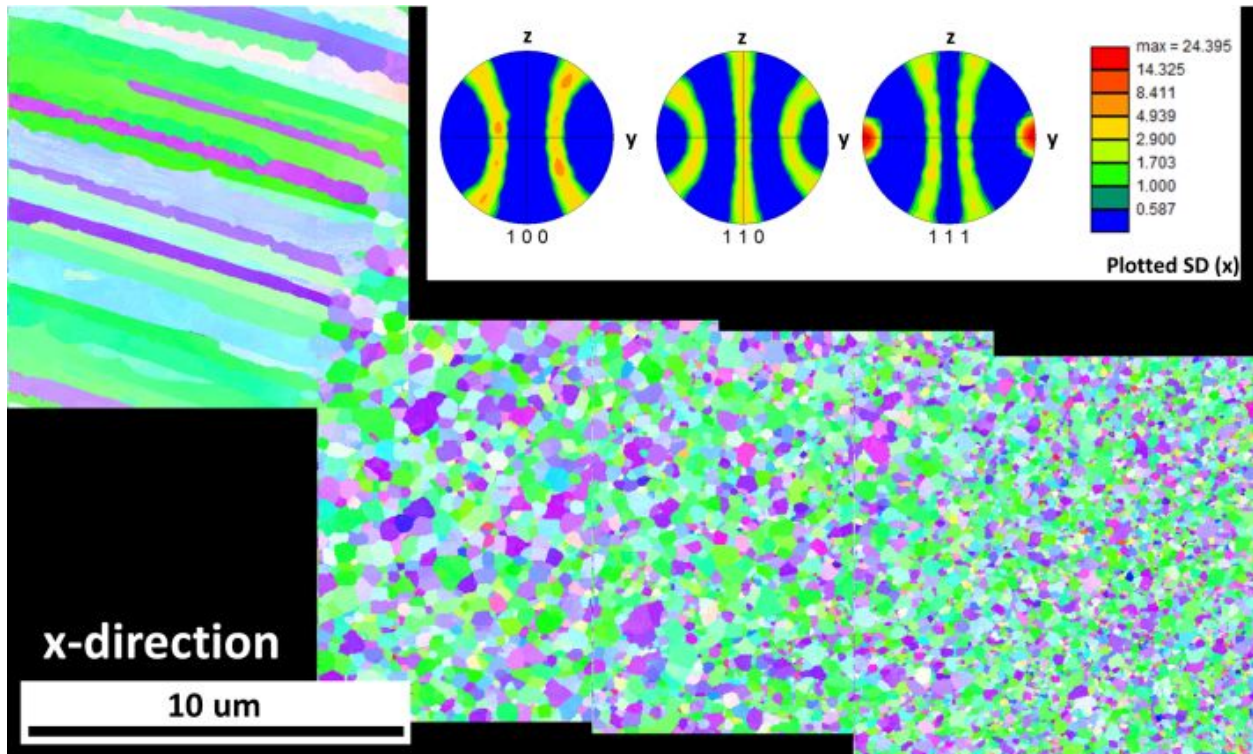


Figure 4.6: PED OIM scan of the strongly modified microstructure of the metallic thin film, from weakly heat-affected-zone to the growth zone to detect changes in texture. Plotted is the Heat Extraction direction [FN] here denoted as \vec{x}

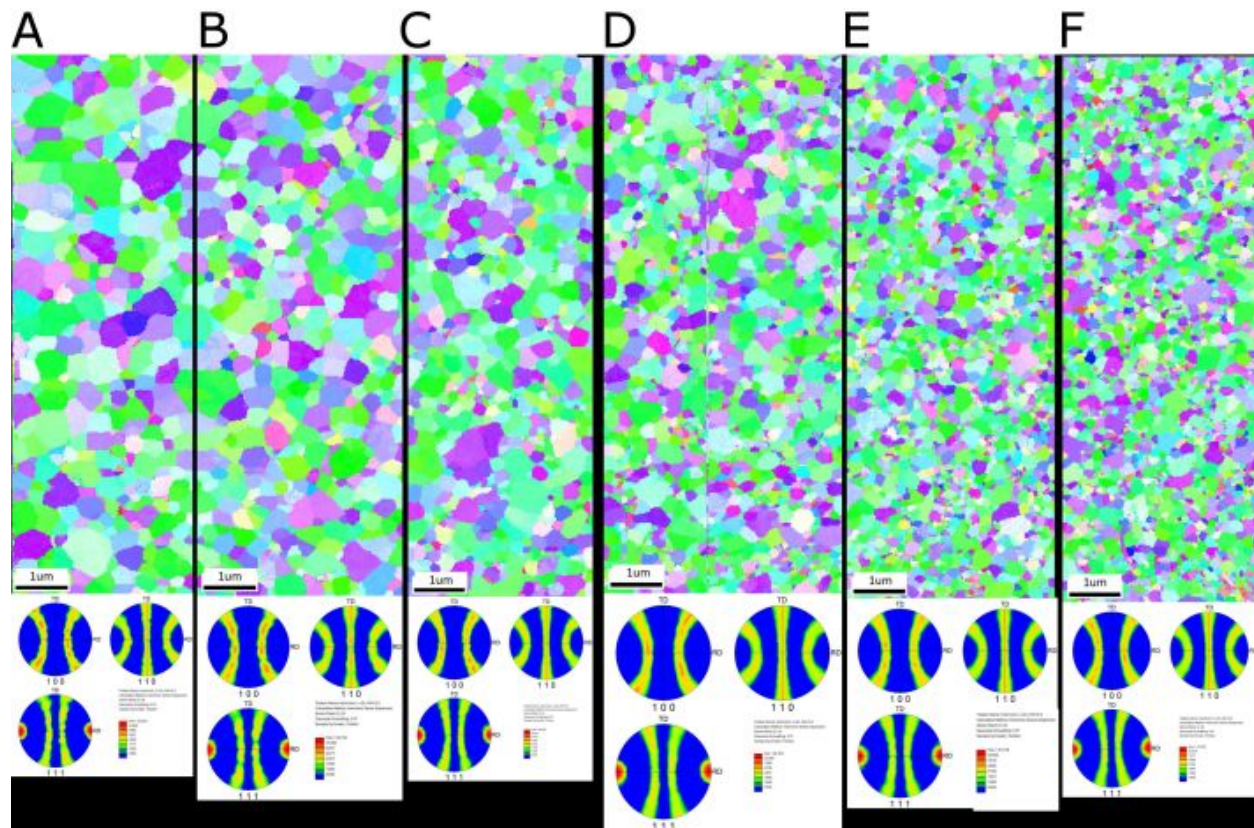


Figure 4.7: Texture analysis of slices with respect to the distance to the melt pool edge, no indication of a texture change.

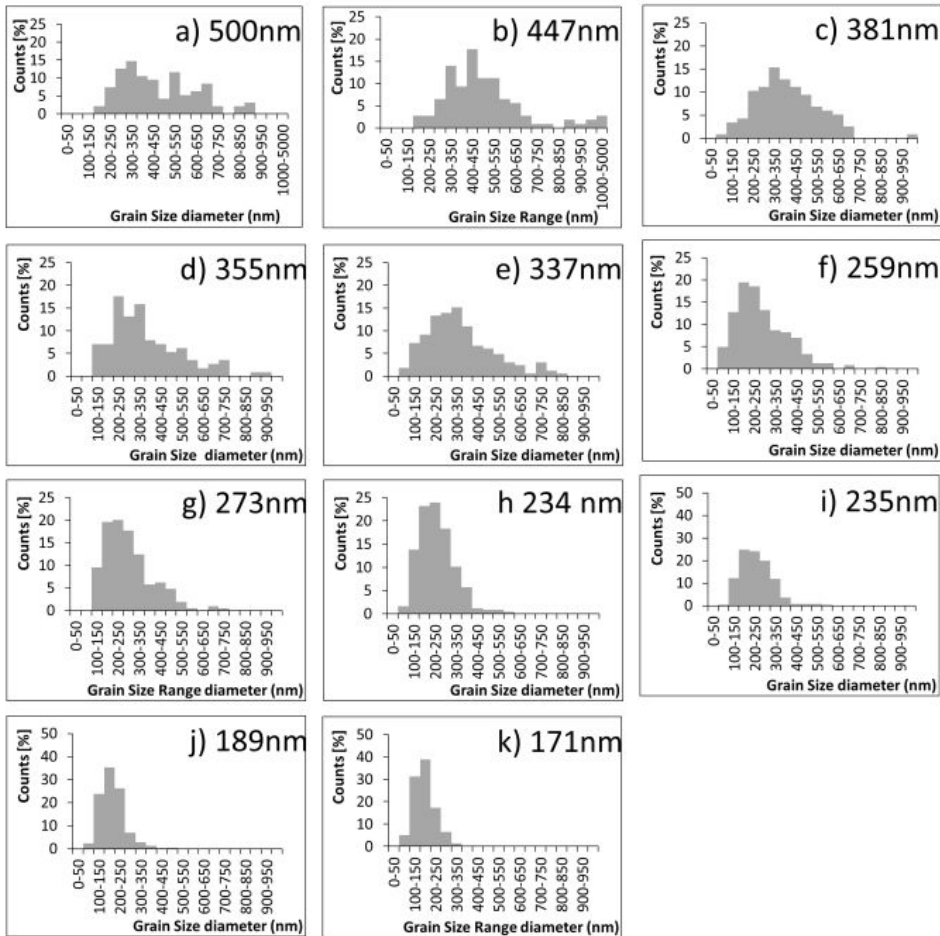
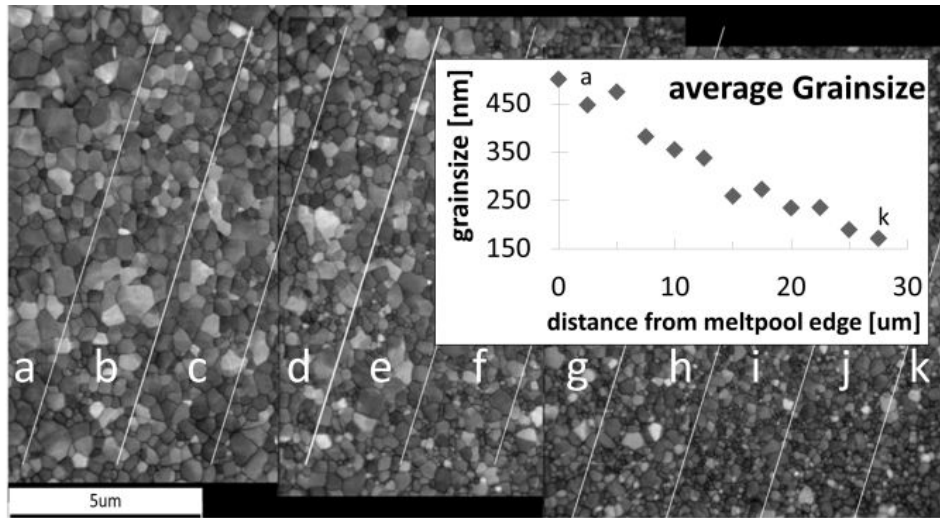


Figure 4.8: HAZ Grain size analysis

grain size development as a function of distance to the melt pool edge. The grain size was determined by measuring the minor and major axis of 150 to 300 grains in the indicated segments in the vBF image of Figure 4.8a. The segments were sliced such that the long dimensions of the rectangular area are oriented approximately perpendicular to the unidirectional heat flux direction from zone 3 through to zone 2 and zone 3. The vBF image has been obtained by averaging the intensity for all the diffraction patterns within a virtual aperture, here the virtual aperture of 5 pixel diameter selected the transmitted central beam, 000, for image contrast formation. The resultant gray-scale image exhibits contrast similar to that of a low-quality BF-STEM image. For each segment marked in the vBF image of Fig. 4.8a, Fig. 4.8a-Fig. 4.8f display the resultant grain size distributions and the indicate the resulting arithmetic mean grain size. The average grain size plot versus distance, shown as an inset to the vBF image of Fig. 4.8, clearly allows demarcation of different grain size regimes. Thus, for distances from the melt pool edge up until 5000 nm = 5 μ m the grain size remains approximately constant at \approx 460 nm and at larger distances drops precipitously to 350 nm, prior to a monotonic and continuous decline in a linear fashion to an average of 150 nm at \approx 30 μ m away from the former melt pool edge. The grain size distributions in Fig. 4.8a and Fig. 4.8b show bi-modal distributions with a grain size ranging from 150 nm to > 1000 nm. Inspecting the grain size distributions for locations in the HAZ further away from the melt pool edge, e.g. Fig. 4.8c-4.8k, shows a gradual transition from a Weibull distribution towards a Gaussian distribution with an average grain size close to that of the as-deposited Al thin film of 170 nm. The bi-modularity of the grain size distributions and the step-like drop in the mean grain size after the first two segments closest to the melt pool edge could indicate a liquid-solid phase transformation for this region, which would be suitable to rationalize the observed order-of-magnitude (\approx 10) increase in grain sizes relative to the 160 nm film thickness. The pole figures shown in Figure 4.6 already documented that the pre-existing $\langle 111 \rangle$ -texture is maintained in zone 1, the HAZ. Upon inspection of the directionally solidified region, zone 3, in Figure 4.9 it becomes apparent that the orientation of the as-deposited condition of the Al thin film is also maintained in this crystal growth regime where the liquid-solid transformation occurred under presumably non-equilibrium RS conditions. Figure 4.9a shows the IPF-map for the film normal direction, clearly with

a strong $\langle 111 \rangle$ -fiber texture. The IPF-map of Figure 4.9b plots the crystal plane normal directions that are parallel to the solidification direction, anti-parallel to the predominant directional heat flux. In zone 3 the crystal growth appears to exhibit some preference for proceeding along the $\langle 110 \rangle$ -directions (green shaded grains). This crystallographic growth direction effect is an indication that the growing crystals advancing into the liquid Al melt have their nuclei in the boundary region of the HAZ. It further suggests that the nuclei of the growing crystals were indeed pre-existing non-fully melted grains associated with the HAZ region immediately adjacent to the melt pool edge separating the fully from the only partially melted Al thin film regions (e.g. slices (a) and (b) in the VBF of Fig. 4.8 with bi-modal grain size distributions, Fig. 4.8a and 4.8b). Comparing the mean crystal width of the directional solidified region, zone 3, with the equiaxed grain size at the boundary with the HAZ, zone 2, shows similar bi-modal grain size distributions with an average grain width of about 550 nm. The post-mortem TEM based analyses and microstructural characterization performed here for the ex-situ PL irradiation modified thin film samples of Al clearly demonstrate the feasibility of using a PL system and electron beam evaporated nano-crystalline metal and alloy thin films to study rapid solidification transformation microstructure evolution. The directional rapid solidification is promoted due to the inherent heat-extraction geometry of the thin-films. The Al-base material system investigated here does not require a protective and restrictive cap-layer to prevent de-wet during the PL irradiation induced melting and subsequent solidification processes for suitably and available laser system processing parameters. The solidification microstructures developing in the Al show three distinct morphological regions: Zone 1, the heat affected zone (HAZ); zone 2, the transition region; and zone 3, the directional crystal growth region, which consists of directionally solidified grains with dimensions of about 10 μm long by about 0.5 μm wide and spanning the film thickness of 80-160 nm. Furthermore, the inherent $\langle 111 \rangle$ -fiber texture established during the e-beam evaporation based thin film deposition is maintained in the three morphologically distinct microstructure zones. The PED-OIM analyses provided evidence for a preferred $\langle 110 \rangle$ -type crystal growth direction selection for the zone 3.

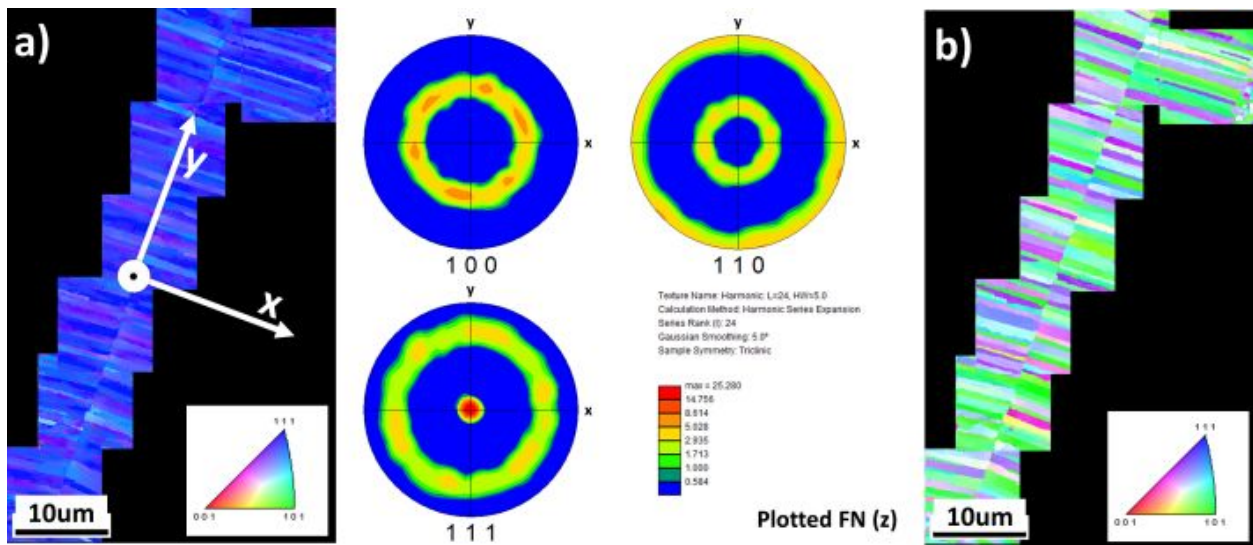


Figure 4.9: The inherent $\{111\}$ fiber texture stays apparent in the liquid-solid-growth regime, this indicates that the preexisting grains at the outer perimeter of the melt-pool are starting points of the crystallization product, i.e. columnar grown grains

4.1.3 Insitu TEM Pulsed Laser Irradiation of Aluminum Thin-films

4.1.3.1 High Spatio-Temporal Resolution Insitu TEM Observation of Melting and Solidification In-situ rapid solidification experiments have been conducted in the DTEM using a pulsed Nd:YAG laser with 1064 nm wavelength, 15 ns pulse duration and a Gaussian beam profile ($1/e^2$ diameter of $\sigma = 135 \pm 5 \mu m$) to provide a thermal stimulus for melting of the metal thin films. The laser fluence that initiates the melting event for the Al thin films was 420 mJ cm^{-2} . The PL irradiation was coupled into the TEM with an incident at 45° to the thin film sample surface normal, explaining the resultant elliptical shape of the melt pools (e.g. Figure 4.10). The locations of the fields of view relative to the PL irradiation induced melting and subsequent solidification experiments of the Al thin film presented in Figure 4.11 to Figure 4.18 are indicated in the micro-structural depiction of the melt pool in Figure 4.10 by semi-transparent circles.

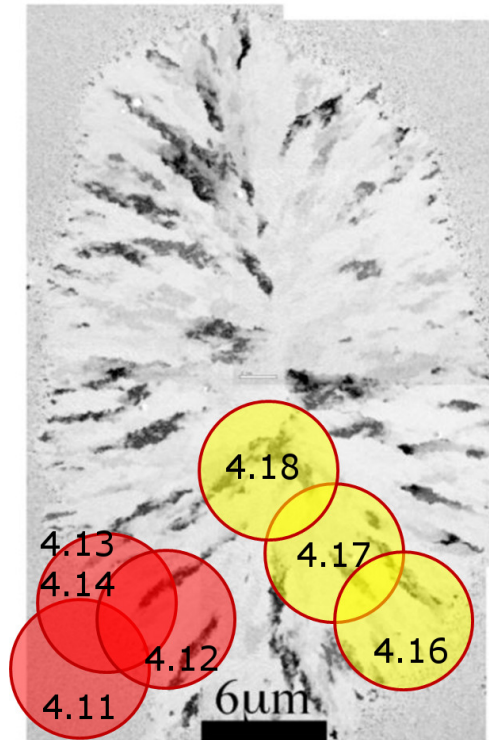


Figure 4.10: Post-mortem acquired Bright-Field images of an in-situ irradiated thin-film showing the melt-pool geometry.

4.1.3.2 Melting of Aluminum ThinFilms Dynamic observations of the pulsed-laser induced melting and subsequent re-solidification of Aluminum thin films have been performed using the DTEM instrument in the MovieMode (MM) operational mode with the goal to capture the complete sequence of the phase transformations from solid to liquid (melting) and liquid to solid (solidification), and to deliver mechanistic and morphological details of the transformation interface and instantaneous transformation interface velocity measurements. The MovieMode (MM) operation of the DTEM utilizes nine separate exposure or frames of fields of view at a preselected spatial magnification and temporal resolution determined by the combination of the exposure time per frame and the inter-frame temporal steps. In this section MM DTEM in-situ experiments have been performed using relatively high spatio-temporal resolution of an approximately 7 μm diameter field of view frame in the BF images and 220 ns total time between frames of 20 ns exposures. This spatial magnification restricts or focuses observations and measurements to small sections of the total volume melted in the Al thin film specimens by the PL irradiation. Also, over nine-frame image series of about 1.6 μs total duration only a fraction of the total time required for completion of the solid-liquid-solid transformation sequence can be observed, Hence, in the high spatio-temporal resolution MM BF image series pre-selected sub-sections or fractions of the total transformation sequence are observed with nanoscale temporal resolution. Several separate MM DTEM experiments of the pulsed laser irradiation induced melting and subsequent re-solidification have been performed at overlapping delay times and for different regions of the transformed specimen region systematically varied and overlapping delay times and for different regions of the transformed specimen region.

In combination these series of MM DTEM experiments enabled the elucidation of details of the complete transformation sequence for the Al thin films, inclusive of establishing the bulk liquid of the initial melt pools by the rapid conversion of the incident laser irradiation pulse, stages of subsequent continued melting of the adjacent polycrystalline solid and the solidification process. Figure 4.11 shows the first MM series of nine BF images, each with 20 ns exposure time and 220 ns elapsing between subsequent frames in the series, which captures the response of the nano-crystalline Al thin film at the outer perimeter of the elliptical area that underwent laser pulse related melting as indicated in Fig. 4.11z. The

multi-beam BF images capture the initial stages of a formation of the melt pool near the outer perimeter, at the boundary between a fully melted pool of superheated liquid Al and the regions of the film that remained solid, at least partially, in response to the absorption of the photon power delivered by the ns-duration laser melting pulse. The MM BF image sequence begins 200 ns prior to the laser pulse that produces the initial melt pool in the Al thin film (Fig. 4.11a). Thus the sequence envelopes a time interval from 200 ns before laser irradiation (Fig. 4.11a, label "-200 ns") to about 1560 ns after the irradiation (Fig. 4.11j, label "1560 ns"). Before melting, the multi beam BF-image of the as-deposited nano-crystalline thin film exhibits diffraction contrast features that are common to nano-crystalline Al at this spatial magnification¹. The second frame (Fig. 4.11b) generated by the second electron pulse in the MovieMode acquisition image series coincides with the irradiation of the melting pulse of 15 ns exposure duration and is labeled as 20 ns.

The thermal stimulus delivered by the high power density photon field of the specimen modifying laser pulse heats the surface of the Al thin-film and melting commences (Fig. 4.11b). Consistent with melting the contrast features discernible for the nano crystalline aggregate Al thin film in Fig. 4.11a are markedly changed, as indicated by the reduction of crystallographic orientation dependent diffraction contrast features. In comparison to Fig. 4.11a the BF image contrast in Fig. 4.11b is considerably less granular in nature. The overall reduction in contrast in Fig. 4.11b is attributed to the increase in thermally induced incoherent scattering associated with the heating of the specimen region across the field of view in response of the directional, radially outward transport of heat through the metal thin film after conversion of the photon pulse power upon its absorption into the thin film. Notably, the center of the pulsed laser irradiated region, the hottest part of the melt-pool is located considerably far outside of the field of view depicted in Fig. 4.11 towards the top-right (see Fig. 4.11z for reference). The thermal profile varies radially from the hottest central region towards the perimeter of the elliptically shaped laser pulse cross section on the Al thin film. The direction of the radial thermal profile existing in this particular set of MM BF image frames is indicated approximately with the colored arrow from hot (red color) to cold (blue color), i.e. it varies approximately diagonally across the circular fields of

¹The circular field of view spans $\approx 7 \mu\text{m}$

view (Fig. 4.11c). The directional heat extraction proceeds parallel to the indicated arrow (Fig. 4.11c). Selective melting of the Al polycrystalline aggregate, preferentially along the grain boundaries and the reduction of the two-phase region comprised of coexisting liquid and solid Al in the transition area are observed in the subsequent frames Fig. 4.11d-4.11i. Consistent with prior research using the DTEM for BF imaging and selected area diffraction for Al thin film prior to and after pulsed laser induced melting [40], in the BF images of Fig. 4.11 the light contrast features are associated with the crystalline phase of the solid Al and the quite uniform darker contrast regions are associated with the liquid Al, the melt. From frame c to i in Fig. 4.11 the area fraction of solid Al grains reduces monotonically, while the area fraction associated with the liquid Al increases, following the thermal gradient approximately diagonally across the circular field of view from the top right to the bottom left. Fig. 4.11y is a post-mortem image taken with a single electron pulse observing the microstructure several seconds after successful melting and completion of solidification. In this particular field of view the microstructure has significantly coarsened and exhibit morphologically equiaxed grains of Al. Figure 4.12 repeats the experimentation of pulsed laser induced melting and subsequent solidification with a pre-delay time of 1000 ns = 1 μ s rather than at -200 ns as in Figure 4.11. The MM BF image series in Figure 4.12 shows nine 20 ns exposure images capturing the melt dynamics close to the edge of the laser pulse affected region. Again the location of the circular field of view for the dynamic in-situ sequences captured in the MM BF image series of Fig. 4.12a-4.12i is marked in the post-mortem BF image of Fig. 4.12y. In this series the individual contrast producing features visible in frame of Figure 4.12a completely disappear at longer times during the subsequent frames of observation, leaving only Al melt behind Fig. 4.12j, the liquid state manifesting in uniform dark contrast. Figure 4.12 and 4.13 capture the sequence of melting of poly-crystalline aggregate Al thin film due to heating from the adjacent super-heated liquid in the initial melt pool generated by the 15 ns specimen laser irradiation pulse. The post solidification BF-image of Figure 4.12y shows only directionally grown features. This is expected for the columnar morphology in zone 3 where directional rapid solidification crystal growth occurs. When shifting the observational field of view to the location of the expected melt pool edge region of the PL irradiated area the development of a solid-liquid interface is observed. An example

of a MM BF image series from such a location is shown in Figure 4.13. The images series in Figure 4.13 spanning $1760 \text{ ns} = 1.76 \mu\text{s}$ captures the melting of the crystalline grains, which are surrounded by liquid. Furthermore, during the duration of the in-situ observations, the time interval of $1.76 \mu\text{s}$ after the initial Al thin melting laser pulse irradiation, heat is constantly extracted from the super-heated liquid Al through the solid (along the direction indicated by the arrow, from red (hot) to blue (cold)), which leads to grain growth, potentially grain reorientation, and general coarsening in the poly-crystalline solid region adjacent to the liquid-solid interface, parts of as the HAZ, Zone 1 in Figure 4.4. Notably, the HAZ exhibits coarsening grain size and maintains the texture evolution with the aid of Figure 4.5 to 4.8. Examples of grains that exhibit clearly discernible grain growth are highlighted in the BF images frames of Fig. 4.13c and 4.13h in Figure 4.13. In the post-mortem BF-image (Fig. 4.13y) the solidified microstructure is visible. The transition zone between the HAZ and the crystal growth region with cellular/columnar morphology solidification product micro-constituent is captured in a separate MM BF image series experiment (shown in Fig. 4.14). The sequence of dynamic in-situ observations depicted in Figure 4.14 has been obtained when repeating the MM BF image series experiment summarized in Fig. 4.13 with a longer pre-delay time of $3000 \text{ ns} = 3 \mu\text{s}$ in an identical location relative to the transition between zone 1 (HAZ) and Zone 3 (directional crystal growth). The location for the field of view of the Fig. 4.14 MM BF image series shown for convenience in Fig. 4.14z). The sequence of dynamic microstructural evolution is captured and illustrated in Fig 4.14 shows the phase transformation sequence at a later point after the initial pulsed laser irradiation melting event, that is temporally subsequent to the observations and measurements collected in Figure 4.14. The phenomenological observations shown in Figure 4.13 are extended to longer times after the PL irradiation induced melting in Figure 4.14. In the first frame (Fig. 4.14a label '3 μs ') a significant fractions of crystalline grains are still present in the liquid region to the top and right of the liquid solid interface. In Fig. 4.14a three morphological distinct regions can be identified. Namely, a region that is fully melted, top right corner in the field of view, a region that is fully solid ,bottom left in the field of view, and a region in the center of the field of view that is interpreted as a solid-liquid phase mixture. Following the BF images series in Figure 4.14 in the temporal sequence of the frames in

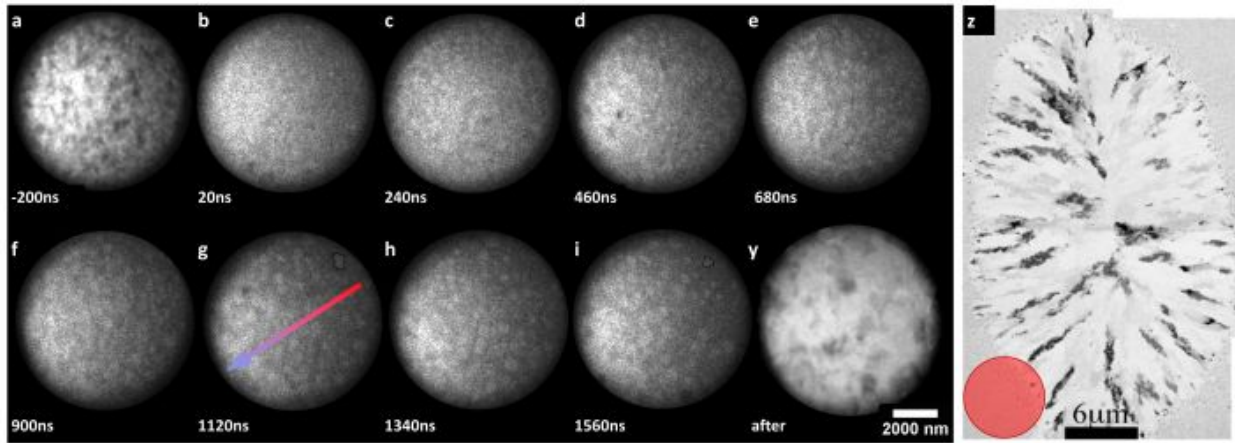


Figure 4.11: Observation of the material response to laser irradiation of an aluminum thin film capturing a two a diminishing two phase region at the edge of the Gaussian laser profile

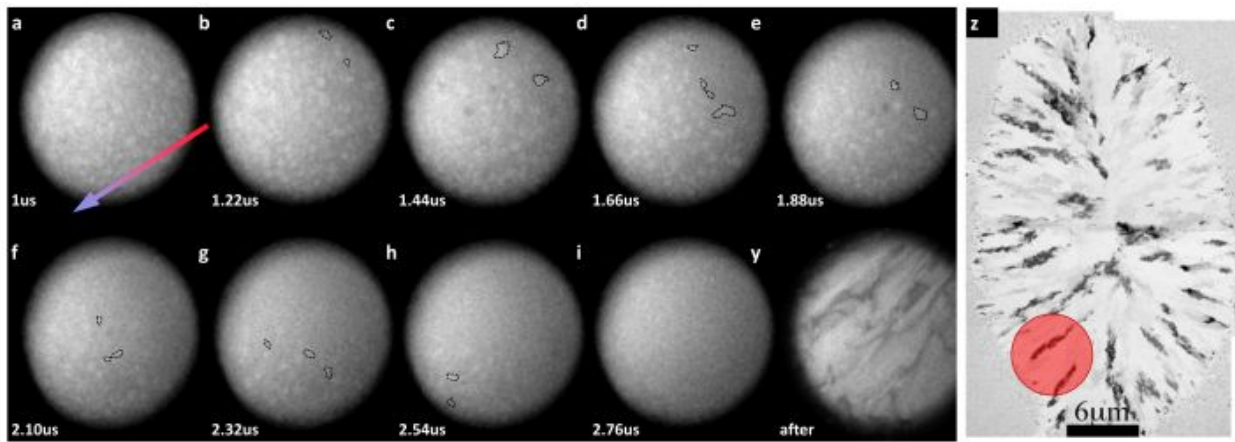


Figure 4.12: Observation of the material response due to laser irradiation in the central, hotter part of the Gaussian laser irradiation profile showing a fast diminishing melting sequence.

Fig. 4.14b-4.14f melting and solidifying of Al grains can be observed in the interface near region. Notably, the Al grains composing the interface near region are essentially stationary for the duration of 1.76 μs of the MM BF image series experiment. During the MM sequence, eventually, a morphologically flat interface is established in the BF image of Figure 4.14g. Directional solidification from the flat interface, that separates Al solid to the bottom left and Al liquid to the top right of it, commences motion in the frame of Figure 4.14h, about 4.5 μs after the initial laser pulse for melting of the Al thin film. For this set of pulsed laser induced melting experiments, using a pulse of about 270 mJ cm^{-2} energy, the directional growth of columnar morphology grains utilizes the coarsened grains established during the stage of the essentially static interface at about 4.5-4.8 μs after the initial melting laser pulse stimulus. This marks the onset of rapid solidification under directional thermal gradients and heat flux conditions, the formation of the columnar morphology Al in Zone 3. Figure 4.15 collates several selected BF images from the different MM BF image series (Fig. 4.11 to 4.14) to illustrate several important key stages during the transformation sequence of solid to liquid and subsequent liquid to solid of the Al meta thin film material in response to the PL irradiation. The BF image of Fig. 4.15a, taken after completion of the solid-liquid-solid transformation sequence indicates that the PL irradiation generated an elliptical melt pool with dimensions of $\approx 45 \mu\text{m}$ diameter along the minor and $\approx 55 \mu\text{m}$ in diameter along the major axis. Furthermore, clearly the vast majority of the solidification product that consumed the liquid Al of elliptical melt pool is comprised of columnar morphology grains, Zone3 microstructure. These columnar morphology grains are $\approx 20\text{-}30 \mu\text{m}$ long and grew radially from the outer perimeter to the center of the original elliptical melt pool under thermal gradient driven, far-from-equilibrium conditions, by directional rapid solidification with quite large transformation interface velocity. However, during the initial stages after conversion of the photon pulse energy into heat produced an elliptically shaped area of super-heated Al melt, for locations along the perimeter of this earliest stage melt pool (e.g. see red circle marker Fig. 4.15a) different conditions prevailed. The dynamic phenomena observed in the MM BF-image series in the in-situ DTEM experiments for short delay times of less than $\approx 1\text{-}2 \mu\text{s}$ after the PL irradiation of the film have to involve the final stages of melting of the solid Al. Even after the nearly instantaneous surface melting induced by the 15 ns duration PL

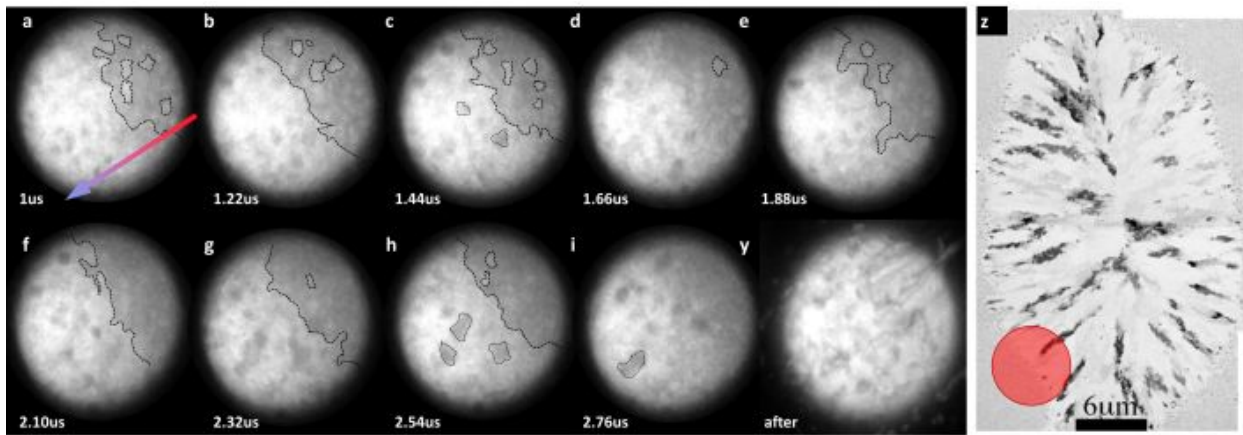


Figure 4.13: Observation of the evolving flat solid liquid interface, grain growth and changing Bragg-condition due to heat flux.

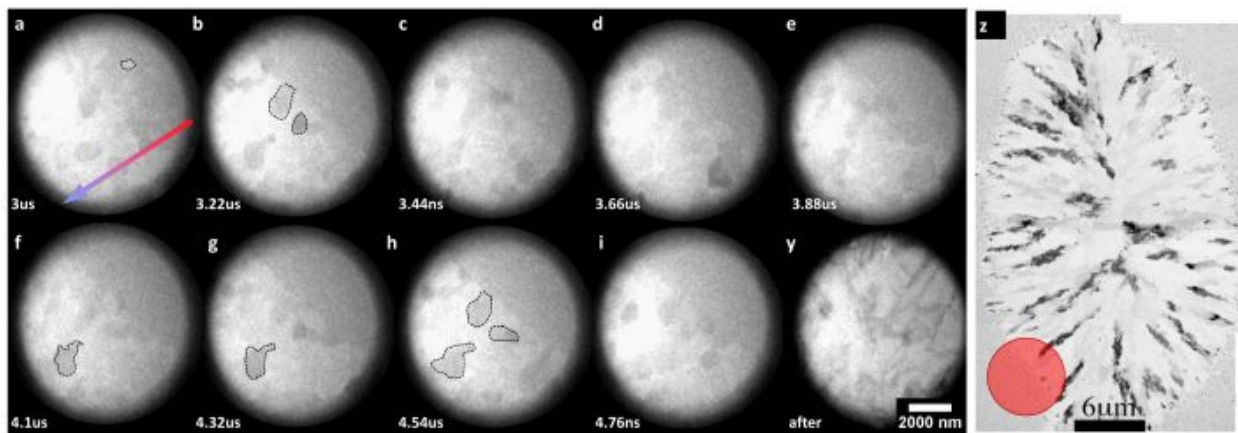


Figure 4.14: Observation of the evolving flat solid liquid interface, grain growth and changing Bragg-condition due to heat flux.

irradiation and expansion of the liquid area has been observed, producing a maximum diameter melt pool and a subsequent transition to stages of solidification, reducing again the area of the melt pool. The liquid-solid transformation interface must therefore experience an inversion in the direction of its motion and correspondingly of the sign of its velocity during the solid-liquid-solid transformation sequence. The dynamic phenomena associated with these initial stages after the pulsed laser irradiation induced transformations in the Al thin film have been determined by direct observation in the DTEM MM BF image series, such as those shown in Figure 4.11 to 4.16. The red circle in Fig. 4.15a marks an approximate observation location for the fields of view of the regions in the MM BF image series shown in Fig. 4.11-4.16. The representative observations and microstructural transformation of the initially nanocrystalline Al in response to the PL irradiation during the first about 4.8 μs time interval is summarized in Fig. 4.15 Fig. 4.15b shows three individual BF image frames extracted from Fig. 4.11 The first frame marked with a time stamp -200 ns has been obtained at a time before PL irradiation with the sample drive laser and captures the unaffected nanocrystalline microstructure of the Al-metal thin-film. The second frame was obtained in a 20 ns exposure and partially overlaps temporally with the 15ns duration sample drive laser pulse. Relative to the first frame in 4.16b the second frame exhibits a reduction in contrast, attributed to significant heating of the poly-crystalline aggregate and could potentially indicate the very first stage of melting of the surface of the 160 nm thick Al thin film [41, 42]. The third frame in Fig. 4.15b shows a large area (about 5 μm in radial width) of a two phase region with a gradient in the fractions of liquid (conversely also the fraction of solid) Al ranging from all-liquid to all-solid, i.e., from 100% liquid to 0% liquid, along the direction indicated by the arrow. The radial width of this two-phase zone reached a maximum of about 5 μm at times about 1.5 μs to 1.6 μs after the melting laser pulse and decreased at longer times (e.g. compare BF frames marked 1560 ns and 1880 ns in Fig.8). Clearly, at 1880 ns after the melting laser pulse (Fig. 4.15c) the radial width of the two-phase regions, where liquid and solid coexist, has diminished significantly by the onset of solidification at locations where the isotherms reached a critical transition temperature, the melting point, $T_{M(Al)} \approx 660\text{C} \approx 933\text{K}$. The process of crystallization and therefore the liquid-solid transformation begins by solidification of the narrowest liquid melt channels in the two-phase or mushy zone where only

partial melting of the Al thin film had been achieved. As a result of this crystal growth mode during the early stages of the solidification a HAZ comprised of considerably coarsened Al grains is produced. Fig. 4.15d (4.5 μs after irradiation) shows a fully established and distinct solid-liquid interface that is morphologically flat and sharp. Notably, there is no discernible two-phase region present at times longer than 4.5 μs after the PL irradiation of the Al thin film. Within the spatial resolution of the BF image frames, estimated at $\approx 100\text{ nm}$, it appears reasonable to conclude the liquid-solid interface is sharp and flat through the thickness of the film (160 nm here for Fig. 4.11-4.16). When the flat solid-liquid interface is established at times of about 4.5 μs after the sample irradiating drive laser pulse the solidification commences by a different crystal growth mode involving strongly directional heat flow and steep thermal gradient driven genesis of a columnar or cellular product of Al grains. Based on the series of MovieMode DTEM experiments conducted at the edge of the photon pulse power induced melt-pool the duration of the period of melting lasting from the incident of the sample drive laser pulse (e.g. 20 ns frame in Fig. 4.11) has been determined to be about 3-3.5 μs . The melting process of the polycrystalline aggregate of Al progresses along the grain boundaries, due to the heat transport away from the bulk liquid in the superheated melt pool formed by the conversion of the absorbed photon energy delivered by the sample drive laser pulse. Enveloped fully or partially by liquid, the Al grains melt from their perimeters towards their centers, quite akin to the familiar fate of ice cubes in a glass of water. This is consistent with the grain scale roughness observed at shorter delay times, e.g. 1-2 μs , after the PL irradiation of the Al thin film (e.g. Fig. 4.15b and Fig. 4.15c). Following and partially overlapping with this final stage of melting of the polycrystalline Al thin film are processes of solidification in the two-phase zone where only partial melting has been achieved. In this region, starting from the regions farthest away from the melt pool center, where isotherms reach the melting temperature, growth of solid Al crystallites (grains) that remained consumes the liquid adjacent to them, while some melting still occurs at the other end of the two-phase zone closest to the center of the melt-pool, where isotherms on average exceed the melting point of Al. It is reasonable assume that the nanosized polycrystalline Al-thinfilms exhibit grain size dependent melting points, modeling showed that the melting point for nanometer sized Al can be reduced by $\approx 45\text{K}$, [43]. The reduction in T_m for selected grains

could lead to the observed liquid-solid two phase region. The shrinking of the two phase region radially inward can be observed against the long-range or far-field thermal gradient and dominant direction of heat flow. This initial stage of solidification persists for the time interval of about 1.6 μs to about 4.5 μs , a duration of about 3 μs in the Movie-Mode DTEM experiments. The maximum lateral width of the two-phase zone with partially melted Al thin film was determined as 5 μm . Consequently, one might be tempted to conclude that the average solidification rate during this initial stage can be estimated as about $5/3 \mu\text{m} \approx 1.7 \text{ms}^{-1}$ with respect to the radial direction of the heat flux. However, this would be erroneous! This estimate neglects the presence of the solid phase in the two-phase zone and misrepresents the actual crystal growth mechanism. The channels of liquid between the solid Al crystals remaining in the two-phase zone are quite narrow ranging from 10 nm (spatial resolution limit of the BF images in MovieMode BF image series) and are at most about 100 nm (the film thickness is 160 nm here) wide. Considering the solidification of channels of a width of 100 nm by lateral growth of the neighboring solid Al grains along isotherms rather than normal to the isotherms leads to a different model for estimating the crystal growth rate responsible for the initial solidification stage. Assuming liquid Al channel of maximum width, e.g. 100 nm, in the 220 ns time interval between successive frames in the BF imaging series of the MovieMode DTEM experiments an upper limit for the growth rate with a velocity of $v \approx 0.2 \text{ms}^{-1}$ can be estimated, while similarly, solidification of a narrow 10 nm wide liquid channel by lateral growth along the isotherms would give a lower estimate of $v \approx 0.02 \text{ms}^{-1}$ for the average solidification rate in the two-phase zone. Estimates for the lateral growth distances involved in the solidification of the two-phase or partially melted zone can also be determined by limiting them against the apparent coarsening of the Al grains in this HAZ relative to the original grain size in the as-deposited film. Fig. 4.15d showed equiaxed grains with approximately constant diameters of about 450-500 nm at distances of up to about 5 μm from the zone 3 columnar morphology grains, while at larger distances grain sizes decrease gradually to that of the as-deposited Al film of about 160 nm. Lateral coarsening of an average grain in the as-deposited Al film to the maximum grain sizes observed in the HAZ implies lateral growth distance of 150-175 nm. Hence, a limit of 100 nm appears to be a reasonable estimate for the radial increase of the size of the grains.

Finally, it can be concluded that the melting stage related processes, defining the solid-liquid transformation step in the solid-liquid-solid sequence, are completed at times of about 4.5 μs after the sample drive laser pulse for the Al thin films and establish coarsened Al grains in contact with the bulk liquid of the melt pool across a quite sharp and planar interface.

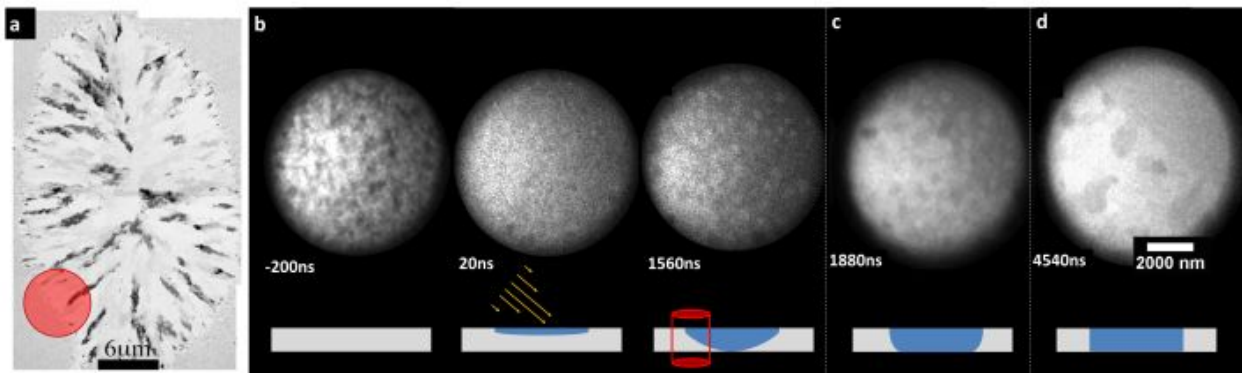


Figure 4.15: Summary of how the edge of a melt pool develops due to the irradiation of a laser with a Gaussian distribution.

4.1.3.3 Pulsed Laser induced Solidification of Al Thin-Films The MM DTEM experiments shown and discussed in the previous two sections demonstrated that after a morphologically flat interface is established in BF image of Fig. 4.14g, directional solidification commences, i.e., Fig. 4.14h. Details of the dynamics associated with columnar crystal growth during the evolution of the zone 3 microstructure have been captured in a separate Movie-Mode experiment (Fig. 4.16). The MM BF image series in Fig. 4.16 spans a duration of 1.76 μs and the growing solid advances locally of ≈ 730 nm at this section of the melt pool in the small 7 μm diameter field of view. The time-resolved image series captures the propagation of the planar, flat solid-liquid crystal interface. The melt pool appears featureless and lacks in contrast; only salient features of the CCD camera are present. The newly formed solid displays contrast features in the resulting multi-beam BF images. The HAZ consistent of small equiaxed grains. Following a grain oriented into a strong Bragg condition and exhibits darker than average contrast in the fields of view of Fig. 4.16a-4.16h it is possible to estimates the local crystal growth velocity in the early stages of solidification of the zone 3 microstructure to be about $v = 0.45 \text{ ms}^{-1}$. Changing the observational field of view and repeating the experiment under nominally identical conditions resulted in the MM BF image series shown in Figure 4.17. Measuring the dimensional elongation of a clearly discernible growing grain the velocity of the crystal growth can be estimated as $v=0.75 \text{ ms}^{-1}$. The solidification front interface curvature becomes apparent in the set of MM BF images of Fig. 4.17. Figure 4.18 captures the solidification front interface development during the evolution of zone 3 microstructure for the time interval from 18 μs to 20 μs after the PL irradiation melting pulse from the sample drive laser. The PL induced melting and solidification process was completed within 19 μs . In these later stages of the columnar morphology crystal growth related solidification the measured interface velocity has been determined as $v \approx 0.75 \text{ ms}^{-1}$. The solidification commenced through to completion by apparently accelerating motion of an interface with planar morphology. Observation of the developing interface morphology during the solidification process consists of pulse-laser irradiation and subsequent melting and solidification. The beginning of solidification of the bulk liquid in the melt pool is marked by first development of a flat solid-liquid interface composed of equiaxed grains on the solid side. The grains transform into elongated shapes, bowing out of the initially planar

and flat solid-liquid interface, forming the transition zone, zone 2 microstructure. Further crystal growth evolves the columnar morphology zone 3 microstructure by directional and rapid solidification. The transformation interface will move with a velocity determined by the heat extraction, and based on quite localized observations of small sections along the evolving solid-liquid interface, seemingly accelerating from $1.3ms^{-1}$ to about $2ms^{-1}$, while consuming the bulk liquid in the melt pool. Each individual nine-frame MM BF-image series can be used to determine the instantaneous velocity of the interface at a given position in the melt pool and is restricted to local information. Notably, the elliptical melt pools typically have dimensions of major to minor vertex of about 1.3. This implies more rapid advance of the solidification interface along the major vertex than along the minor vertex and presumably a range of local velocities for different section along the perimeter of the bulk melt pool. In order to determine reliable and statistically significant transformation front velocities and crystallization rates, lower spatial magnification imaging is needed validate the locally measured velocity of solidification during the crystallization mode evolving the zone 3 microstructure in the Al thin films after PL irradiation induced melting.

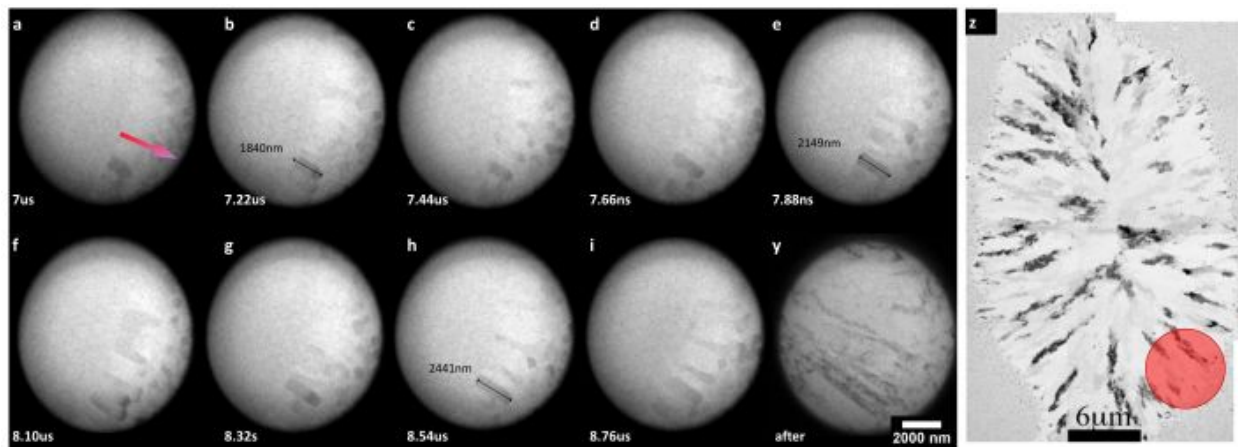


Figure 4.16: Captures the beginning of planar growth in pure aluminum thin-films in situ, the grain that show strong Bragg condition growth with $1.3ms^{-1}$.

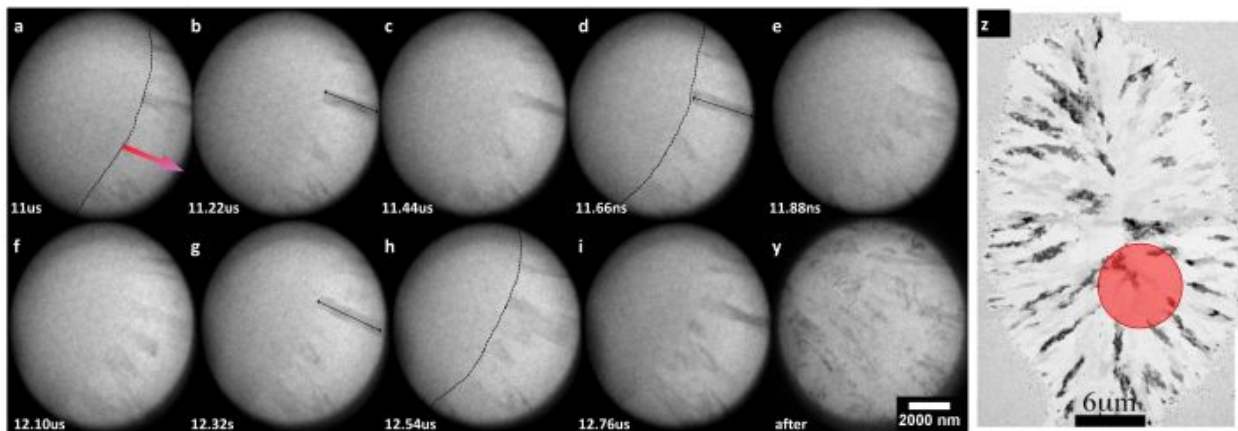


Figure 4.17: Captures the planar growth near the central region of the melt pool and the grain in Bragg condition growth with $1.6ms^{-1}$

4.1.3.4 Low Spatio-Temporal Insitu DTEM Observation of Melting and Solidification Aluminum films, up to 160 nm thick, have been prepared by e-beam evaporation using the 3 mm diameter TEM-Grid substrates. This creates the specimen geometry described schematically with the aid of Figure 4.19a- 4.19c. Figure 4.19a the plan-view of the 3 mm diameter TEM grid and the centrally located amorphous Si_3N_4 membrane covered electron-transparent window of square shape is shown. The perspective view of the TEM grid specimen in Fig. 4.19b indicates the 100-oriented single crystal Si-support in yellow, topped by the 50 nm thick amorphous Si_3N_4 membrane and 160 nm thick Al thin film in gray. The dashed line marking the trace for the cross-sectional view graphics of Fig. 4.19c. The cross-section in Fig. 4.19c shows the layered structure of the thin film specimens used here to be comprised of 200 μ m thick bulk Si substrate in yellow, which has been etched to perforation in the center of the 3 mm diameter disk, and the 210 nm thick thin film composed of the 160 nm thick Al layer and the 50 nm thick Si_3N_4 under-layer.

The region located at the edge of the electron transparent central window indicated by the open circle is shown as an enlarged detail view also in Fig. 4.19c. When utilizing the sample driver laser to create an elliptical shape melt pool in the center of electron transparent window the hot liquid in resulting melt pool will start to cool due to the dominant thermal transport through the surrounding solid Al thin film and the heat extraction geometry becomes essentially two-dimensional. Due to the nanoscale thickness and the complete melting of parts of the PL irradiated region of the Al layer of the thin-film sample, heat is primarily transported in the plane of the film with a negligible temperature gradient in the direction of the film-normal. Furthermore, contributions from radiative cooling are negligible for the short time scales of the experiments given the low emissivity of the pure Al in high vacuum. Thus, to very good approximation the heat flux is radially outward from the hot liquid established at the center of the PL irradiated regions to the cooler surrounding areas. The movement of the solidification interface is determined by the thermal diffusion towards the interface and thermal transport away from it. Hence interface movement is limited by the thermal diffusion through the solid aluminum surrounding the melt pool. However, for locations on the electron transparent window within a critical distance to the edge the heat extraction behavior may be influenced by the proximity of the thick silicon substrate that

supports the electron-transparent TEM window. The Si substrate has a thermal conductivity of about 150 to 160W/mK , which is about one order of magnitude, ten times, higher than that of Si_3N_4 and comparable to that of Al ($205\text{-}230\text{W/mK}$). Thus, for locations close to the edge of the electron transparent window the Si substrate provides an additional and substantial heat sink due to its rapid increase in thickness, e.g. within about 300 nm from the edge of the window the Si substrate reaches about 530 nm thickness.

The dynamics of the PL irradiation induced processes of melting and subsequent solidification in the Al thin film have been monitored utilizing the low-spatio-temporal setup of the DTEM in order to facilitate observations of the entire melt pool in the field of view of the frames in MM BF image series. Selecting different locations at systematically varied distances from the Si substrate edge on the electron window of an Al thin film specimen for placement of the PL irradiation the possible effects of changes in heat extraction should manifest in different interfacial dynamics for elliptical shape melt pools produced by nominally identical PL irradiation pulses. To rule out influences on the heat-extraction geometry by the thick Si substrate an experimental safe zone needs to be established for the electron transparent $500\text{ }\mu\text{m}$ by $500\text{ }\mu\text{m}$ square windows. The procedure to investigate the electron beam transparent region is schematically displayed in Fig. 4.19d. Here, the locations marked as 1) through 5) are the approximate locations for the in-situ DTEM PL irradiation and low spatio-temporal observations of the melting and solidification on the electron transparent window of the TEM grid supported Al thin film presented in this section. The shortest distances of the center of the PL irradiation pulse from the Si frame of the window are $50\text{ }\mu\text{m}$, $75\text{ }\mu\text{m}$, $100\text{ }\mu\text{m}$, $200\text{ }\mu\text{m}$ and $250\text{ }\mu\text{m}$ for the locations marked as 1), 2), 3), 4) and 5) respectively. Figure 4.20 shows the results of MM BF images series DTEM experiments performed with the low-spatio-temporal resolution set of parameters of 50 ns exposure time per image frame and $2500\text{ ns} = 2.5\text{ }\mu\text{s}$ inter frame delay time for locations 1)-5). In these MM BF image series the entire melt pool is captured in each image. The location of the nearest corner of the square shaped electron transparent window and thus the Si substrate support frame is indicated schematically in Fig. 4.19d. Figure 4.20a shows the melt-pool interface development after PL irradiation for the location of the central spot of the laser profile at a distance of $50\text{ }\mu\text{m}$ away from the thick silicon substrate (location (1) in Fig. 4.19d). The

50 μm distance is measured from the peak of the laser pulse to the closest edge of the transparent window. The electron-opaque region is visible in the top part of the Movie-Mode image series in Fig. 4.20a, as marked by the dashed lines. The image sequence is timed such that the first 50 ns duration imaging electron pulse coincides with the 15 ns duration shallow Gaussian profile PL irradiation pulse of the sample-drive laser with a diameter of 135 μm ($1/e^2$). The first image in the sequence defines the starting time ($0 \mu\text{s} = t_0$) for the subsequent melting and solidification process observation. The melt-pool development from 0 μs to 12.8 μs shows the interfacial evolution due to non-uniform radial heat extraction from the super-heated Al thin film melt pool into the cooler surroundings. The close proximity of the Si substrate results in an asymmetrical heat extraction geometry, which is reflected in the asymmetrical shape melt pool development. The temporal evolution of the melt-pool differs for directions along the major and minor axis of the nominally elliptically shaped PL irradiated area. Clearly, the melt-pool is distorted and solidification completes at a very short time, at about 12.8 μs after the PL sample probe PL irradiation pulse at t_0 , presumably due to the increased rate of cooling associated with the proximity of the Si substrate. The melting and solidification sequence shown in Fig. 4.20b has been obtained for location (2) on the electron transparent region of the Al film at a distance of about 75 μm from the Si substrate. For the nominally identical PL irradiation parameters the time to complete solidification increased from 12.8 μs in Fig. 4.20a to about 17.9 μs . Obvious melt-pool shape distortions cannot be discerned for this location on the electron transparent window. The MM BF image series for PL irradiation at locations (3) to (5), i.e., at distances of 100 μm , 200 μm , and 250 μm are shown in Fig. 4.20c, Fig. 4.20d and Fig. 4.20e respectively. No significant changes in melt-pool dimensions, shape, or solidification time have been observed for these latter three locations at distances larger than 75 μm from the edge of the Si substrate support frame. Minor differences in the time to completion of the solidification process, as indicated by the slight variations noticeable in the melt-to-solid fraction in the images obtained at 17.85 μs exist. These minor differences are attributed mainly to the $\pm 5\%$ fluctuations in pulse-to-pulse power of the sample drive laser system. Solidification completes reproducibly by 20 μs after the PL irradiation at t_0 always in the symmetry center of the elliptical shape irradiated area. Symmetry distortions of the melt-pool geometry are

not detected in Fig. 4.20c-4.20e. It appears reasonable to conclude that at distances larger than $75\ \mu\text{m}$ from the Si support frame the PL irradiation induced melting and solidification dynamics are reproducible. Figure 4.21 collates the $2.6\ \mu\text{s}$ image frames of the MM BF image series in Figure 4.20, showing in detail the changes in shape, dimensions, and extent of the diffuse contrast two-phase region (see previous section). Fig. 4.21a shows a strongly distorted melt-pool shape. Interestingly, the melt-pool interfaces at locations labeled (1) and (2) in Fig. 4.21a capture a non-uniform solid liquid interface behavior. Along the melt pool interface section near the label (1), closest to the Si substrate support frame edge of the electron transparent window, solidification is already in progress at $2.6\ \mu\text{s}$ after the PL irradiation pulse from the sample drive laser, while at the opposite side melt pool interface with the solid Al film near label (2) melting is observed simultaneously. The presence of the two-phase partially melted region, a mushy zone of crescent shape, giving rise to diffuse contrast at a gray level in-between the darker liquid Al and the brighter solid Al (Fig. 4.20 and Fig. 4.21a), clearly indicates that thermal transport was less rapid at the side of PL laser irradiated elliptical area labeled (2), the locations at the largest distances away from the Si substrate support. In the image of Fig. 4.21b for the $2.6\ \mu\text{s}$ image obtained for PL irradiation at a location $75\ \mu\text{m}$ away from the electron transparent window edge, a smaller mushy zone at the region labeled (1) and larger size mushy zone at the region labeled (2) have been observed. The different sizes of the mushy zone of partially melted Al for the latter location at a distance of $75\ \mu\text{m}$ from the window edge with the Si support imply reduced but still significant asymmetry in the heat extraction at the opposite sides of the melt pool along the major axis. In comparison to Fig. 4.21a and Fig. 4.21b the $2.6\ \mu\text{s}$ image frames in Fig. 4.21c -Fig. 4.21e show very elliptically symmetric melt-pools without distortions associated with asymmetries in the heat extraction geometry. The image contrast line profiles along the major axis of the melt pools for Fig. 4.21a-4.21e are shown in Fig. 4.21f. Here, the normalized and smoothed (LOWESS) intensity profiles show the influence of the different heat extraction geometry resulting from the proximity of the Si substrate support at the edge of the electron transparent window. The intensity plots for the PL irradiations at distances of $50\ \mu\text{m}$ (black) and $75\ \mu\text{m}$ (red) show significantly reduced distances for the darkest liquid Al region, indicating smaller melt pool dimensions and with asymmetrical melt

pool developments and transformation interface behavior, which would be consistent with shorter total solidification times. For the locations closest to the Si Substrate, marker (1) in Fig. 4.21b and Fig. 4.21f, the intensity profiles for the 50 ns exposure images of the melt pool for the locations at 50 μm (black in Fig. 4.21f) and 75 μm (red in Fig. 4.21f) from the Si substrate are considerably steeper than those for larger distances from the Si substrate. Consistent with an enhanced heat extraction rate for the former two resulting narrower in smaller mushy zone developing during the melting after PL irradiation. For PL irradiation at distances of 100 μm or more from the silicon substrate edge the melt-pool dimensions, inter-facial behavior, and the time required to complete solidification are reproducible and unaffected by possible effects from the massive Si substrate support frame on the heat flow. Figure 4.22 compares the experimentally measured melt pool dimensions Aluminium melting and solidification experiments with theoretical modeling of the photon-field distribution. Figure 4.22a displays the 500 μm by 500 μm electron transparent TEM window where the boundaries of the x-y-plane determine the beginning of the thick Si support frame of the TEM specimen. The blue dashed ellipses mark the location and experimentally measured melt pool dimensions from the solidification experiments at locations (1)-(5) (Fig. 4.22b). Furthermore, the photon distribution fields from a photon pulse with a Gaussian shape of $\sigma = 135 \mu\text{m}$ at $1/e^2$ incident at 45° are superimposed as ISO-intensity lines ranging from 100% (red) to 13.5% (grey) of the peak fluence. Location (1) marks the irradiation experiment where the center of the melt pool is located 50 μm away from the silicon edge, i.e. in close proximity of a larger more massive heat sink. Here, a large portion of the photon distribution covers the thick Si substrate. Thus, the heat generated in the Al top-layer from the photon-phonon interaction can be transported away through the z-direction and the x,y-direction of the Al film and substrate. When an irradiation takes place at a greater distance to the substrate the heat generated in the Al -top layer can only be transported away along x- and y-direction. Effectively the heat extraction geometry changes from the 2D case to a more complex 3D situation. The change in heat extraction geometry leads to a change in the long range thermal gradient, rendering it asymmetric with respect to the symmetry center of the nominally elliptical shape area modified by the incident PL irradiation. The solid-liquid interface regions close to the massive Si support, which acts as an additional heat sink, show

altered inter-facial behavior. At location (1) a significant amount the photon field covers the silicon substrate at the top and on the right side. Thus, the melt pool interface region closest to the Si substrate (top right side of the melt pool), which are shown in Fig. 4.22b near marker (1) exhibit the largest deviations from the nominally expected elliptical shape melt pool. At location (2), 75 μm away from the silicon substrate, the measured melt pool dimensions, blue dashed line, with the superimposed ISO-intensity lines for the PL irradiation profile are also shown for 75% and 13.5% of the peak-fluence. The 75% ISO-intensity line closely aligns with the experimentally measured melt pool dimensions. The 13.5% ISO-intensity line delineates effectively the extend of the photon-field-distribution. The melt pool dimensions measured from location (2) showed a diminished mushy zone along the major axis near the top of the melt-pool edge (Fig. 4.21a,4.21b). This indicates that the thermal gradient established by the photon-phonon interaction along this direction in the Al layer is changed by the proximity to the Si substrate. Location 3)-5), 100 μm to 250 μm away from the TEM window edge with the Si substrate, show identical elliptical melt-pool geometries and scale. Considering the overlap of the simulated photon field with the experimentally measured resultant melt pool dimensions clearly shows that the PL irradiated area only covers the Al layer that is supported by the 50 nm Si_3N_4 membrane, where an idealized 2-D heat-extraction model can be applied to very good approximation. The safe-zone for artifact free PL induced melting and subsequent solidification experiments in the DTEM using the windowed TEM grid specimens includes locations on the square electron transparent window for which the incident photon profile does not overlap with the Si support frame, e.g., locations (3)-(5) in Fig. 4.22. The simulated Photon-Pulse distribution established the same safe-Zone requirements as the observed experimental results.

Figure 4.23 summarizes the quantitative measurements of the changes in melt pool dimensions and the interfacial velocity for the transformation interface, averaged along the entire perimeter of the melt pools obtained by direct observation from in-situ DTEM experiments shown in Figure 4.20 for the locations (1)-(5). Figure 4.23a shows the elliptical area reduction over time. The elliptical areas were used to calculate an average radius of an equivalent circular area and its change over time is displayed in Fig. 4.23b. Furthermore, a polynomial best fit was employed to determine analytical functions that describe the ve-

locity measurements between $5.1\ \mu\text{s}$ and $17.8\ \mu\text{s}$ after PL irradiation. The first measurement points, marked as (a) in Fig. 4.23b, were excluded due to difficulty in discerning and accurately detecting the growth interface in the 50 ns exposure TEM bright field images of the melt-pool obtained at the shorter times. The extrapolated functions were utilized to create the velocity plots shown in Fig. 4.23c. The velocity profiles for location (1) (black line) shows a constant acceleration throughout the solidification process observed from 2.9m/s^{-1} to 3.3m/s^{-1} . Velocity measurements for the PL irradiation experiment from location (2)-(5) also show a steady acceleration of the interface and fall into the same range of velocities that increase from initially $\approx 1.2\text{m/s}^{-1}$ to 2.5m/s^{-1} at the end of solidification. These are fast crystallization front velocities and consistent with RS conditions in Al. Experiments on identical thin film of Al that utilized nominally identical PL irradiation pulses to induce melting for different locations on the electron transparent window area with systematically varied distances from the Si support frame at the edge of the window have been performed. Using the low spatio-temporal-resolution mode of the DTEM instrument to observe the entire melting-solidification processes in a single Movie-Mode series of BF images the investigation showed incontrovertibly that the solidification behavior of pure Al differs depending on the location of the PL irradiation on the electron-transparent $500\ \mu\text{m} \times 500\ \mu\text{m}$ square window. In cases of close or too close proximity of the thick silicon substrate relative to the center of the PL irradiated region the thermal field evolution and heat extraction is altered such that the melt pool interface development is asymmetrical and the solidification times are significantly reduced relative to the artifact-free conditions a safe locations on the electron transparent window where reproducible results can be obtained. Hence it has been ascertained that in-situ PL irradiation experiments performed with the DTEM here deliver reliably reproducible and quantifiable behaviors regarding the melt pool evolution and dynamics for locations on the electron transparent window where the center of the laser power is located at distances of $75\ \mu\text{m}$ or more from the window frame edge. This is an important finding in the context of the novel experimental set ups used here for in-situ studies with the DTEM. DTEM in-situ observations and measurements obtained from the direct observation of irreversible transformation dynamics of PL induced melting and subsequent solidification in Al based metallic systems can deliver reliable and robust quantitative data for experimentation in the safe

zone of the electron transparent window. For DTEM in-situ experiments performed with improving temporal resolution, i.e., shorter image frame exposure times (shorter duration electron pulses from the photon induced pulsed electron source of the DTEM) and reduced inter-frame delay times (higher frequency of image acquisition), decreasing total temporal observation windows result and it is critical to have certainty regarding the reproducibility of the material response to ensure artifact-free studies of the dynamical behavior of irreversible phase transformation that are time sensitive.

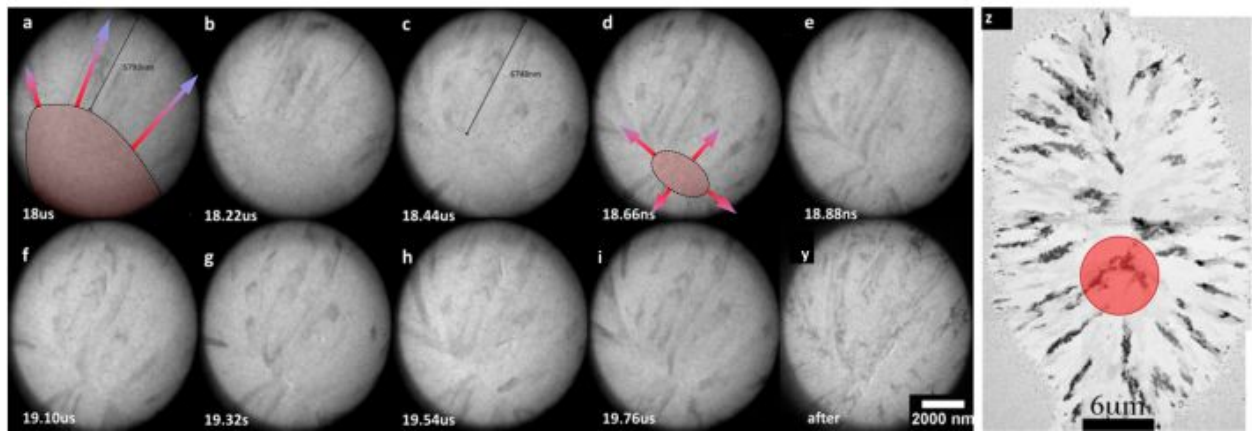


Figure 4.18: Captures the last 660ns of solidification, the curvature of the melt pool is clearly visible and the grain that shows slight Bragg condition growth with around 2ms^{-1}

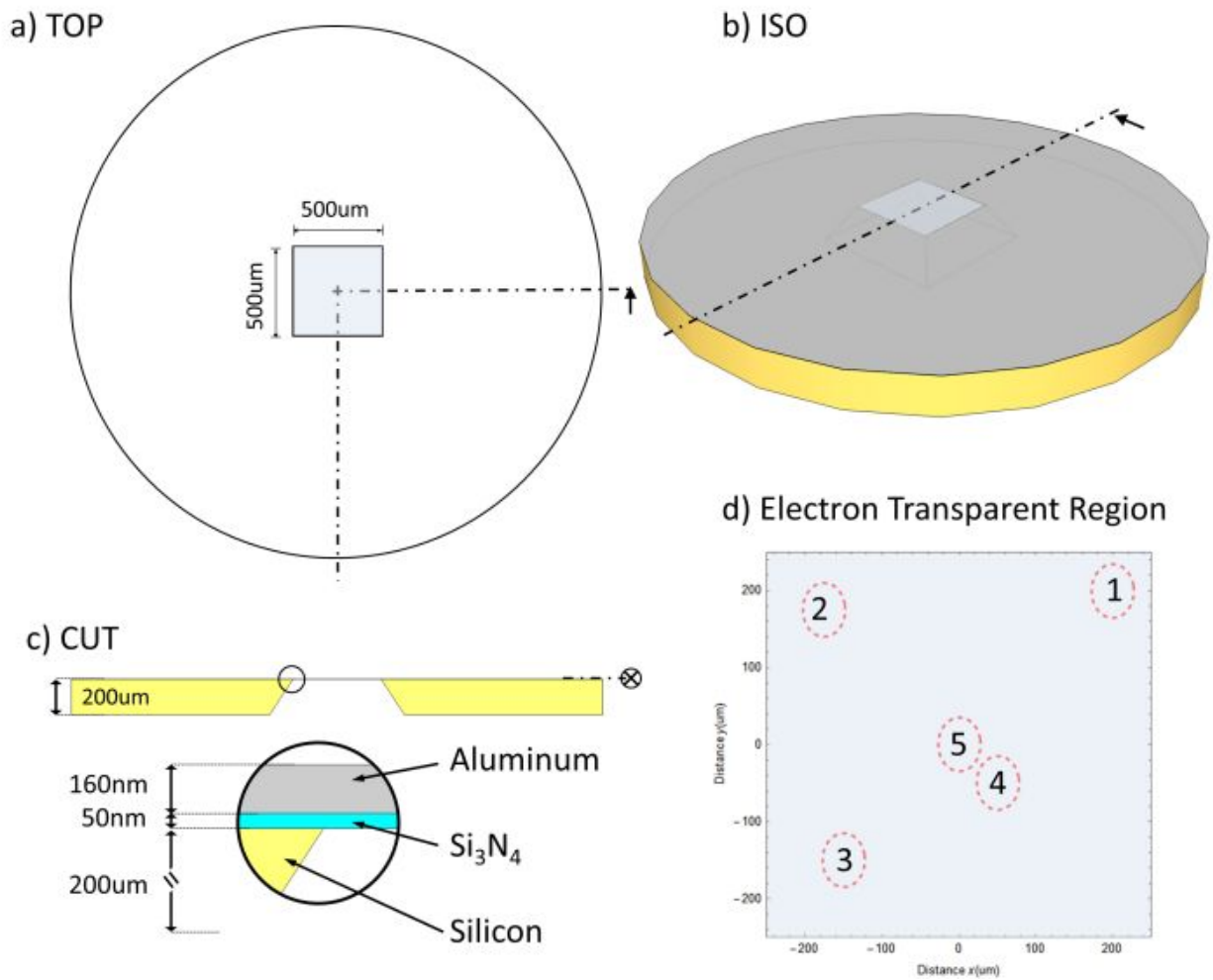


Figure 4.19: Schematic of the thin film specimen geometry for the Si frame and α - Si_3N_4 membrane square window TEM grids: a) Plan or Top View; b) ISO-view or projected perspective view; c) Cross-sectional CUT view and magnified schematic of the layered thin film structure; d) Enlarged detail view of the 0.5mm x 0.5mm square electron transparent window region, x and y in μm , dashed red lines mark the dimensions and locations of the melt pools created on the TEM window by pulsed laser irradiation at various distances away from the edges of the silicon substrate as measured along the diagonal, i.e., the corner points, in 1) at 50 μm , 2) 75 μm , 3) 100 μm , 4) 200 μm and 5) 250 μm for the location at the center of the electron transparent window.

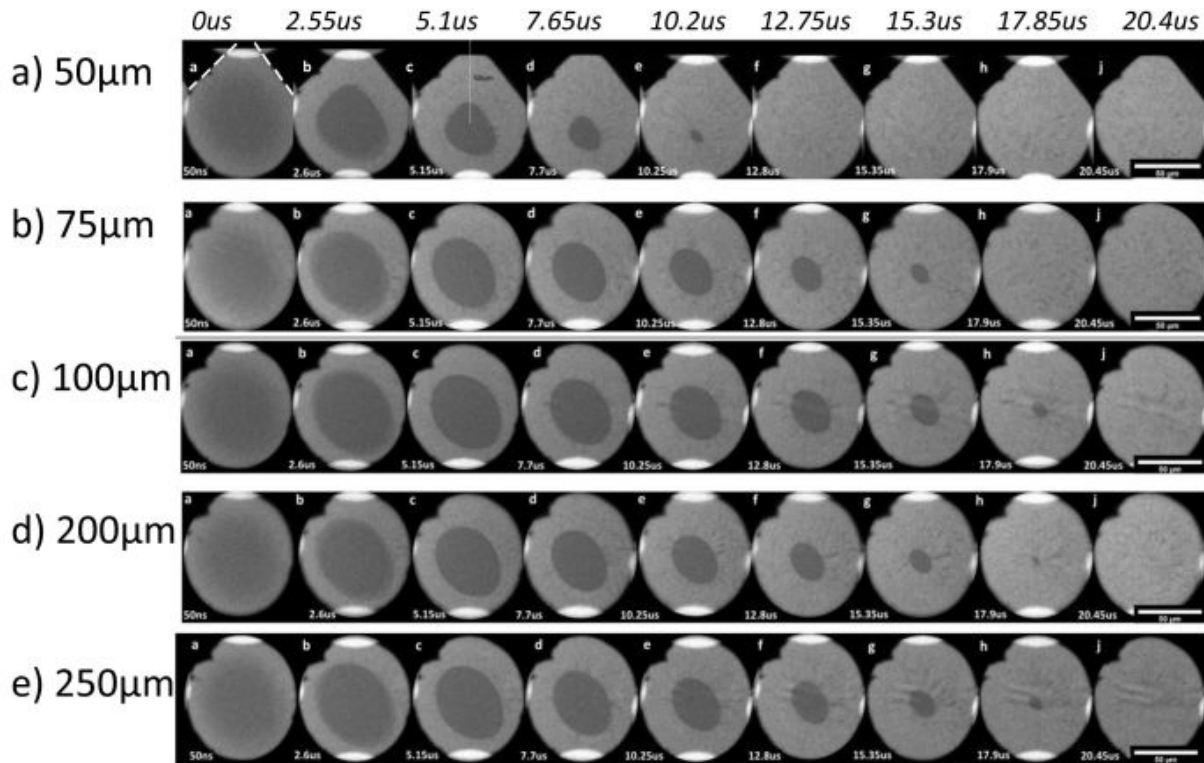


Figure 4.20: Low-Spatio-Temporal observations of location dependent Solidification experiments

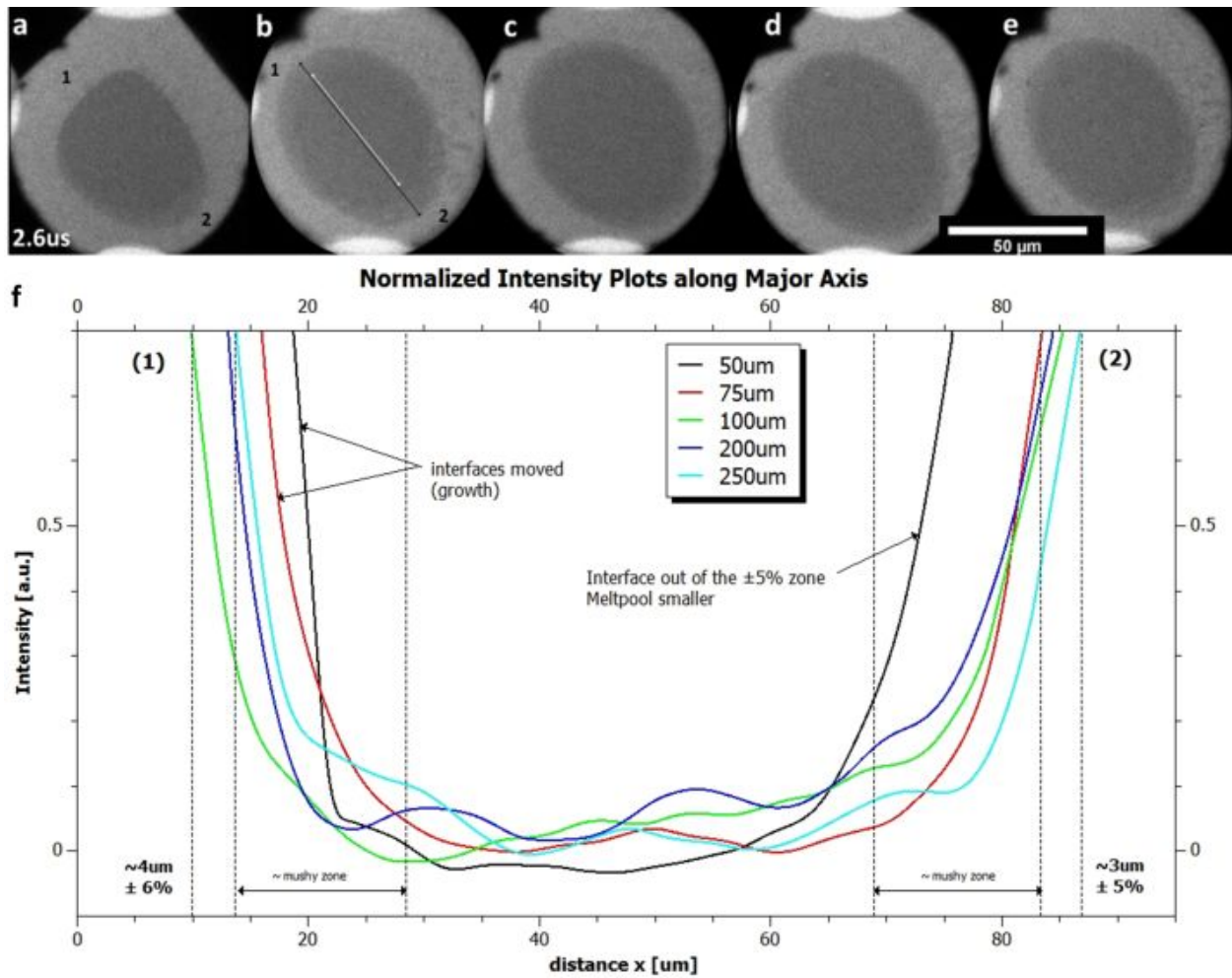


Figure 4.21: Showing the influence of irradiation location dependent heat extraction profile. Here, **a)** severely distorted melt pool 50 nm away from the thick silicon substrate, **b)** smaller melt pool near (1), **c),d),e)** identical melt pool sizes and shapes, 75 μm to 250 μm distance from the silicon edge. **f)** shows the intensity curves measured along the major axis of the meltpool

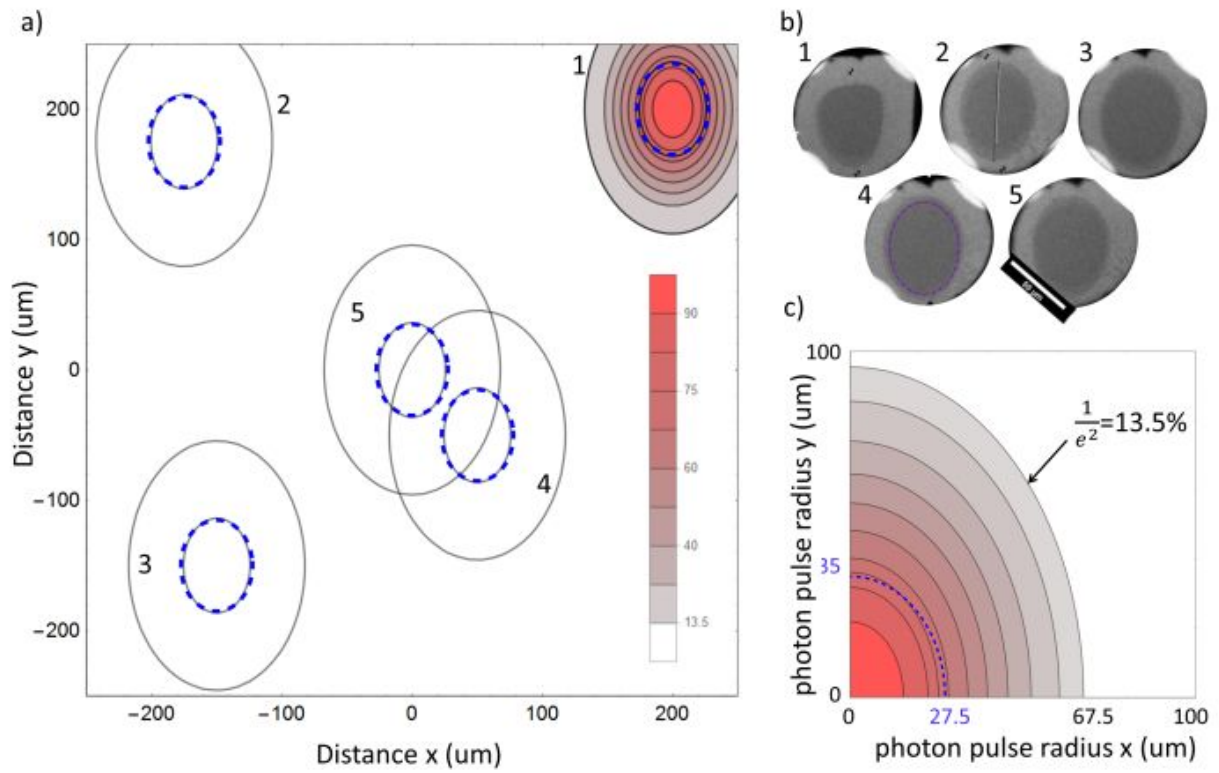


Figure 4.22: **a** Electron transparent region of the TEM window with melt pool dimensions and calculated photon distribution field. **b** Created Melt pool for the individual location 1-5 **c** Photon field distribution along major and minor radius.

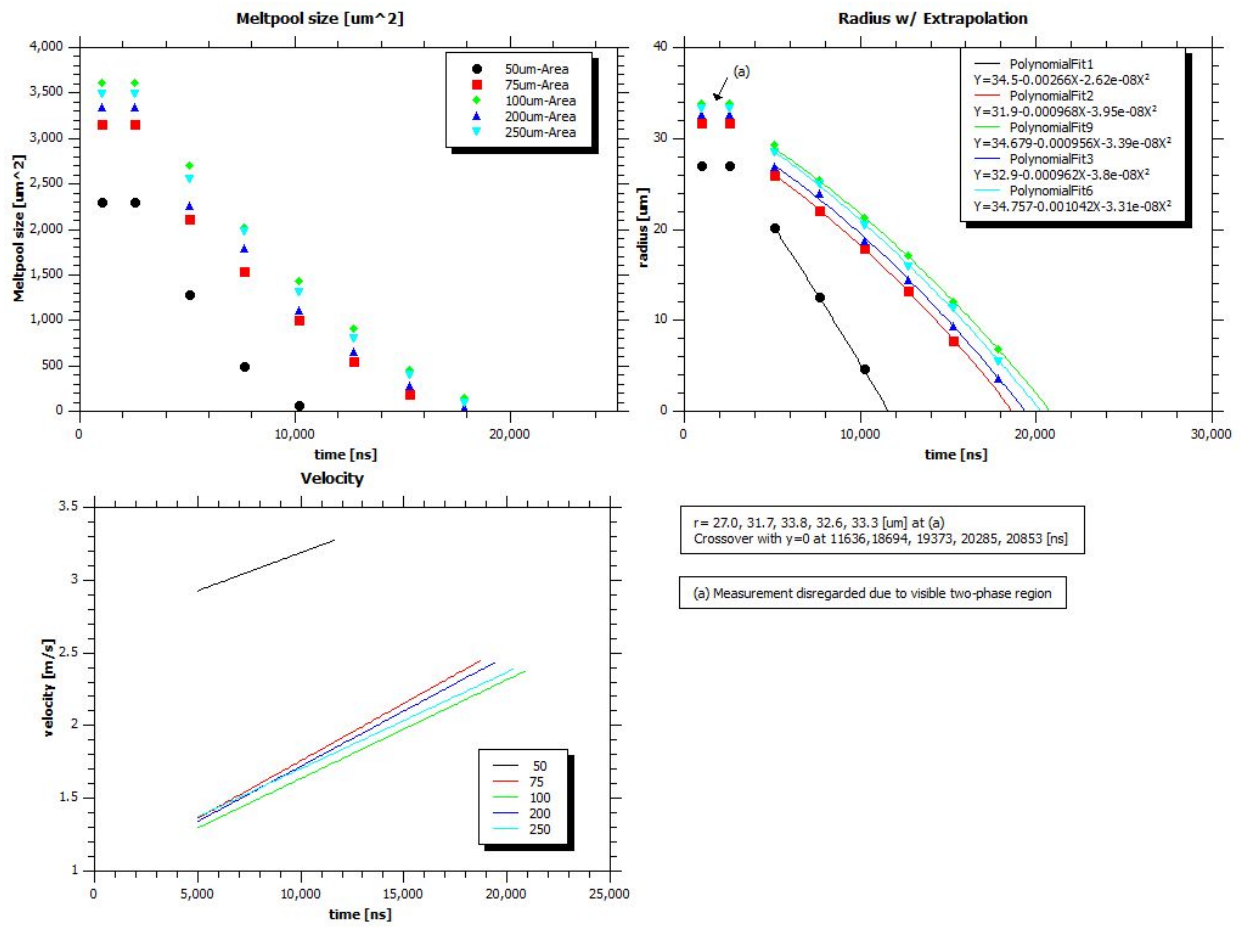


Figure 4.23: Velocity evaluation for the experimental observation in Figure 20

4.1.3.5 PED Studies of In-situ DTEM PL modified Microstructure Obvious photon pulse shape differences due to different laser projection and focusing systems utilized in the set up for ex-situ PL melting and in-situ DTEM PL induced transformation experiments establish different far-field thermal gradients in the thin film specimens. Here, we analyze the HAZ near a melt pool edge created by the shallow Gaussian shaped laser pulse of the in-situ DTEM sample drive laser system will be presented. It is important to compare quantitatively the microstructures established in the Al thin films in response to the PL induced transformation sequences in the DTEM experiments with those that obtained for the ex-situ PL irradiation experiments (e.g. Section 4.1.2.1 and in particular Fig. 4.8).

Figure 4.24 collates IPF based PED-OIM maps for the Al grains showing the HAZ (Zone 1) of the Al thin films after DTEM in-situ PL irradiation experiments. Figure 4.24a shows the IPF maps for the film normal direction (z direction) and the associated pole figures for the Al grains. The Al grains exhibit a strong $\{111\}$ texture with respect to the film normal. The thermal gradient in this region is assumed to decrease along the y-direction as marked for reference in Figure 4.24a. In order to ascertain possible texture effects of the heat extraction directionality the PED-OIM data set for the Al-grains has been rotated to display the poles parallel to the y-direction in Figure 4.24b. The Al film does not exhibit discernible texturing with respect the heat extraction direction in the film plane. Similar to the case of the ex-situ PL irradiated Al thin film, the HAZ (zone 1) maintains the texture established during the e-beam evaporation, the as-deposited state. PED-OIM based IPF-maps for Zone 3, the directional the growth zone are shown in Figure 4.25. After PL irradiation of the Aluminum thin foil in the DTEM induced melting, the subsequent solidification processes involve directional crystal growth radially towards the center of the melt-pool of the grains that maintain or slightly increase their width in at the transition from zone (2), where occlusion processes occur, to (3). This is entirely qualitatively analogous to the conclusions drawn from the microstructural analyses performed for the ex-situ PL irradiation induced transformations in the Al thin films. The IPF-map for the film normal directions of Fig. 4.25a shows the central part of an elliptical melt pool and the associated pole figures. The strong $\langle 111 \rangle$ texture present in the as-deposited condition is maintained. The interface growth velocity has been measured to be $\approx 2-2.5 \text{ms}^{-1}$, indicating RS conditions for advancing

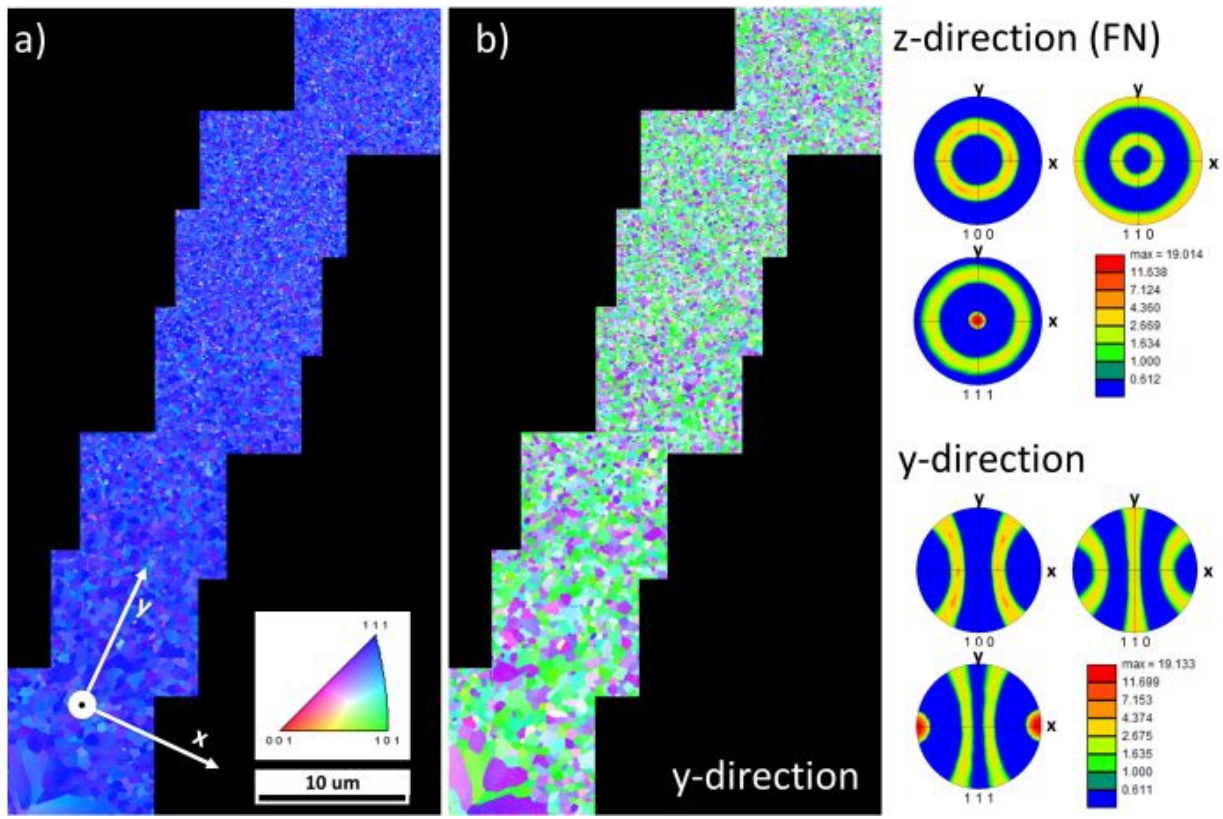


Figure 4.24: PED investigation of zone 1,2 and 3 i) PED orientation image map with the film normal parallel to the electron beam or (z direction) ii) plotted is the x direction perpendicular to the heat-flow iii) and the y-direction parallel to the heat flow direction

transformation interfaces facilitating the directional Al crystal growth. During strongly directional crystal-growth process anti-parallel to the heat extraction direction preferred growth directions might be observed for pure Al, as has been reported for other substances [44]. The PED-OIM data set has been rotated into the solidification direction and the resulting IPF-map is displayed in Fig. 4.25b. A preferred crystal growth orientation can not be identified for these columnar morphology Al grains. Figure 4.26 shows a collage of virtual bright field (vBF) images from zones 1 to 2, the HAZ and transition zone. The grain size distribution along the y-direction. The grain size distribution changes as a function of distance from the boundary to zone 3, i.e., along the y-direction, the direction of the dominant directional heat flux, have been determined. The average grain size displayed in the inset in Fig. 4.26 was determined by measuring the minor and the major axis of the grains contained in each of the area slices (a)-(q). The corresponding grain size plot shows that up to 15 μm away from the melt pool edge, the zone 3 boundary, the average grain-size in the HAZ is approximately constant at ≈ 640 nm. This plateau of a constant grain size indicates that this region has experience a similar temperature field cycle. Notably, the average grain size in this region is about eight times (8x), i.e., nearly an order of magnitude larger than the film thickness. This quite extraordinary coarsening of the grain scale in the polycrystalline Al thin film might indicate that these regions have undergone a solid-liquid-solid phase transformation and could correspond to the two-phase zone that partially melted in response to the PL irradiation. Typically grain sizes in ISO-thermally treated thin-films grow no larger than perhaps two to three times of the film thickness. At larger distances along the y-direction the grain size decreases to a plateau of ≈ 350 nm at a distance from the melt pool edge of 30-35 μm . With further increasing distance to the melt-pool edge the average grain-size then decreases monotonically until the starting condition of 150 nm is reached at distances of about 80 μm away from the melt-pool edge.

Comparing the grain size plot in Fig. 4.26 with that of Fig. 4.8 shows qualitatively quite similar details. However, significant quantitative differences regarding the maximum grains size in the HAZ and more importantly in the spatial extension of the plateau in the grain size and the HAZ are noted for the in-situ DTEM and ex-situ PL induced transformation experiments. Although the melt pool creation and assumed liquid temperatures can be assumed to

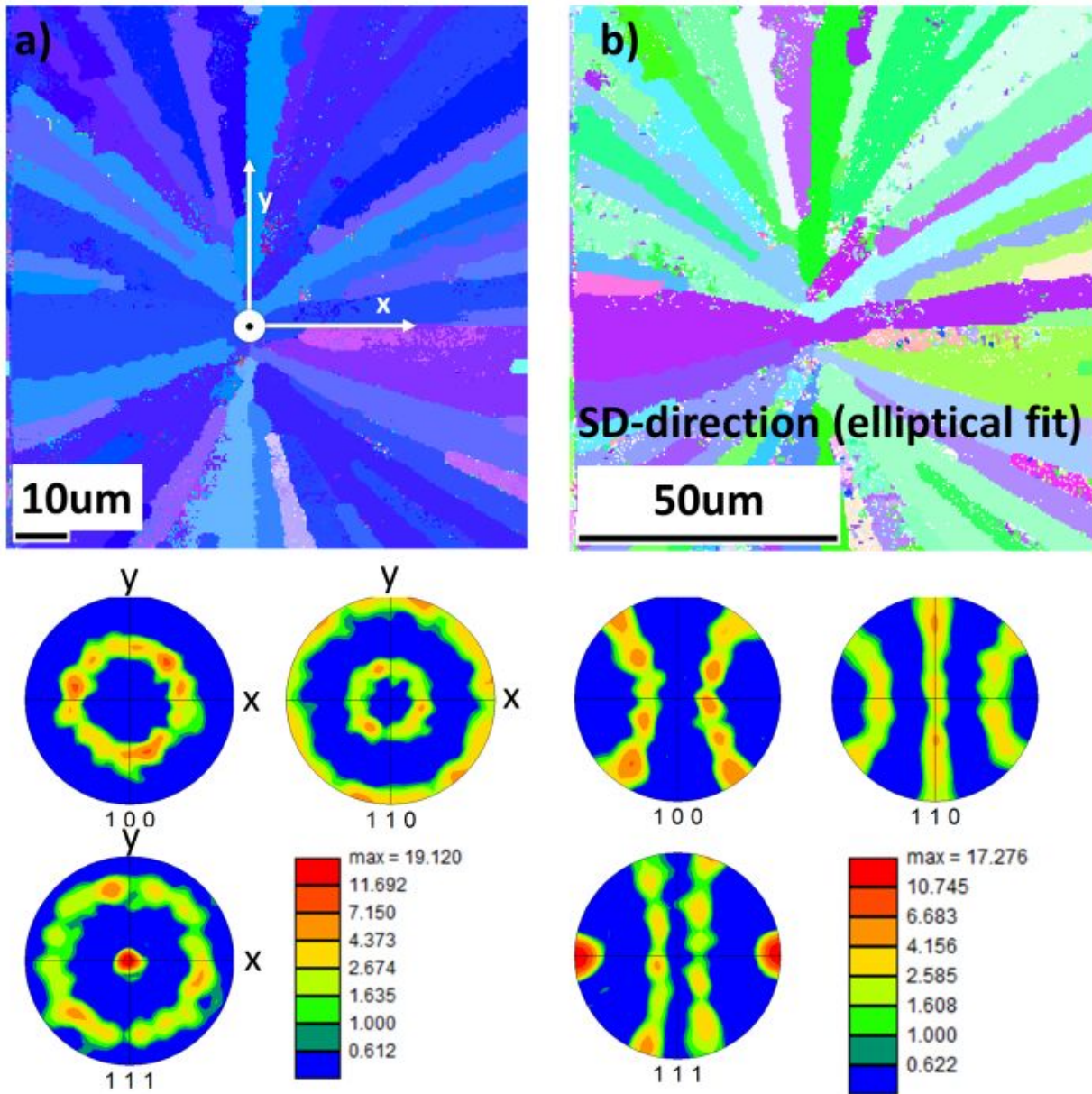


Figure 4.25: Investigation of the growth zone of in-situ irradiated Al thin film **a** Orientation map with the plotting direction parallel to the Film normal and associated pole figures showing the reoccurring $\{111\}$ fiber texture **b** Orientation map shows the growth direction for the individual grains in the growth zone.

be very similar in the in-situ and ex-situ experiments, the grain scale modification defining the HAZ extends to much large distances from the zone 3 boundary the melt pool edge for the shallow Gaussian shaped laser pulse of the in-situ DTEM experiments. The top-hat laser profile of the ex-situ PL experiments produces a more confined HAZ up to 30 μm away from the melt pool edge. The Gaussian laser profile on the other hand modifies the microstructure up to 70-80 μm away from the melt pool edge. The grain sizes found in the vicinity of the melt pool edge seem in both cases very large, 500-600 nm and 550-650 nm for the ex-situ and in-situ experiments respectively. This region, immediately adjacent to the melt pool edge, could be the region observed in the high spatio-temporal observation experiments (Fig. 4.13, 4.14) that consisted of solid-liquid phase mixture where the ratio between liquid and solid is fairly uniform in this region and the grains might grow equiaxial. For regions in the HAZ beyond 15 μm away from the melt pool edge a solid-liquid phase mixture may still have been present during the in-situ DTEM PL melting experiment. However, at these locations the liquid to solid ratio seems to be decreasing rapidly and the partially melted two-phase (solid and liquid) zone presumably persisted only for very short duration. For regions beyond distances of 40 μm to the melt-pool edge the monotonically decreasing grain-size can be attributed to solid-state based thermally induced coarsening involving lattice diffusion processes.

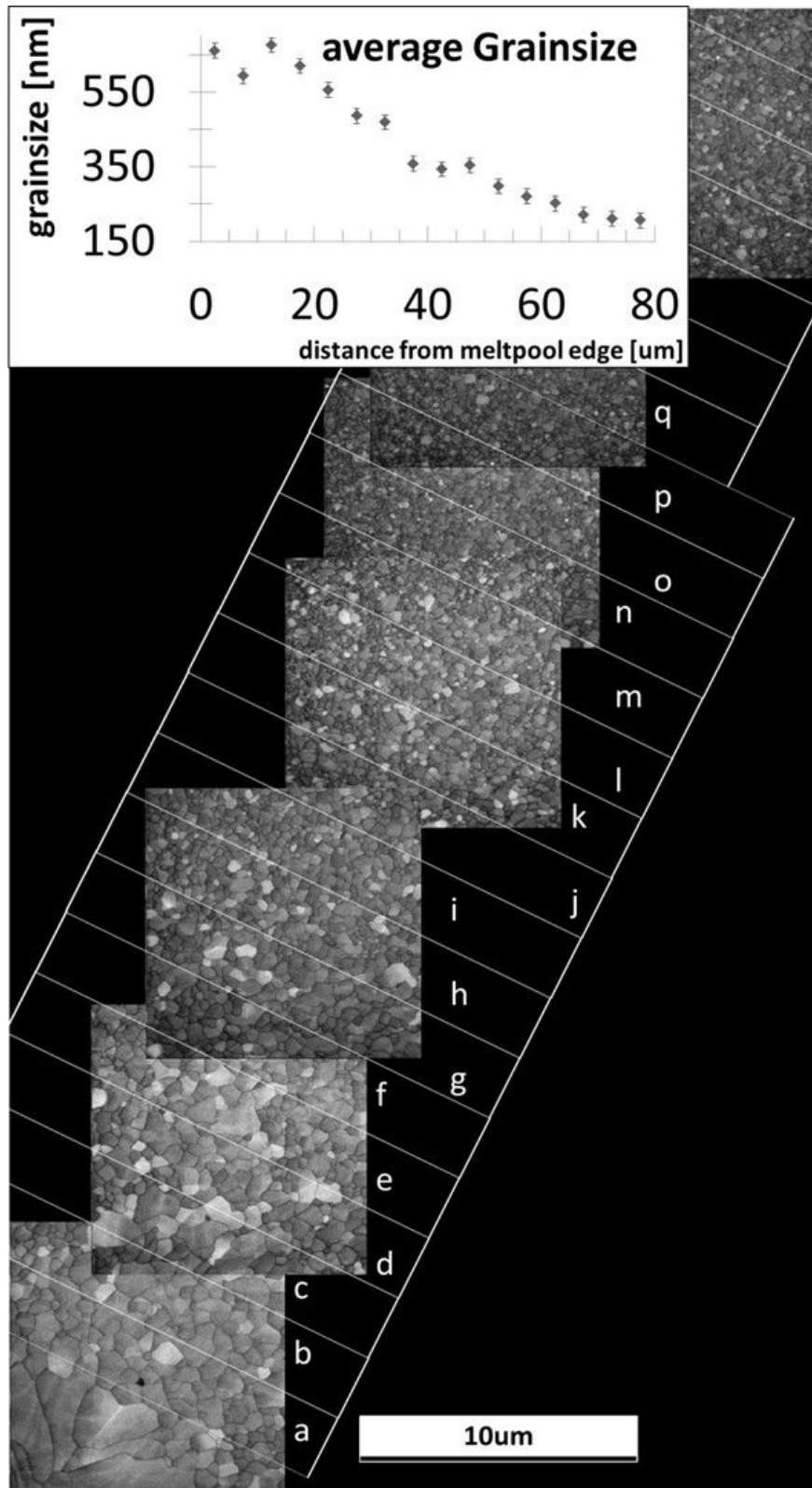


Figure 4.26: Virtual Bright field (vBF) of the region up to 80 μm away from the melt pool edge (bottom left) indicated are the segmented regions (a-q), the average grain size plotted is plotted in the insert

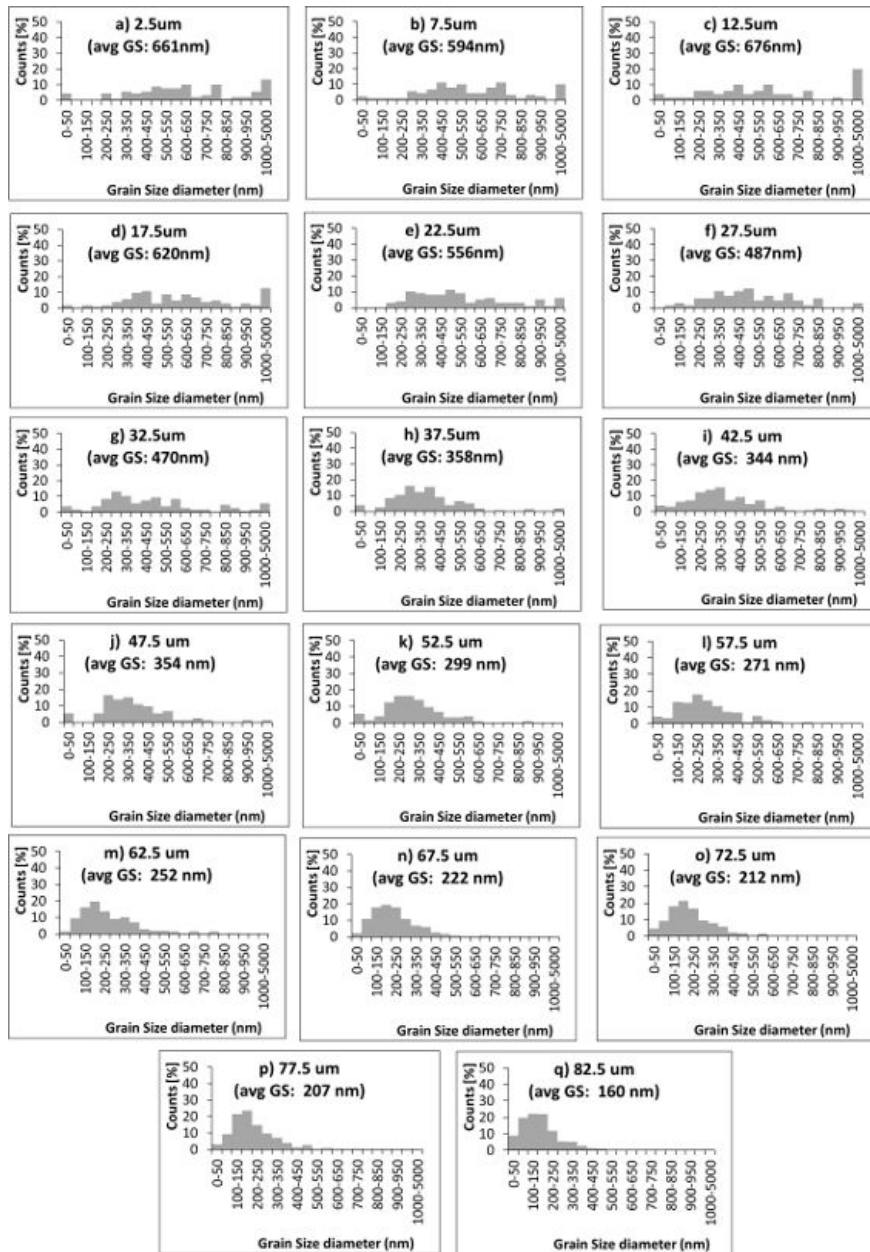


Figure 4.27: Grain size distributions complementary to Figure 4.26

4.1.4 Summary and Discussions

Aluminum thin films were deposited with a thickness of 80 nm to 160 nm by electron-beam evaporation onto 50 nm thick amorphous support films of 500 by 500 μm windowed TEM grids (Ted Pella Inc.). The thin films were deposited in high vacuum at a rate of 2-2.5 nm/s with substrate held at room temperature, i.e. 298K. The deposited film is continuous and composed of nano-crystalline grains with an average grain-size of 150 nm which was confirmed via regular dark field imaging and the novel PED-OIM system. A preferred crystal orientation of $\langle 111 \rangle$ parallel to the film normal and $\langle 100 \rangle$ randomly oriented about $\langle 111 \rangle$ is clearly apparent and expected for the given evaporation conditions of $\frac{T_M}{T_S} = 3$. The Al thin foil can be successfully irradiated utilizing the in-situ instrument (DTEM) and the ex-situ experimental setup (PITT). Resulting microstructural features and morphological zones observed in ex-situ and in-situ experiments are very similar to bulk CW-laser or welding experiments. The interface velocity dependent growth-modes and associated observed morphological zones can be summarized as zone (1), the heat affected zone, zone (2), a transition zone, and zone (3), the directional crystal growth zone. PED-OIM was applied to acquire statistical significant data sets of crystal-orientation from the non-ISO-thermal non-uniform microstructural zones. Grain size measurements identified an 5 μm wide band of equiaxed grains surrounding the growth zone for the ex-situ irradiated thin foils. Further, a 20 μm wide band of equiaxed grains was found around the melt pool of the in-situ irradiated thin foil. The bands of large equiaxed grains around the melt pool indicate a liquation zone/two phase region during melting and in the beginning of the solidification sequence. The size of the band is determined by the photon-distribution field, if the laser pulse is sharply defined the surrounding grains are less subjected to equiaxed growth and the initial thermal gradient is much steeper. The growth zone is composed of long ribbon shaped grains growing anti-parallel to the heat-extraction direction, and the average grain width of these ribbons is comparable with the average grain size of the grains surrounding the melt pool. PED measurements of the growth zone, did not indicate a preferred growth direction.

High-spatio-temporal observation of pulsed laser induced melting and subsequent solidification shows the melting behavior of nano-crystalline Al with an unprecedented ns-temporal

resolution. A diminishing two phase region (solid-liquid zone) was captured in the early stages of melting, the movement of this diffuse interface was shown to be parallel to the heat extraction direction. A flat interface between solid and liquid is fully established at $\approx 3 \mu\text{s}$. Until a flat, almost stationary interface is established heat is extracted from the melt pool throughout the surrounding microstructure leading to grain-coarsening in zone (1). The onset of solidification was captured at about $5 \mu\text{s}$. Local grain growth can be measured and shows an accelerating interface.

Low spatio-temporal observation experiments successfully demonstrated the influence of the thick Si support frame on the solidification behavior of rapid solidifying Aluminum. Experiments that utilized nominally ($\pm 5\%$) identical PL irradiation pulses to induce melting for different locations on the electron transparent window area with systematically varied distances from the Si edge of the TEM-transparent window showed that an influence on the solidification behavior is noticeable if the irradiated area is too close to the Si edge. A safe distance to the Silicon support frame is necessary to achieve reproducible results. The solidification interface velocity development for solidifying Aluminum was measured to have a constant acceleration of $\approx 0.07 \text{ m s}^{-2}$.

4.2 HYPOEUTECTIC AL-04CU ALLOY

4.2.1 As -deposited State: Al-04Cu Thin films

Microstructural changes accompanying the phase transformation subsequent to pulsed laser irradiation induced melting requires a thorough investigation of the starting condition of the alloy thin film materials studied here. Important metrics, such as grain-size distribution, film-thickness, possible underlying texture as well as the fractions, spatial distribution and composition of the crystalline phases present, need to be recorded prior to the irreversible transitions to establish microstructural benchmarks. For the hypo-eutectic composition Al-Cu film with nominal composition of Al-04at.%Cu, referred to as Al-04Cu, the starting microstructure after the electron beam evaporation consisted of nano-crystalline

granular features (Fig. 4.28a). The image contrast is dominated by crystallographic orientation changes in the field of view, depicting differently oriented crystallites, grains. Utilizing a large selective area aperture a diffraction pattern collected from the field of view is displayed in Fig. 4.28b. The nearly continuous ring-type SAD pattern indicates a nano-crystalline nature of the thin film. Azimuthal integration of intensity along constant scattering vector magnitudes for the SAD pattern produced the intensity line profile (PASAD) plotted as a function of diffraction length k vs intensity shown as an inset in Fig. 4.28b. The PASAD profiles (Fig. 4.28b inset and Fig. 4.28c) can be interpreted akin to data of a Θ 2 Θ -type X-ray diffraction scan. The Bragg peaks labeled in blue are consistent with the face-centered cubic crystal structure, space group $Fm - 3m$, of Al, while the peaks labeled in red are consistent with the inter plane spacings of Al_2Cu with tetragonal crystal structure, space group $I\frac{4}{m}cm$. After deposition the Al-04at.Cu thin films are comprised of equiaxed nanoscale grains of the equilibrium phases of α -Al and stable θ - Al_2Cu . Figure 4.29 shows the results of scanning transmission electron microscopy (STEM) annular dark field (ADF) imaging in combination with compositional analysis by X-ray energy-dispersive spectroscopy (EDS) mapping. The ADF-STEM contrast image in Fig. 4.29a exhibits strong dependence on the atomic number density, e.g. it shows strong Z-contrast effects. The small bright features, which indicate an elevated amount of heavier atomic number elements, i.e., Cu, and darker larger features indicate lighter atomic number average elemental composition, i.e., reduced Cu fraction. It is reasonable to interpret the former as Al_2Cu and the latter as Al solid solution grains, given that the SADP data clearly identified the presence of the equilibrium α -Al and θ - Al_2Cu phases. In Figure 4.29a the areas of interest in the field of view marked with numbered green rectangles have been analyzed by EDS STEM scans, which utilized a 0.5 nm diameter electron beam probe. The results of the elemental composition averaged over these small selected areas are listed in Fig. 4.29b. The overall composition for the entire field of view would be expected to be representative of the alloy composition, nominally Al-04Cu, and was determined to be 4.1 at.% Cu. The compositions obtained by quantification of the EDS analysis of the select smaller areas in the polycrystalline hypo-eutectic Al-04Cu thin film can be misleading, since through-the-film-thickness overlap of multiple grains of the different phases cannot be excluded. In the heat-map representation of the Cu composi-

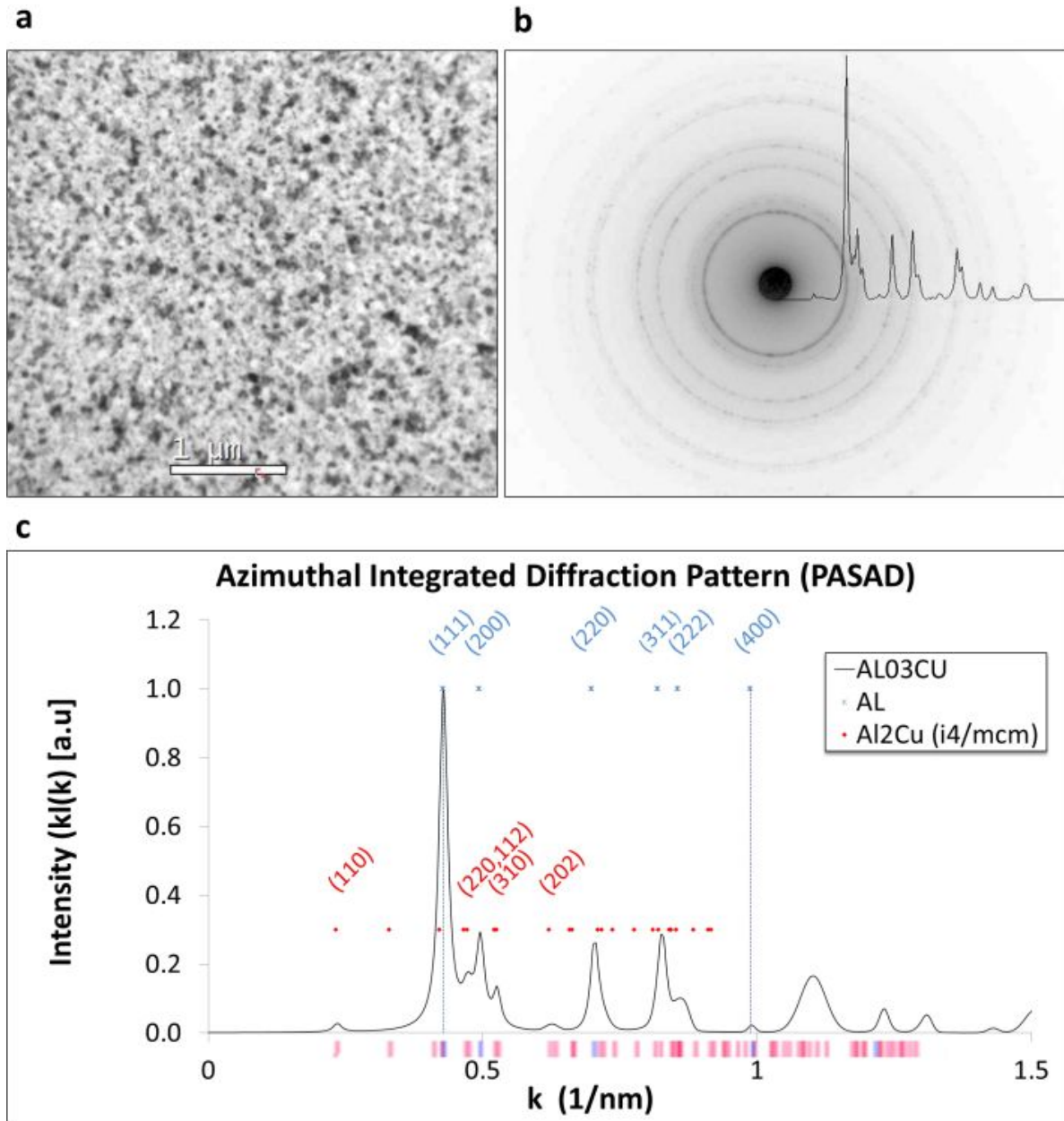


Figure 4.28: **a** TEM Bright Field image of the evaporated Al-Cu alloy thin film; **b** Ring-type selected area diffraction pattern obtained at a 0° specimen tilt and superimposed azimuthal integrated line profile arising from the diffraction rings; **c** The azimuthal integrated intensity plot profile (intensity vs. magnitude of scattering vector k). The diffraction maxima not associated with the aluminum reflections (marked blue) are consistent with θ -Al₂Cu (marked red)

tion in Fig. 4.29c one pixel represents the average composition obtained from a 16-voxel size area for which the sub nm electron-probe and step-size EDS spectra have been summed to reduce the noise levels. The Cu based heat map displays a composition range from black at 0 at.% Cu to red at 19 at.%Cu. For the Al_2Cu θ -phase the expected Cu content is about 33 at.% at room temperature. The reduced maximum Cu-content detected in the heat-map for Cu composition in the polycrystalline aggregate hypo-eutectic alloy thin film of nominal thickness of 80 nm would be consistent with the effects from through-thickness overlap of the nano-crystalline Al and Al_2Cu grains. Essentially, the surrounding Al solid solution grains dilute the true composition of the embedded Al_2Cu grains in the resultant EDS spectra and Cu-composition heat-map. Hence, it appears reasonable to conclude that the hot red shaded regions in the heat-map for the Cu composition, Fig. 4.29c, represent regions of the hypo-eutectic alloy thin film. The SADP of the as-deposited alloy thin film indicated a two-phase mixture of α -Al and θ - Al_2Cu , which is reasonable considering the thickness of the Al-Cu thin film and the evaporation conditions [45]. Precession electron diffraction orientation image mapping (PED-OIM) by computer-controlled, automated sequential collection and indexing of diffraction patterns from preselected scanning areas, facilitating determination of the spatial distribution and fractions of the crystal phases present in the Al-04Cu alloy thin films with nanometer spatial resolution (Fig. 4.30a). The acquired PED data sets have been indexed utilizing the α -Al, meta-stable θ' - Al_2Cu and stable θ - Al_2Cu phases, with space groups $Fm - 3m$, $I_m^{\frac{4}{m}}2m$ and the $I_m^{\frac{4}{m}}cm$, respectively, leading to the phase distribution map shown in Fig. 4.30b. The phase area fractions have been determined by the PED-OIM as 94% α -Al, 0.4% meta-stable θ' - Al_2Cu and 5.6% stable θ - Al_2Cu phase. Given the uncertainty levels in the PED-OIM based phase fraction determination, the very small fraction of data points as θ' - Al_2Cu is not significant and is concluded that the hypo-eutectic film contained 94% α -Al and 6% θ - Al_2Cu . Under equilibrium solidification behavior the expected phase fractions can be estimated using the lever rule to be $\approx 88\%$ α -Al and $\approx 12\%$ θ - Al_2Cu . The reduced second phase fraction seems to be reasonable given the characterization technique that has been employed and the complex matrix-precipitate relationship. Smaller second phase precipitate might not give raise to enough diffraction to be detected by the automated system. The average grain size and the associated grain size distributions of

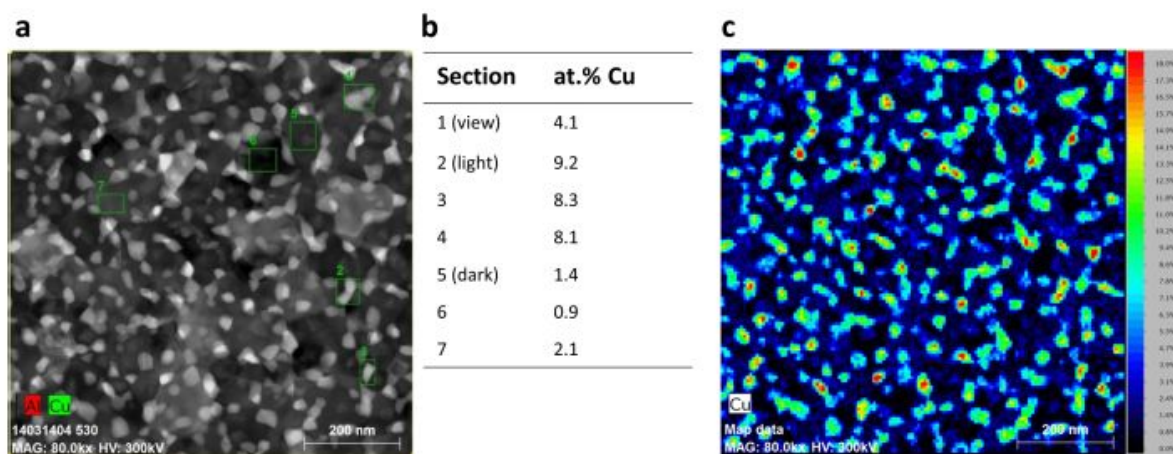


Figure 4.29: **a** ADF STEM Z contrast image where light contrast signifies a higher amount of Copper atoms, the chemical composition of the selected areas can be found in **b**, **c** displays the atomic copper concentration arising of the individual analyzed voxel intensity spectras in form of a temperature map, where red is around 18at.%Cu and black is around 0.0at.% Cu

the as-deposited alloy thin film have been determined by statistically significant analysis of the grains presenting in the virtual bright field (vBF) image constructed from the PED-OIM data sets. The resulting grain-size distribution plot for the 2 m by 2 m field of view in Fig. 4.30a is shown in Fig. 4.30c. An average grain size of about 50 nm has been determined for the as-deposited Al-04Cu thin film. Using the grains indexed as α -Al by the PED-OIM analysis inverse pole figure (IPF) based orientation maps have been prepared as shown in Fig. 4.31. Fig. 4.31a is an IPF-based orientation map for the thin-film normal. Each grain is color-coded according to the unit stereographic triangle based legend, where shades of blue correspond the $\langle 111 \rangle$ corner, shades of red to orientations close to $\langle 001 \rangle$ and shades of green to orientations close to $\langle 110 \rangle$. The black features in the color-coded IPF-based orientation map are the locations for the θ - Al_2Cu grains. The pole figures obtained from the IPF map for the α -Al grains exhibit a strong $\langle 110 \rangle$ -texture with respect to the thin film normal, with a narrow orientation spread to within $\pm 5^\circ$ away from the film normal. The in-plane orientations within the population of Al grains are essentially random distributed rotationally about the direction parallel to the film normal. Thus, the $\langle 111 \rangle$ direction exhibits an even and continuous pole density distribution about the preferred $\langle 110 \rangle$ film normal. Complementary IPF-based orientation maps for in-plane rotations are displayed in Fig. 4.31b and Fig. 4.31c. The absence of a clear dominance of a given shade of color indicates that there is no in-plane preferred orientation. In the as-deposited condition the thin films of the hypo-eutectic Al-Cu alloy show significant differences to the pure Al metal thin films. The Al-04Cu alloy thin films exhibit a strong $\langle 110 \rangle$ -fiber texture with respect to the film normal, while for the Al thin films instead a $\langle 111 \rangle$ -fiber texture exists. Notably, the $\langle 110 \rangle$ -texture of the alloy thin films would allow for a close-packed direction, e.g. $[\bar{1}10]$, the plane normal for $(\bar{1}10)$, and a cube-direction, such as $[001]$, the normal to (001) , to lie in the plane of the thin-film. Unlike in the case of the Al thin films, this implies the possibility for selective and preferred crystal growth during solidification of the alloy Al-04Cu thin films, which has been observed for dendritic growth in solidification for cubic metals.

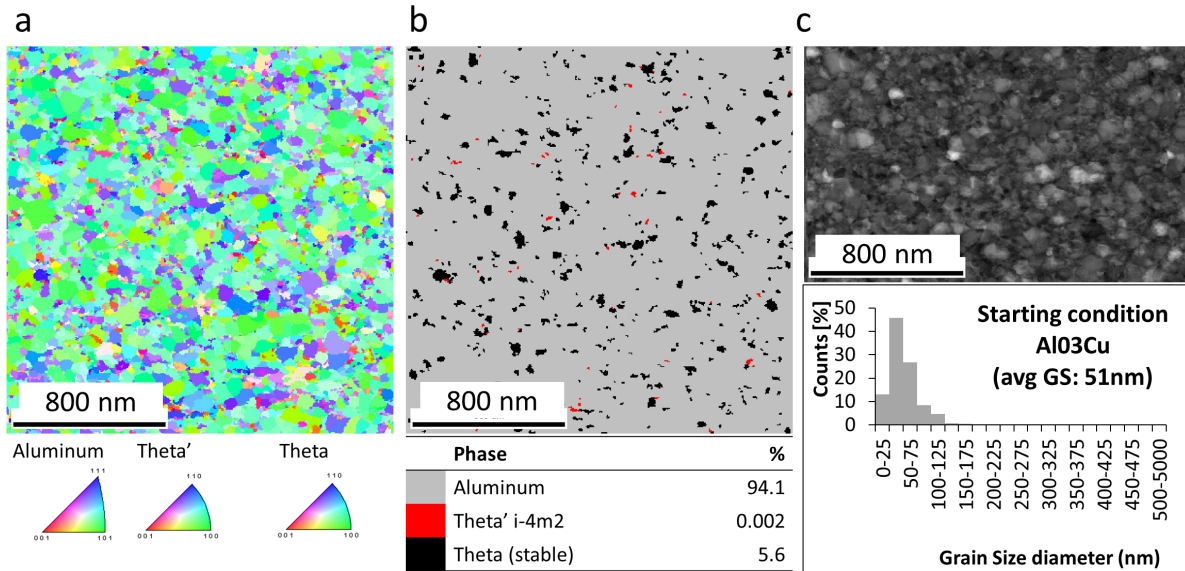


Figure 4.30: **a** inverse pole figure (IPF) based orientation maps for the three phases in the evaporated starting condition for the 4.1% Cu Film **b** resulting phase map displaying 94% Al and 6% θ -Al₂Cu **c** vBF and resulting grain-size measurement displaying the nanocrystalline nature of the evaporated thin film

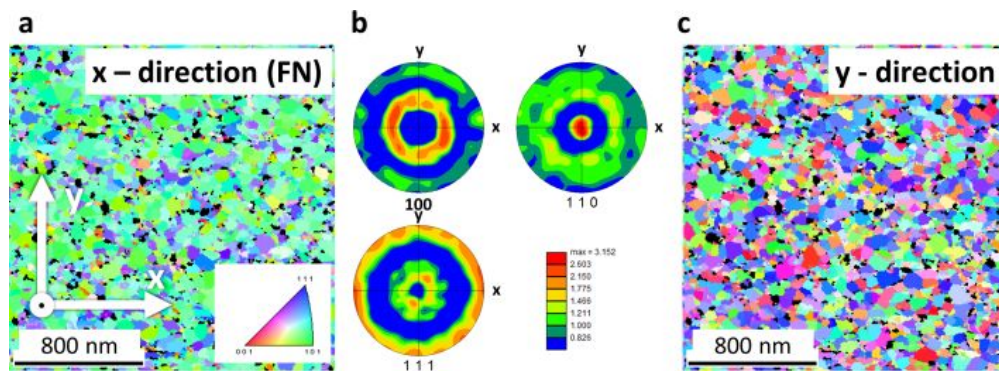


Figure 4.31: Inverse pole figure based orientation maps and associated 100- 110 and 111-pole figures showing a preferred orientation where the 110 direction of the Al crystallites are parallel to the film normal and the 111 directions are rotated around 111, **a** displays the electron beam parallel to the film normal (z-direction) **b** when the electron beam is parallel to the x-direction and **c** the z-direction

4.2.2 In-situ and Ex-situ PL irradiated Al-Cu Thin films

Compared to the RS experiments performed with the elemental Al thin films the fluency of the in-situ and ex-situ laser systems were reduced to achieve full melting in the Al-04 at. %Cu alloy. Utilizing fluency as high as in the Al experiments resulted in destruction of the alloy thin films by PL irradiation. Figure 4.32 presents TEM and STEM images of the characteristic details associated with the microstructures of the hypo-eutectic Al-08 at. %Cu and Al-04 at. %Cu alloy after successful melting by the PL irradiation and subsequent rapid solidification for the case of in-situ DTEM and ex-situ experimentation. Figure 4.32a shows the post-mortem microstructure of an Al-08 at. %Cu alloy that has been subjected to PL irradiation in the DTEM and illustrates the location of the different morphological zones (1)-(4). The collage of post-mortem TEM-BF images in Fig. 4.32a shows an overview of the area melted by the photon irradiation pulse, for hereon referred to as the melt-pool for short, in an in-situ experiment for the Al-08 at. %Cu film. The major and minor axis diameters of the elliptically shaped melt-pool resulting from the photon irradiation pulse ranged from 25 μm by $\approx 30 \mu\text{m}$ for this particular Al-08 at. %Cu alloy sample. In contrast later irradiated Al-04 at. %Cu alloys ranged between 70 μm and 50 μm in the dimensions for major and minor axis. Notably, the laser profile of the photon pulse incident on the sample in the in-situ DTEM experiments can be described by a Gaussian function with $1/e^2$ diameter of $\sigma = 135 \pm 5 \mu\text{m}$, which defines a significantly larger area on the film than the dimensions of the resulting melt-pools, e.g. Fig. 4.32a. In the TEM micrograph of the overview in Fig. 4.32a four morphologically different solidification micro-structure zones can be identified. Three of them are similar to the solidification microstructure zones, namely Zone 1 to Zone 3, observed in the pure Al PL induced RS experiments. For the alloy thin films Zone 1 can be described as a heat affected zone (HAZ) with grains that have significantly grown in size due to exposure to heat from a superposition of thermal energy imposed by the photon field and the radial outwards directed unidirectional heat flow from the superheated melt of the melt-pool. In the transition zone, Zone 2, adjacent grains grow into the melt in a kinetically competing fashion. In Zone 2 the grains grow anti-parallel to the unidirectional long-range thermal gradient established in the alloy thin film, elongating them towards the center of the

melt-pool. Concomitantly they also grow laterally, expanding in width essentially parallel to isotherms. As a result, some grains grow wider in the plane of solidification at the expense of their neighbors. This occlusion process prevents further growth for the latter. The grains that successfully emerge from the transition zone advance along the dominant growth direction, radially toward the center of the melt-pool, anti-parallel to the thermal gradient in the alloy thin film, and form Zone 3 in Fig. 4.32a, Zone 3 is the directional growth zone with grains of columnar morphology. Following the ribbon shape grains of Zone 3 along the crystal growth direction during this stage of the solidification a new micro-structural morphology appears that cannot be observed in the Al thin films during the PL induced RS processes. Notably, a small number of grains mostly located at the vertex of the elliptical melt-pool (e.g. dark contrast grain marked by label 4 in Fig. 4.32a) transition from the columnar-type growth mode into a new type crystal growth mode. The new growth-mode accessed by these select grains produces the banded morphology in the microstructure at the center of the melt-pool (Label 4 in Fig. 4.32a). Only a few grains compromise the center of the melt-pool, Zone 4, as illustrated in the overview of Fig. 4.32a and in higher magnification detail in the STEM micrograph of Fig. 4.32c. The three separate grains outlined by the dashed lines in Fig. 4.32c emerge from Zone 3 of columnar growth, grow very rapidly laterally (along isotherms) to occlude neighboring columnar morphology Zone 3 grains. Only three grains then constitute one half, about 50% of the area of the melt-pool associated with Zone 4, which exhibit internally a banded morphology. The banded morphology can be described as single crystal grains that are comprised of bands of super saturated solid solution alternating with bands of two-phase micro-constituent roughly arranged parallel to the isotherms that prevailed during the final stages of rapid solidification [33, 32]. Remarkably, the rapid lateral growth of the grain marked by the labels 3 and 4 in Fig. 4.32c occludes ten to eleven columnar grains to its right and its growth by the new mode consumes close to 40% of the entire melt remaining at the time of the growth mode transition from that associated with formation of Zone 3 to that of Zone 4 during the RS process of the alloy. The new growth mode responsible for establishing Zone 4 consumes the last remaining liquid alloy and concludes the solidification. The post-mortem bright-field TEM image collage in Fig. 4.32d shows the melt-pool dimensions of an ex-situ irradiated hypoeutectic Al-08 at. %Cu alloy

thin film. In the ex-situ PL irradiation experiments the imposed photon field distribution creates a melt-pool of elliptical shape where the dimensions of the minor and major vertices, r_1 to r_2 , of the melt-pool are in a ratio of about 1 : 10. The strongly asymmetric and elongated melt-pool shape is achieved by defining the beam profile via use of a nominally rectangular aperture and its demagnification via an optical laser projection system. As a result the photon distribution leading to the melting and subsequent solidification is to reasonable approximation a top-hat profile with steep Gaussian side-walls [46]. Although differences in the laser projection system and resulting melt pool shape exists the microstructural features observed are quantitatively equivalent to those established in the in-situ PL irradiated specimens. Morphological zones identical to the four zones observed in-situ experimentation also present in the ex-situ PL irradiation experiments for the hypoeutectic composition Al-Cu alloy thin films, e.g. compare Zone 1-4 in Fig. 4.32a and in Fig. 4.32d for Al-08 at. %Cu and Fig. 4.32c, Fig. 4.32d and Fig. 4.32e for Al-04 at. %Cu. Fig. 4.32e shows an ADF STEM image from the vertex region of the exsitu irradiated melt-pool revealing clearly the four morphologically distinct micro-structural zones. Despite these qualitative similarities and the comparable radii of curvature that can be used to describe the areas of the vertex regions of the ex-situ PL induced melt-pools and for the in-situ PL induced melt-pools, noticeable quantitative microstructural differences exist. For instance, Zone 3 in Fig. 4.32e extends only over about 0.5 μm , while it is much larger in Fig. 4.32a. This may be related to the combined effects for the differences in the alloy composition, the Cu content, and the PL pulse profile. The microstructures displayed in Fig. 4.33 show the extend of the HAZs (Zone 1) for the different photon distribution fields associated with the PL pulse profiles utilized in the ex-situ (Fig. 4.33a) and in-situ (Fig. 4.33b) PL irradiation experiments for hypoeutectic Al-Cu alloy thin films. At first glance, the top-hat laser profile used in the exsitu experimentation (Fig. 4.33a) clearly results in reduced grain size scale in the morphologically equiaxed polycrystalline region of Zone 1 as compared to the case of the in-situ PL irradiation (Fig. 4.33b). To quantify the width of the HAZ established at the perimeter of the PL irradiation induced melt pools, the changes in grain-size or average grain width have been determined as a function of the distance from the melt-pool edge. The area segments used to measure grains sizes as function of distance for the melt-pool edge are

marked on the micrographs of Fig. 4.33a and 4.33b respectively, The grain size distributions corresponding to the various segments of representative areas at increasing distances from the melt-pool edge have been collated in Fig. 4.34a and 4.34a for the ex-situ and the in-situ PL irradiated hypo-eutectic Al-Cu alloy samples respectively. Within the bounds of certainty of the data sets the grain size populations show mono-modal size distributions with well defined averages for both samples. Plots of grain size versus distance from the melt pool edge obtained for the data sets shown in Fig. 4.34 are included as in-sets in Fig. 4.33. The vertical black dashed lines in Fig. 4.33a and in Fig. 4.33b are associated with a transition in crystal growth mode, marking the boundary between Zone 3 of columnar grain growth to the left and Zone 2 of transition from occlusion to columnar growth on the right. To the left of the black dashed lines the growing grains of Al advancing in the STEM micrographs from the left along the horizontal direction show first signs of forming Cu rich precipitates. The average grain width of the ribbon like shaped or columnar grains are displayed in the grain-size plots (insets in Fig. 4.33a, 4.33b) as white or open circle markers. Furthermore, the black line is associated with a flat solidification interface, a positive interface velocity $v > 0m/s$ and is assumed to be abrupt and well defined. The yellow dashed lines in Fig. 4.33a and 4.33b mark the approximate boundary between Zone 2, the transition zone, where occlusion processes take place by growth competition, and Zone 1 where partial melting and grain coarsening take place. The, boundary between Zone 1 and Zone 2 is assumed to be fairly rugged or diffuse on the scale of the local grain diameters. The exact location of this boundary depends on location along the melt-pool edge where the *mushy-zone* comprised of retained solid and liquid melt sustains prior to and in the very early stages of the onset of the solidification processes. This conclusion is drawn based on the observations in dynamic sequences during in-situ DTEM experiments and is analogous to the melting and solidification sequences elaborated for the Al thin films (e.g. Section 4.1.3). The average solid-liquid interface velocity along the yellow line is assumed to have been about $v \approx 0m/s$, i.e., a momentarily stationary interface is assumed. Along this somewhat diffuse interface marked by the vertical yellow dashed line the average grain-size widths are ≈ 150 nm for the ex-situ and ≈ 250 nm for the in-situ PL irradiation experiments of the hypo-eutectic Al-Cu alloys, as marked as the yellow dot/circle in the grain-size plots inset in Fig. 4.33a and Fig. 4.33b, respectively. The

average grain-sizes plotted in Fig. 4.33a for the ex-situ PL irradiated Al-Cu alloy have been obtained from the segmented unit areas at increasing distance from the flat melt-pool edges labeled a-j. At distances between 1.0 and 1.5 μm from the melt-pool edge the average grain-size plateaus at 115 nm. For distances of 1.5 μm and larger away from the melt-pool edge the average grain-size decreases monotonically, following a hyperbolic decay function. The bright contrast features in Fig. 4.33, an ADF STEM micrograph obtained from the co-vertex of the ex-situ irradiated melt-pool, are associated with an elevated amount of Cu, while dark features are associated with reduced Cu content, representing Al solid solution. Evidently, Cu enriched (relative to the Al solid solution grains and the alloy composition) phase is segregated around Al grains. Notably, with increasing distance from the melt-pool edge the connectivity and thickness or width of Cu enriched grain-boundary phase decrease until the microstructural morphology of the as-deposited state with separate nano-crystalline (average grain size ≈ 50 nm) Al solid solution and Cu-enriched (relative to the alloy composition) phase is reached at distances of ≈ 4.5 μm and larger (Fig. 4.33a). Figure 4.33b shows the heat-affected zone of an in-situ irradiated Al-04 at. %Cu alloy thin-film. Here, the grain-width along the black dashed and yellow dashed lines, marking the boundaries between Zones 3 to 2 and Zones 2 to 1, are ≈ 470 nm and ≈ 250 nm, respectively, as noted in the graph in Figure 4.33b. The average grain size determined for the segmented areas labeled as (a-n) has been used to obtain the plot of grain-size versus distance from the melt-pool edge plot shown as inset in Fig. 4.33b. After an initial decline from the large vertical grain width, ≈ 470 nm, along the black dashed line (onset of Zone 3 crystal growth) the average grain-size plateaus at distances between 1.5 μm and 2.5 μm away from the former melt-pool edge. At distances beyond the plateau the grain-size decreases following a shallow hyperbolic decay function reaching the as-deposited grain size scale of 50 μm average grain size at distances of ≈ 7.5 μm . The grain size changes determined from analysis of the micrographs of Fig. 4.33a and Fig. 4.33b show morphological scale differences due to the different laser profiles and resulting thermal gradients in the alloy thin films. The occlusion zone, Zone 2, defined by the dashed yellow and black lines, in the in-situ irradiated sample is about twice as wide as compared to the ex-situ irradiated melt-pool. The precipitate free grains in the occlusion zone grow into the direction of the center of the melt pool by on the order of

800 nm before first signs of Cu enriched phase precipitates. The grains in the occlusion zone of the ex-situ irradiated sample grow 400 nm into the melt pool before they show first signs of precipitates. The grain width along dashed black line also shows about a factor of two enlargement for the in-situ irradiated samples (≈ 470 nm) as compared to the ex-situ irradiated samples (≈ 260 nm). This overall coarsened microstructure in the ex-situ irradiated samples as compared to the ex-situ PL irradiated samples can be attributed to the different laser profiles and resulting thermal gradient. The experiments have been conducted to achieve full melting at the lowest possible laser fluency. The shallow Gaussian laser profile used in the in-situ PL irradiation experiments exposes the area surrounding the melt-pool to a significant amount of heating from the photon distribution field in the laser pulse, leading to slower dynamics in the development of the liquid-solid interface velocity due to a shallower and longer range thermal gradient. The solid alloy surrounding the melt-pool, i.e., the heat sink for the excess heat emitted from the super-heated melt-pool, is at elevated temperatures in the in-situ PL irradiated thin films relative to the case of the ex-situ experiments where the sharper laser profile also leads to sharper, steeper thermal spatial gradients. Furthermore, the distance from the hottest region of the melt-pool (center point) of the in-situ experimentation melt-pool shows a minimum distance of 20 μm , while the hottest line (central line) in the ex-situ setup is about 10 μm away from the heat sink of the solid alloy surroundings. The time of heat extraction is a function of melt-pool width since the heat extraction rate is limited by the thermal diffusion in the liquid. Thus the grains bounding the melt-pool edge experience an extended time to grow leading to a coarser microstructures for the case of the in-situ PL experiments due to longer solidification times. Moreover, it is assumed that the starting temperatures reached in the melt-pools are the same for the in-situ and the ex-situ laser irradiation and melting experiments. Given the differences in the laser power profiles across the beam diameter this may not be actually the case. Considering a shallow Gaussian versus a steep top-hat shaped power profile in the laser pulse, it is reasonable to expect considerable differences for the duration of the initial melting process and elimination of the two-phase, mixed liquid-solid or mushy zone prior to the onset of crystal growth and solidification. Such different pre-solidification delay times after the delivery of the initial laser pulse to melt the alloy thin films prior to the onset of solidification can suitably rationalize

the coarser scale of the microstructural zones 1 through 3 in the in-situ experiments relative to the ex-situ experiments of the PL induced melting of the hypo-eutectic alloy thin films , which otherwise exhibit qualitatively the same microstructural characteristics, e.g. Zone 1 to Zone 4 morphology (Fig. [4.33](#)).

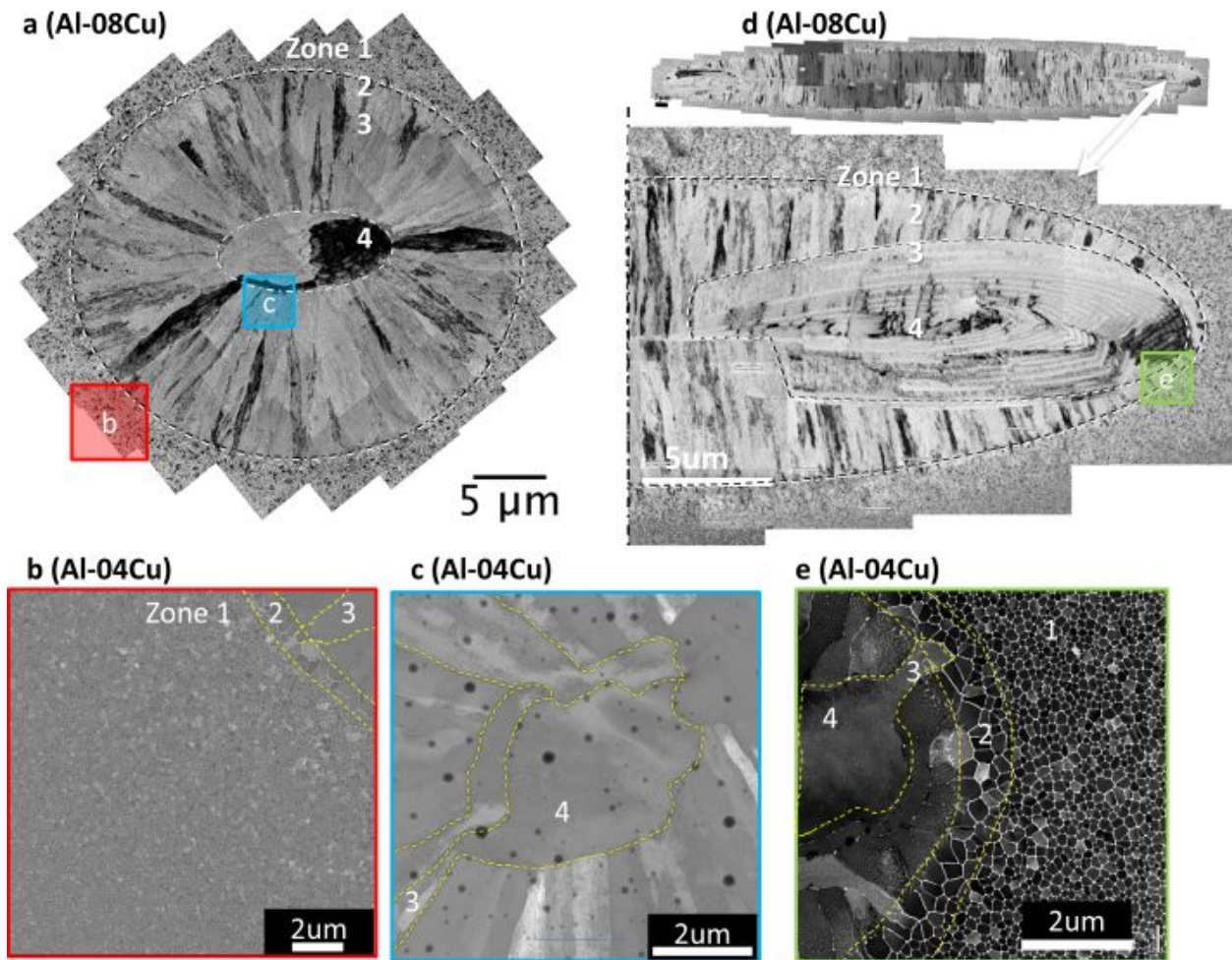


Figure 4.32: **a** In-situ irradiated melt-pool showing four morphological different zones. **b** shows the familiar 3 distinct zones found in RS experiment of pure Aluminum, (Zone 1 HAZ), (2 transition zone), and (3 growth zone). **c** the transition from zone 3 into zone 4 the banded region. **d** TEM collage showing the morphology of the ex-situ irradiated aluminum copper thin film and the distinct Zones (1-4) present **e** ADF-STEM image of the vertex of the ex-situ irradiated film. The in-situ and ex-situ experiment show essentially the same micro structural features and compare well with experiments done in continuous wave laser experiments, to note is that the co-vertex of the ex-situ melt pool is half the diameter of the in-situ experimentation

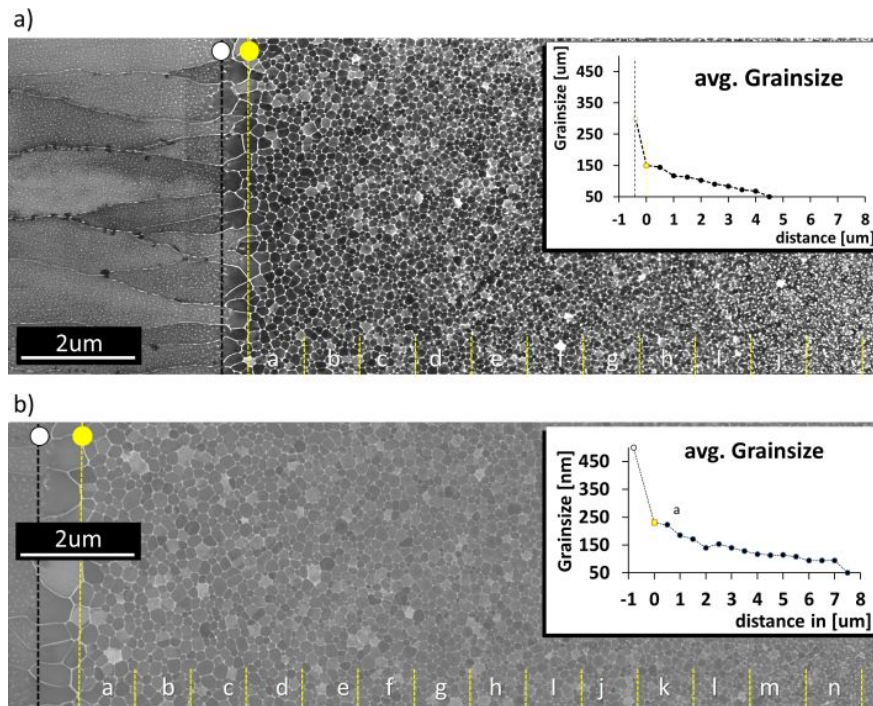


Figure 4.33: ADF TEM images of Zone 1-3 for **a** the exsitu irradiated film alongside with an evaluation of the heat effected zone showing the grain-size evolution as a function of distance to the former melt-pool edge, the grain size is unaffected at around 5 μm away from the melt pool edge and **b** shows the average grain size for the in-situ irradiated microstructure the grain size reaches starting condition at about 8 μm away from the melt pool edge. Further, indicated in the images are the segments taken into account for the grain size evaluation which are displayed in Fig. 4.34. To note is that the microstructure irradiated with the in-situ laser appears to be more affected, the largest grains found are around twice the dimensions, the HAZ is around twice as long and the width of the columnar grown grains at the point of first precipitation is twice as wide. This might be an effect of the different photon profile and/or different heat extraction times profiles

a Exsitu Statistics

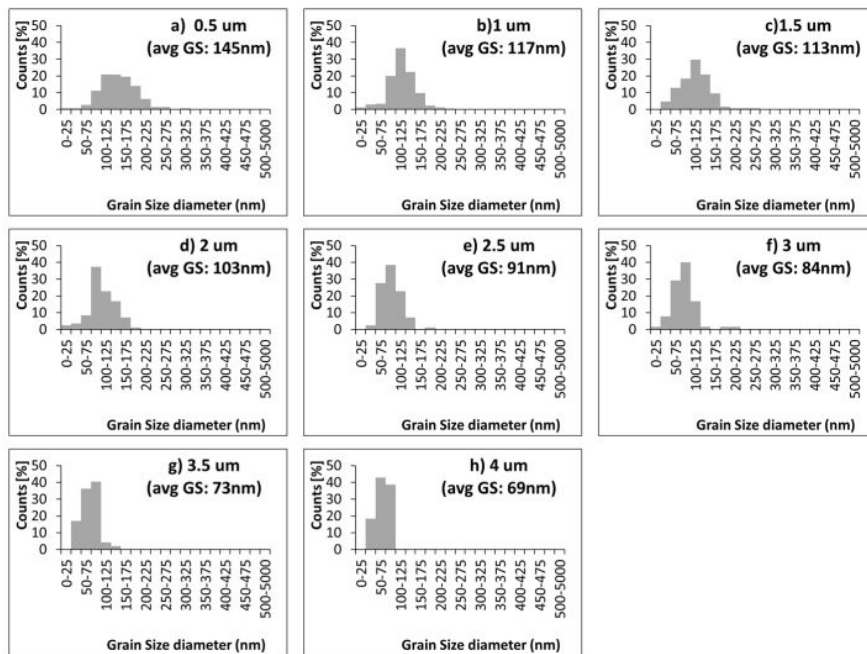


Figure 4.34: Statistics for individual evaluated segments of Figure 4.33

b In situ Statistics

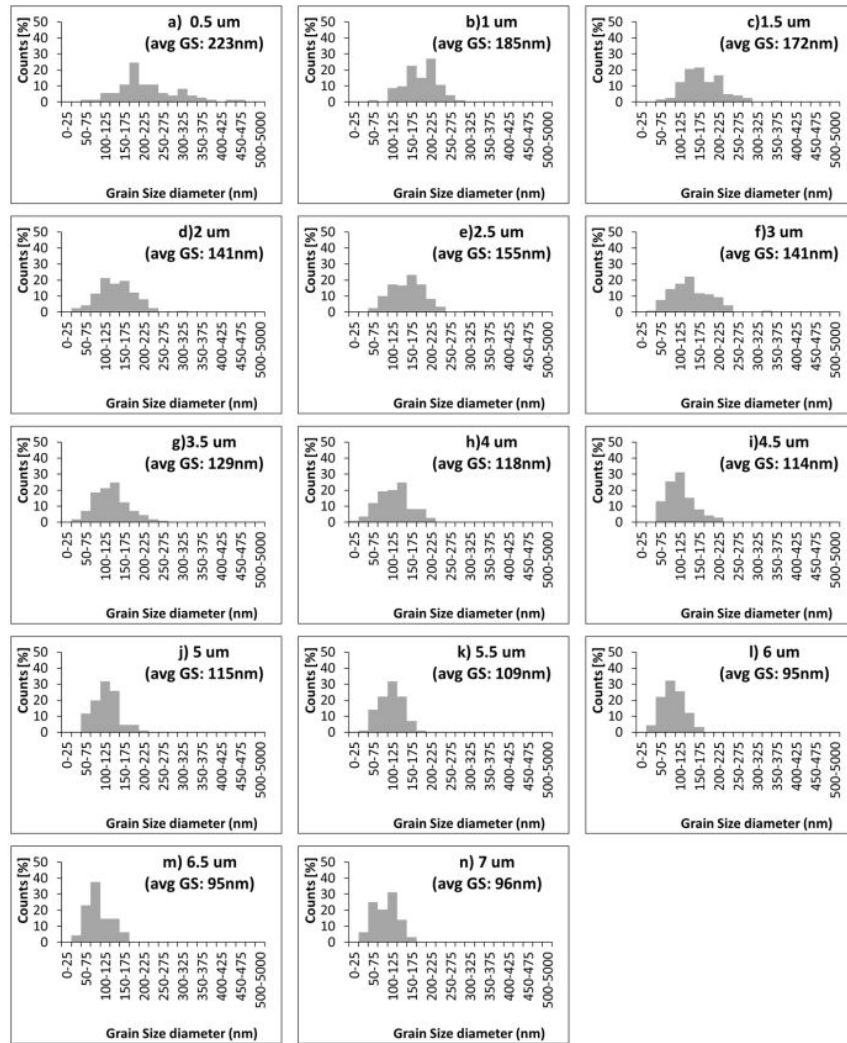
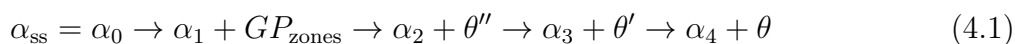


Figure 4.34: ... continued

4.2.3 PED Studies of the in-situ PL irradiated hypoeutectic Al-Cu Alloy

Aside from the stable phases of the α -Al matrix and θ - Al_2Cu precipitates, after non-equilibrium processing the hypo-eutectic composition binary Al-Cu alloys may also contain additional meta-stable intermediate phases, such as Guinier-Preston Zones (GPZ), θ'' - and θ' - Al_2Cu , well-documented precursors in the precipitation sequences of supersaturated Al-Cu solid solutions during low-temperature aging treatments [47]. After the PL irradiation induced melting the micro-structures of the Al-04 at. %Cu alloy thin film should develop various different precipitates, enriched in Cu relative to the alloy and α -Al solid solution in the morphologically different Zones 1 to Zone 4. Here, the TEM based PED OIM method has been used to examine the details of the micro-structures produced in the Al-04 at. %Cu alloy thin films in response to the PL irradiation induced melting. Figure 4.35 shows results of PED OIM examination for a HAZ section located about $(3.8 \pm 0.2) \mu\text{m}$ away from the melt-pool edge. At this location the alloy only undergoes solid state transformation processes. The as-deposited thin film micro-structure consists of a nano-crystalline (average grain size of $\approx 50 \text{ nm}$) mixture of predominantly α -Al (94%), a minority fraction of θ - Al_2Cu ($\approx 5.6\%$) and minimal θ' -phase ($\approx 0.4\%$) grains. Recalling that the α -Al phase grains with $\approx (1.5 \pm 0.6) \text{ at}\% \text{ Cu}$ are exhibiting solute supersaturation at temperatures below $\approx 460^\circ\text{C}$, a typical precipitate age-hardening sequence in response to the thermal activation provided by the PL irradiation can be envisaged, as described in Eq. (4.1).



The α -Al phase solid solution, α_{ss} decomposes into the Cu leaner versions of α -Al phase, in descending Cu% from α_0 to α_4 , while in subsequent or partially overlapping stages the Cu enriched precipitates form in sequence as GPZ, θ'' - and θ' - Al_2Cu before finally the equilibrium phase θ - Al_2Cu is established. The IPF based PED OIM data in Figure 4.35a displays the film-normal directions of for the α -, θ - and θ' -phase grains that constitute the microstructure of the as-deposited alloy thin film. Clearly, the microstructure consists mainly of α -Al grains. The film normal pole directions of the individual granular features are color-coded according to the unit stereographic triangles inset in Figure 4.35a for each of

the three phases. The $\langle 110 \rangle$ -fiber film normal texture established after film deposition (e.g. Fig. 3) prevails for the coarsened α -Al grains. Quantitative analysis of the pole-density (see Fig. 4.36) and the grain size (Fig. 4.35c, 4.35d) indicates a very slight strengthening of the $\langle 110 \rangle$ -fiber texture and a significant increase in the average grain size from ≈ 50 nm in the as-deposited state to ≈ 126 nm after PL irradiation (e.g. Fig. 4.35d). Phase mapping reveals the spatial distribution, shape and scale characteristics and the phase fractions present after PL irradiation. The Phase map of Figure 4.35b indicates thickening of the Cu enriched phases located intergranularly with respect to the equiaxial coarsened Al matrix grains. Furthermore, the PL irradiation resulted in an increase in the volume fractions of the α - and remarkably, the θ' -phase, from 94% to 96.3% and from 0.4% to 1.2%, respectively, while the fraction of θ -phase decreased from 5.6% to 2.5%. The polycrystalline thin film retained a grain boundary network (GBN) dominated by high-angle grain boundaries. GB sections with disorientation of $>15^\circ$ account for 92.3% of the length of grain boundary analyzed, while the remaining minority fraction contains 6.2% of segments in the transitional disorientation range of 5° to 15° and only 1.5% in the low angle range with disorientation 5° (Fig. 4.35c). Figure 4.36 collates IPF based PED-OIM maps for the α -Al and θ' -phase grains. Fig. 4.36a shows the OIM map for the film normal direction (z-direction) and the associated pole figures for α -Al and θ' -phase in Fig. 4.36b and Fig. 4.36c, respectively. The α -Al grains exhibit a $\langle 110 \rangle$ -fiber texture with respect to the film normal, very slightly increased in strength due to PL irradiation effects (≈ 4.1 versus ≈ 3.2 times average after and prior to PL irradiation, respectively). The indexed θ' -phase does not show a preferred orientation with respect to the film normal in this region of the alloy thin film microstructure. The thermal gradient in this region is assumed to decrease along the x-direction as marked for reference in Fig. 4.36a. In order to ascertain possible texture effects of the heat extraction direction on the α -Al grains and θ' -phase the PED OIM data set has been rotated to display the poles parallel to the x-direction in Fig. 4.36d and Fig. 4.36e. Neither the texture of Al- nor that of the θ' -phase shows discernible signs of an influence of the directional and non-isothermal heat treatment this region of the alloy thin film experienced due to the PL irradiation. For reasons of completeness, the PED-OIM images and pole-figures for the direction along the y-direction (orthogonal to heat extraction direction, \approx parallel to isotherms) are shown in Fig. 4.36g,

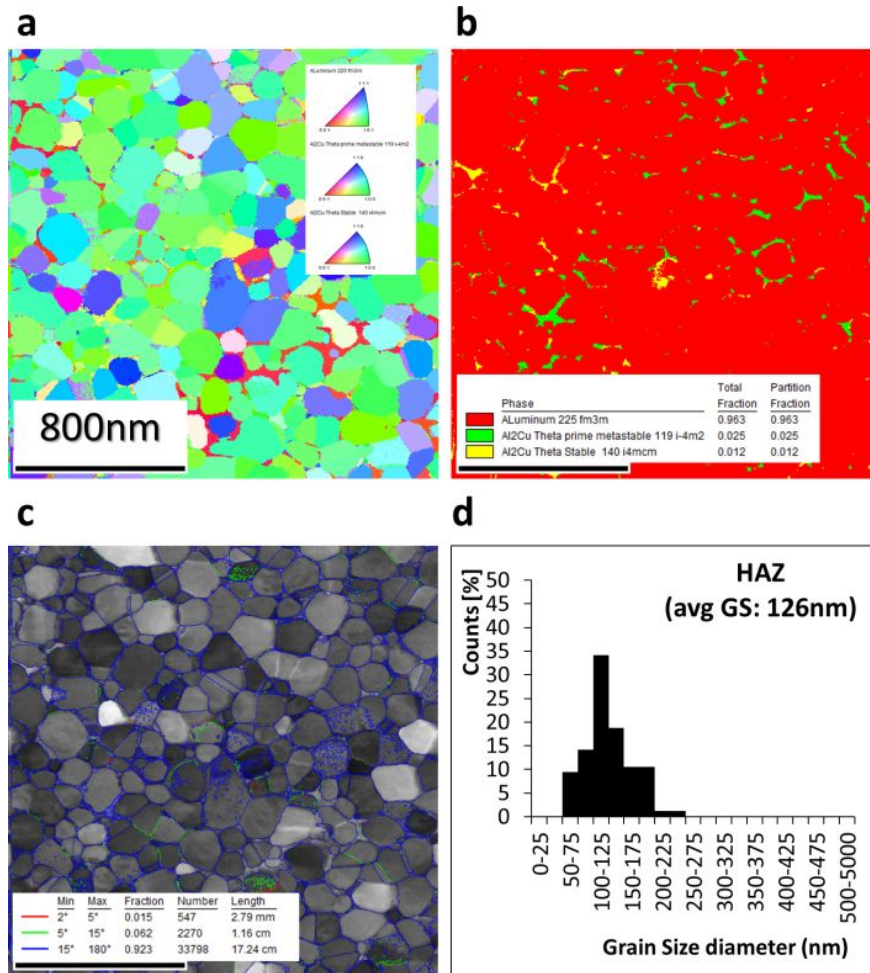


Figure 4.35: PED results of an area around 1 μm away from the former meltpool edge **a** shows the orientation map and **b** the associated phase map with around 2.5% θ' -phase and around 1.2% θ -phase **c** the vBF and the grain-boundary map showing the majority of the grains are separated by high angle grain-boundaries, and **d** grain size measured from the vBF. To note is that it was assumed to this point that only solid phase transformation have occurred in this region of the modified microstructure, however the presence of the θ' -phase suggests that a l-s transformation must have occurred.

Fig. 4.36h and Fig. 4.36i. During the strongly directional crystal growth process anti-parallel to the heat extraction direction, which is associated with formation of the microstructural constituents observed in the Zone 3, the growth zone, after PL irradiation of the hypoeutectic Al-Cu, the majority phase (α -Al) grains grow mostly radially towards the center of the melt pool, while more or less maintain their width established at the transition from Zone 2, the occlusion zone. This would be expected for a fairly planar growth front or interface morphology behind which the elongated shape columnar grains are established by its motion into the liquid. The PED-OIM data of Fig. 4.37a was acquired from a region at the onset of Zone 3, with the adjacent Zone 2 region just outside the field of view to the top of the figure. For the growth mode transition associated with the onset of Zone 3 crystal growth, producing columnar grains via a eutectic solidification process under rapid solidification conditions, a transformation or crystal growth interface velocity of $1\text{-}1.5\text{ms}^{-1}$ can be reasonably assumed. In the field of view of Fig. 4.37a multiple grains with different crystal growth directions were analyzed by PED-OIM. While all grains in this microstructural zone exhibit a matrix of α -Al containing Cu-enriched phase precipitates (e.g. Fig. 4.32-Fig. 4.34), here only for the grain with $\langle 110 \rangle$ as the film normal (FN = z-direction, green color) consistently and reliably indexed second phase precipitates, θ' -phase, can be discerned by the PED analysis. The absence of second phase indexed region in the PED scan of the grains with $\langle 111 \rangle$ film normal orientation might be due to reflections corresponding to the second phase being either too weak relative to the matrix reflections or because a particular orientation relationship between the matrix and precipitates exists that superimposes the second phase reflections with the dominant parent phase reflections. Either of which would rendering successful phase identification by automated indexing of the PED data difficult or impossible. Figure 4.37b shows the phase map for the θ' -phase precipitates superimposed with the virtual bright-field image, identifying coarser inter-granular and finer scale intragranular precipitates in the $\langle 110 \rangle$ -film normal α -Al grain. Figure 4.37c shows the PED-OIM orientation map with respect to the film normal direction (FN = z-direction) for the latter α -Al grain. The associated pole figures, Fig. 4.37d, reveal that grain has the $\langle 110 \rangle$ direction parallel to the film normal and the $\langle 111 \rangle$ is closely aligned to the crystal growth direction parallel to the solidification direction and anti-parallel to the dominant directional heat flow (here the

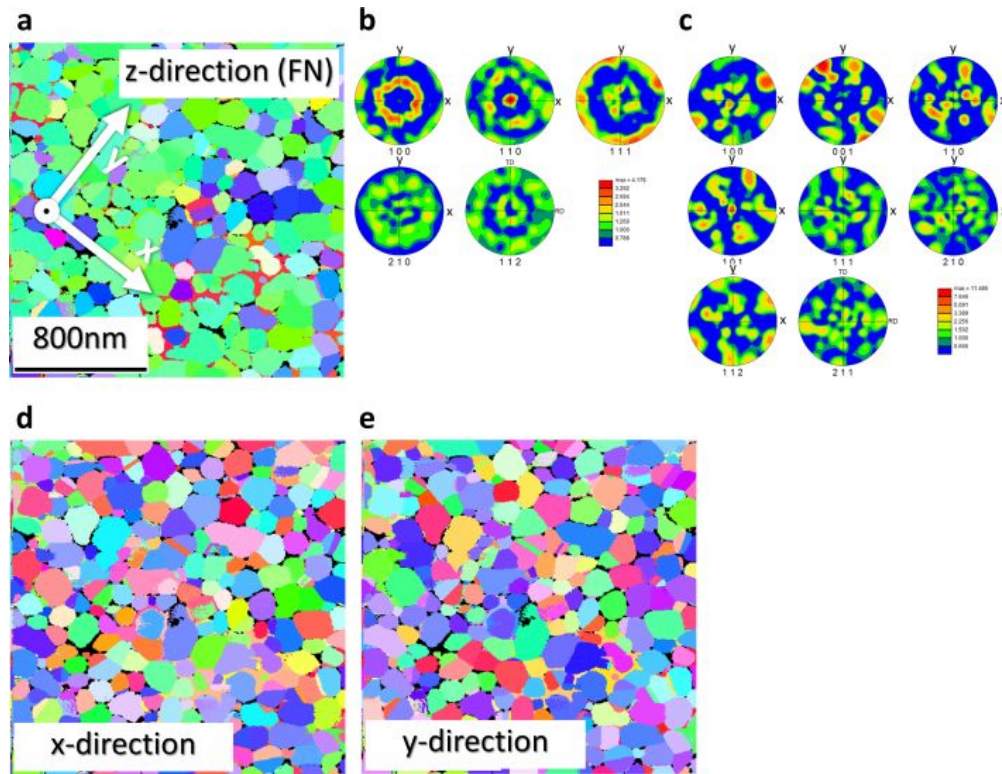


Figure 4.36: PED-OIM of the HAZ at a distance of about $120\ \mu\text{m}$ away from the melt pool edge. **a** IPF-based orientation map of the film normal for the equiaxed coarsened $\alpha\text{-Al}$ grains. **b** associated pole figures for the $\alpha\text{-Al}$ and in **c** the intergranularly distributed (see black regions in panel **a**) θ' -phase; **d** IPF-based orientation map for the crystal orientation parallel to direction x marked in panel **a**; **e** IPF-based orientation map for the crystal orientation parallel to direction y marked in panel **a**.

x-direction marked in Fig. 4.37c). The pole figures and IPF based PED OIM orientation map of Fig. 4.37f shows the crystal growth direction for the α -Al matrix in this grain. The pole figures for the θ' -phase with respect to the film normal and the Al crystal growth or solidification direction are shown in Fig. 4.37e and Fig. 4.37h, while Fig. 4.37k shows the complementary in-plane pole orientations along the approximate isotherms (the direction orthogonal to both the film normal and the growth direction). Comparing the pole figure signatures for the matrix and precipitate phases in these complementing orientations allows assessment of possible orientation relationships. Considering the $\langle 110 \rangle$ Al pole figure for the plane normal (Fig. 4.37e) coincidence with a significant fraction of $\langle 101 \rangle$ pole density in the tetragonal θ' -phase (Fig. 4.37f) is observed. This indicates that a significant subset of the θ' -phase $\langle 101 \rangle$ poles is parallel to the matrix α -Al $\langle 110 \rangle$ pole. Further analysis shows that the θ' -phase $\langle 112 \rangle$ poles are approximately parallel to the Al $\langle 111 \rangle$, which are oriented close to parallel to the solidification direction. The IPF based PED OIM data sets rotated to display the crystal orientations parallel to the isotherms (y-direction, orthogonal to both the film normal and the solidification direction), e.g. see Fig. 4.37i, Fig. 4.37j and Fig. 4.37k reveals that a minority fraction of the θ' -phase $\langle 100 \rangle$ poles are aligned parallel to $\langle 100 \rangle$ poles of the Al matrix grain. This would be expected after the favorable precipitate and matrix orientation relationship described by Guinier-Preston. However, a large fraction of the indexed θ' -phase precipitates can be identified with approximate alignment of their $\langle 112 \rangle$ poles parallel to the Al matrix $\langle 100 \rangle$ poles. It therefore appears reasonable conclude that the θ' -phase precipitate population comprises of different subsets or orientation variants, which exhibit different orientations with respect to the Al matrix grains they are embedded in. The orientation relationships between matrix and precipitate phase differ from those described in commonly to obtain during the age hardening processes in Al-Cu base alloys. The latter are strongly influenced by the effects of inter-facial strain accommodation resulting from lattice misfit between matrix and precipitate during these solid-state transformations. Notably, in liquid-solid transformation the constraints imposed on solid state transformations products from the required strain accommodation across the interphase interfaces are less important to the resulting possible orientations in resulting phase mixtures. The PED-OIM scan shown in Fig. 4.38a displays the plane normal orientations in grains of Zone 3 and has been obtained

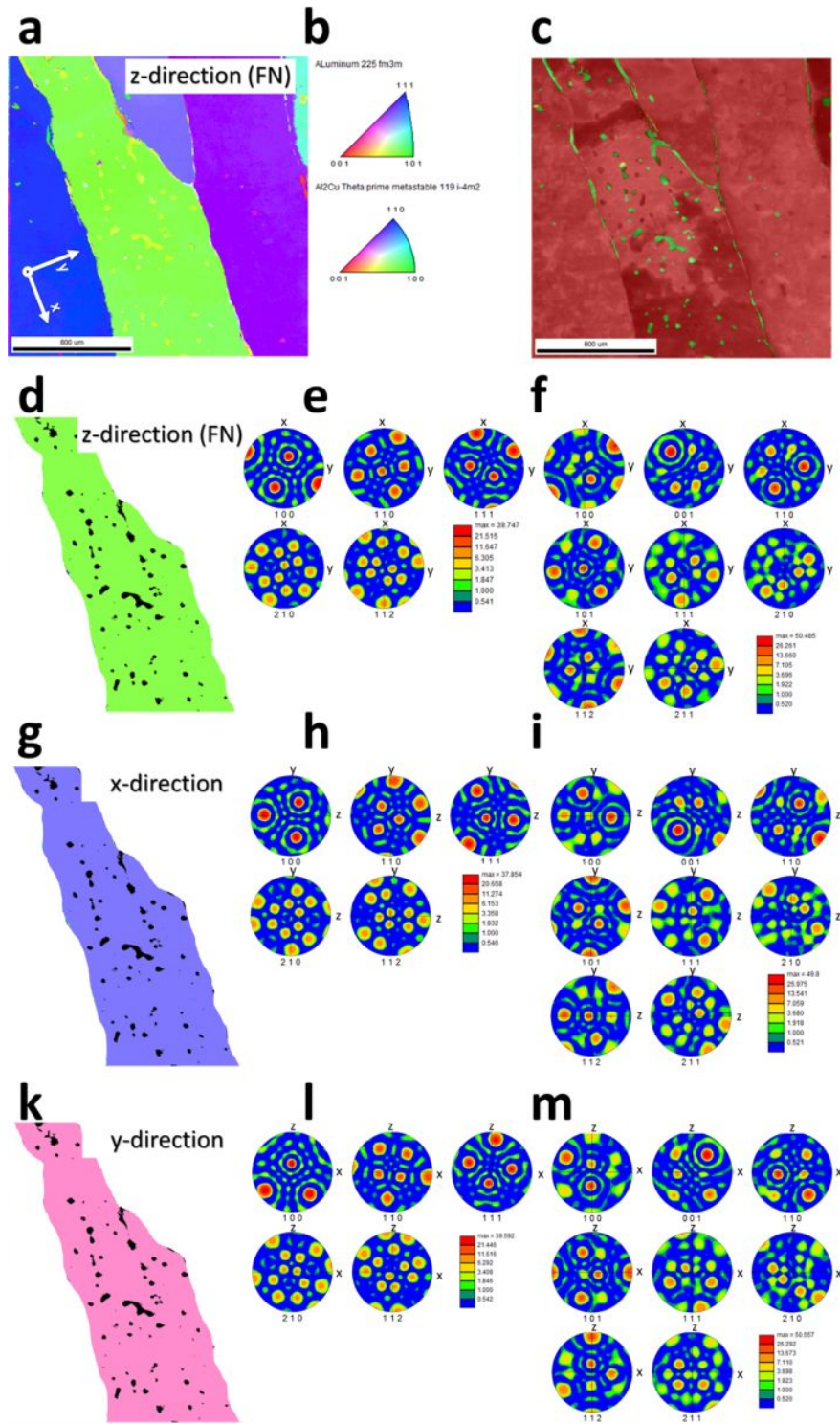


Figure 4.37: **a** PED-OIM image of columnar grown grains, with associated phase map **b**, here, the $\{110\}$ grain (green) shows precipitates that can be indexed utilizing the automated method. The $\{110\}$ grain is analyzed separately for **c** the Film-normal, **f** the solidification direction and **i** perpendicular to SD.

from a location near the edge of the melt pool of the rapidly solidifying Al-04 at. %Cu alloy. Two smaller Al matrix grains of different orientations were occluded by the larger columnar morphology grains on the left and right side of the field of view. The latter exhibit $\langle 110 \rangle$ foil normal orientations. The grains predominantly grew directionally approximately along directions about -12° (clockwise rotation) rotated with respect to the y-direction denoted as an inset in Fig. 4.38a and the corresponding pole figure of Fig. 4.38c. The two columnar grown grains show that the $\langle 110 \rangle$ are parallel to the film-normal and the disorientation is 46.24° around $\langle 1.699, 1, 1.497 \rangle$ which is about 3° away from $\langle 323 \rangle$. Each of these Al matrix grains contains about 50 precipitates indexed with best certainty as θ' -phase as shown in the phase map of Fig. 4.38b. In order to establish orientation relationships from the present PED-OIM data shown in Fig. 4.38 the contributions from the two grains containing second-phase precipitates have been separated and are displayed in Fig. 4.39 and Fig. 4.40 respectively. Fig. 4.39a shows the PED OIM IPF based orientation map for the left grain only. The associated pole-figures for the matrix and the indexed precipitates are shown in Fig. 4.39b and Fig. 4.39c. Here the parent grain $\langle 100 \rangle$ direction is closely aligned with the solidification direction. The $\langle 100 \rangle$ direction in an FCC-metal is a preferred growth direction under dendritic growth conditions [48, 44]. In the region of the solidification microstructure of the Al-04 at. %Cu alloy examined here the growth interface is assumed to be a planar or flat interface where two phases crystallize simultaneously. The α -phase and θ' -phase grow predominantly anti-parallel to the heat-extraction direction under rapid solidification conditions far from equilibrium during rapid solidification establishing a kinetically modified eutectic micro-constituent. The IPF-based orientation maps of the solidification direction (Fig. 4.39e and Fig. 4.39f) show that a large subset of θ' -phase precipitates exhibit three different orientation relationships with the α -phase, which can be described by the parallel pole direction alignments as follows:

- $\{001\}_{\theta'} \parallel \{110\}_{\alpha}$ and $\langle 110 \rangle_{\theta'} \parallel \langle 100 \rangle_{\alpha}$
- $\{001\}_{\theta'} \parallel \{100\}_{\alpha}$ and $\langle 100 \rangle_{\theta'} \parallel \langle 100 \rangle_{\alpha}$

Moreover, clearly some of the precipitates show no preferred orientation to the parent α -phase. Finally, alignments of poles in the matrix and precipitate phases with respect to the

direction perpendicular to the solidification and film normal directions (e.g. Fig. 4.39g), indicate (e.g. Fig. 4.39h and Fig. 4.39i) that some precipitates exhibit alignment of their $\langle 100 \rangle_{\theta'}$ directions with a $\langle 100 \rangle_{\alpha}$ direction of the Al matrix.

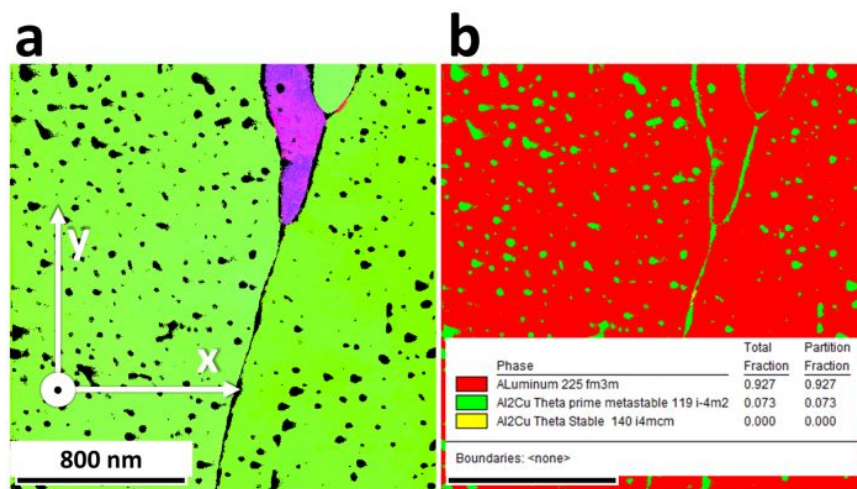


Figure 4.38: **a** Film Normal direction with around 50-100 precipitates indexed per grain, **b** phase map indicating the parent columnar grown α -grains (red) and embedded Θ' -phase (green)

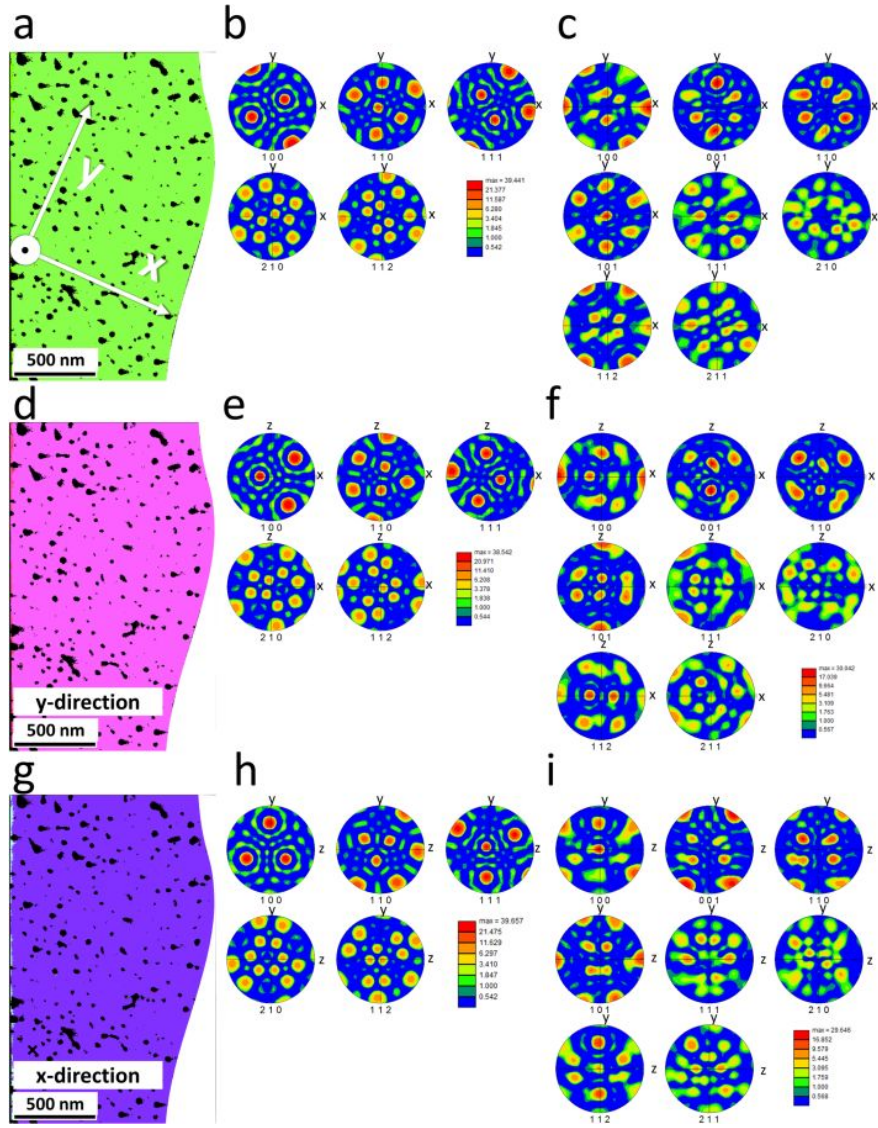


Figure 4.39: PED image of the Left Grain: **a** Film normal- **d** Solidification- and **g** Perpendicular Direction and associated (**b,e,h**) for the α -phase and (**c,f,i**) for the θ' -phase pole figures. Here the $\langle 100 \rangle_{\alpha}$ is closely aligned with the solidification direction for the second phase and a significant subset of the $\{100\}_{\theta'}$ and $\{112\}_{\theta'}$ planes are stacked parallel to $\{100\}_{\alpha}$

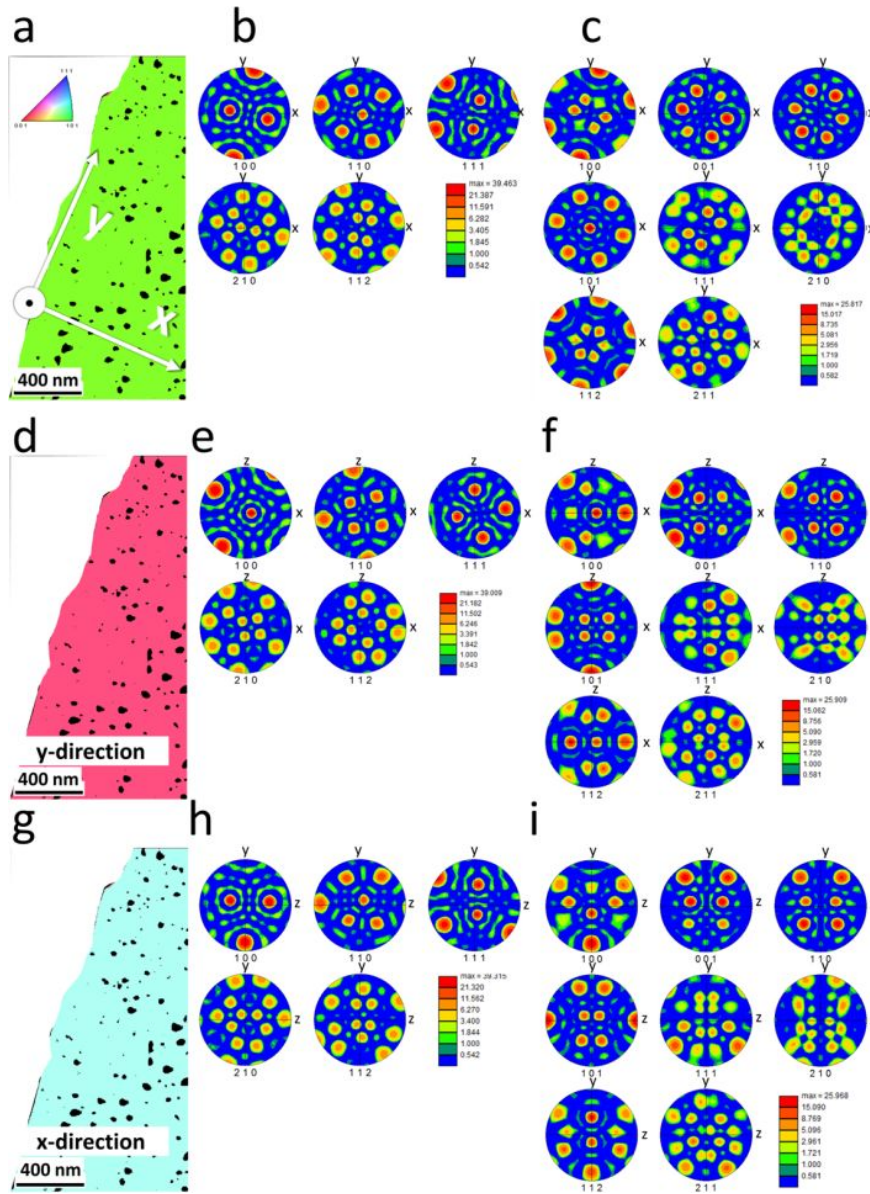


Figure 4.40: PED image of the Right Grain: **a** Film normal **d** Solidification direction and **g** Perpendicular Direction and associated **(b,e,h)** α -phase and **(c,f,i)** θ' -phase pole figures

4.2.4 Composition Analysis of the Growth Mode Transition Zone

During alloy solidification compositional adjustments at the interface accompanying the phase transformation determine the resultant microstructural features, the micro-constituents. These compositional adjustments depend on the interface behavior and characteristics, i.e., temperature, velocity, and morphology. During the early stages of solidification relatively low interface velocities attain and atomistic arrangements near the interface would reasonably be expected to experience near-equilibrium considerations. Elemental composition analysis by x-ray energy dispersive spectroscopy (EDS) can give valid information on the constitutional adjustments at the interface that are recorded in the resultant solid formed.

Figure 4.41a shows the results of STEM ADF imaging in combination with compositional EDS mapping for the growth mode transition from Zone 1 to Zone 2 (approximately from a stationary interface to a moving interface) and from Zone 2 to Zone 3 (pro-eutectic constituent formation to kinetically modified α -cells, modified eutectic constituent). This represents the regions of transformation mode changes from the final stage of melting to solidification of crystal growth and from near-equilibrium condition crystal growth to rapid solidification related crystal growth. The heat map in Fig. 4.41b represents the EDS quantification and shows the distribution of Cu in this region. The Cu based heat map displays a composition range from black 0 at.% to 33 at.%Cu. The majority of copper is located in grain boundary regions in Zone 1 and in the ellipsoidal precipitates found in Zone 3. The average area composition from regions of interest, (white circles in Fig. 4.41b), are shown in Fig. 4.41c. The equiaxed shape grains near the former melt pool edge show an average copper content of about 1.56 at.%, which under equilibrium considerations equates to a pro eutectic α -Al solid solution crystallizing at the solidus temperature of 630 °C. Notably, the field of view exhibits an average composition of 4.1 at.% Cu, the alloy composition. The line profiles (5)-(7) of the first regions of solidification (transition zone, Zone 2) show an increase of Cu concentration the precipitate free α solid solution grains along the dominant crystal growth direction. The solute content raises from about 1.2 at.% to about 3.3 at.% over the distance of about 0.5 μm . Under equilibrium consideration the maximum solubility for Cu in Al is about $c_{ms} \approx 2.5$ at.% at $T_e \approx 548$ °C (black dashed line Fig. 4.41d). Hence, after ≈ 250 nm of

crystal growth in this regime, the atom redistribution at the transformation interface clearly deviates significantly from prediction based on the equilibrium phase diagram. Considerably supersaturated Al solid solution, a metastable phase, has formed. When the interface temperature decreases to 548 °C or below, eutectic micro-constituent would be predicted to form, which is assumed to happen when the first precipitates of Cu enriched Al_2Cu related phase form the growing crystal (black line Fig. 4.41d). This is associated with a growth mode change from pro-eutectic forming to eutectic forming solidification. The average composition in Zone 3 of the matrix is about 3.1 at.% Cu and the average composition of the precipitate phase containing regions of the thin film is significantly elevated to ≈ 15 at.% Cu. The latter corresponds to a composition close to the eutectic point. Hence, the solid formed in Zone 3, direction growth zone, is termed as kinetically modified eutectic or α -cell.

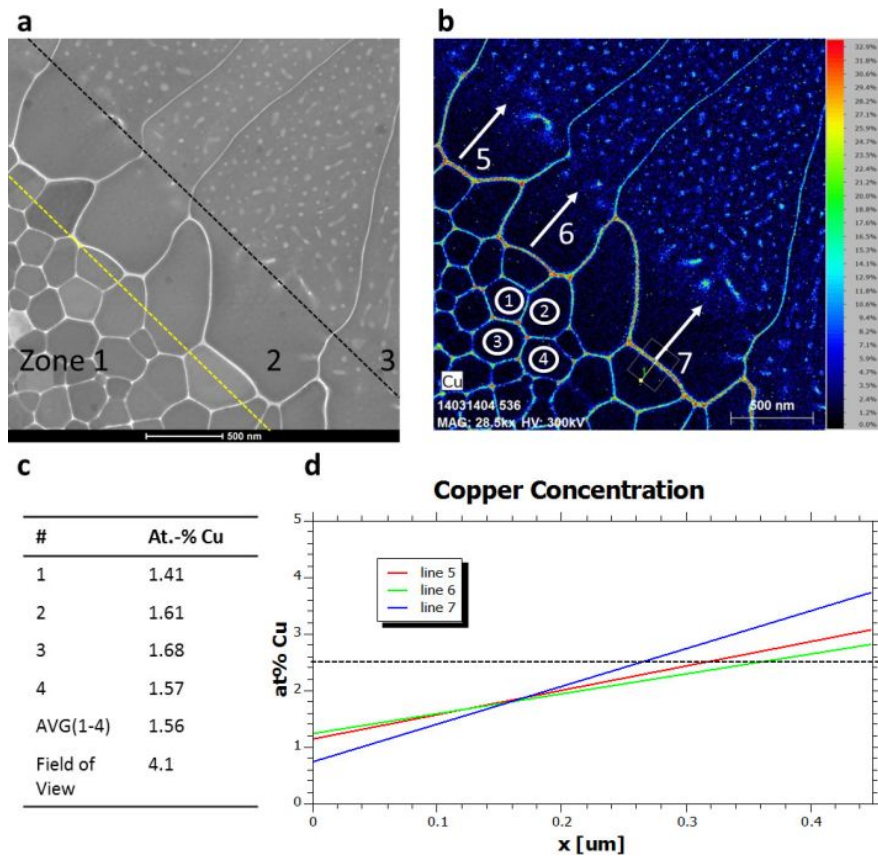


Figure 4.41: EDS of the transition zone **a** DF STEM image **b** Temperature Map **c** average grain interior composition **d** line profiles of columnar growing grains in the early stages of solidification

4.2.5 In-situ DTEM PL Irradiation of hypoeutectic Al-Cu Alloy

In the single component metal system the PL irradiation induced transformation sequences are influenced predominantly only by thermal effects, the evolution of the temperature field, while constitutional effects, changes in composition which are expected in a two-component alloy system, were negligible. For the single component Al metal system the details of the crystal growth morphology have been shown to depend critically on the transformation rates facilitated by the changes in the liquid-solid interface velocity (Section 4.1.3.4) In the hypo-eutectic Al-Cu alloys studied here the transformation sequences and related phase transformation mechanisms are reasonably expected to be influenced by both the evolution of the temperature and the composition fields, i.e., thermal and constitutional effects. Comparisons to the Al metal DTEM experiments provided benchmarks regarding selection of the parameters that define the spatio-temporal resolution of Movie-Mode (MM) series data explored for probing of the irreversible transformation events for the Al-Cu alloy. In the in-situ DTEM experiments a wide range of experimental parameter combinations, related to selection of a combinations of spatial domain resolution and temporal domain resolution, are available. The field of view in an observation is limited ultimately to the size the CCD camera and the resolution depends on the magnification chosen for the electron-optical system of the TEM. The size of the field of view and resulting spatial resolution are chosen to represent a best compromise to provide the information that is most relevant to the problem under investigation. Thus, to observe the entire melt pool a large field of view is required, implying TEM operation at relatively low magnification and therefore affording relatively low spatial resolution. Similarly, in the time or temporal domain, best compromise regarding combination of temporal resolution, essentially the time between individual Movie-Mode series frames (frame exposure plus the inter-frame delay time), and the temporal length or duration of the Movie-Mode series need to be made for any given problem under investigation. The in-situ PL irradiation DTEM experimentation performed for the Al metal (Section 4.1.3) established benchmarks for these parameters and regarding spatio-temporal resolution. So-called low-magnification and higher magnification DTEM experimental parameter selections, have been identified. With the lower magnification observation parameter selection the entire

melt-pool and the entire set of processes during the sequence of melting and solidification can be observed in a single Movie-Mode series for Al (see. Section 4.1.3.4). Figure 4.42a presents MM bright field image series obtained with 50 ns exposure time per image frame and inter-frame delay time of 2500 ns = 2.5 ns. The resulting resulting in Movie-Mode image series spans a duration of 20.4 μ s in total duration. The melting and the subsequent rapid solidification processes for the hypo-eutectic Al-04 at. %Cu alloy for an 80 nm thick alloy thin film are captured in two separate 20.4 μ s duration MM BF image series (Fig. 4.42a and 4.42b), which were obtained from two different locations on the same thin film sample within the established safe zone for in-situ DTEM PL irradiation experiments at distances in excess of 75 m away from the thick Si substrate. In the safe zone on a given thin film specimen the PL induced transformation sequences were shown to be reproducible and can be considered identical. In Figure 4.42a at time zero (0 μ s) the solidification process initiating photon pulse from the sample-drive PL system and the first 50 ns duration electron pulse interact with the specimen simultaneously. At this point in time the 50 ns exposure multi-beam bright-field image does not show a sharp interface between liquid and solid. Hence, the initial alloy thin film melting and associated heating from the conversion of the pulsed (15 ns) photon field energy to heat in the thin film specimen appears to be in progress. In the images obtained for the time 0 μ s will be disregarded in the velocity calculation analyses performed in the following, because of the uncertainty regarding the location of phase boundary between liquid and solid state regions of the Al-Cu alloy. At 2.55 μ s after the sample drive laser interacted with the stable two-phase mixture of nano-crystalline Al-04 at. %Cu alloy a soft or diffuse transition from solid to liquid can be detected and the resulting the melt pool dimensions can be measured. However, this measurement is associated with a fairly large error bar as the edge detection based on the soft contrast transient from the darker liquid alloy region to the brighter solid alloy region. At about 5.1 μ s after melt initiation a well-defined and sharp solid-liquid interface is established in the third frame of the Movie-Mode image series. The subsequent images at longer times after the melt initiation capture the solidification process of the alloy with unprecedented spatio-temporal resolution and enable quantitative measurements of the solidification dynamics for the alloy from the direct in-situ DTEM observations. At about 7.65 μ s in the fourth image of the series distinct small (\approx 1-3 μ m) dark

features become first noticeable all along the perimeter at the edge of the melt-pool. These small and well-defined dark contrast features are associated with columnar grains oriented into strong a Bragg condition for the pulsed electron illumination wave field. Neighboring columnar grains that are not oriented into a strongly diffracting condition appear discernibly brighter, which gives rise to the distinct and strong variation associated with the columnar morphology and directionally crystallizing grains that establish the Zone 3 microstructure. The columnar grains consume the liquid by growing rapidly radially towards the center of the melt pool, anti-parallel to the heat extraction direction until the last image frame of the first MovieMode image series acquired at $20.4\ \mu\text{s}$ after melt initiation. Notably, the fact that these crystallographic contrast features, grains are discernible implies that they have coarsened massively relative to the $\approx 50\ \text{nm}$ grain size associated with the Al-Cu alloy thin film microstructure prior to PL irradiation (e.g. Figs. 4.32 to 4.34). In order to observe the solidification process until its completion, a second MM series experiment was required, which has been performed by selecting a delay time of $20\ \mu\text{s}$ after the initial melting for the start of acquisition of the nine-frames. This second MovieMode series data was obtained by repeating the PL irradiation under nominally identical conditions at a different location within the safe zone on the thin film, enabling capture of the later stages of the solidification experiment from $20\ \mu\text{s}$ onward, Fig. 4.42b. The first image at $20\ \mu\text{s}$ after melt initiation in Fig. 4.42b shows contrast features indicating that solidification has progressed such that a substantial amount of liquid has been consumed by the advancing solid in the form of the columnar grains. Subsequent images captured at longer times after melt initiation document the progression of the solid-liquid interface until solidification is completed at a time between the images recorded at $30.2\ \mu\text{s}$ and $32.75\ \mu\text{s}$ respectively. The type of experiments represented in Fig. 4.42a and Fig. 4.42b have been conducted twice to ensure reproducibility. The results of the melt pool area changes and solidification interface velocity analyses shown in Fig. 4.42c include all four MM BF image series data. The error-bars show the small deviations between the measurements resulting from each of the separate DTEM PL irradiation MM experiments. Fig. 4.42c displays the temporal evolution of the size of the alloy melt pool. Here the data points correspond the measured length of the major axis and minor axis radii of the elliptical shape melt pools and the equivalent radius for a circular shape of identical

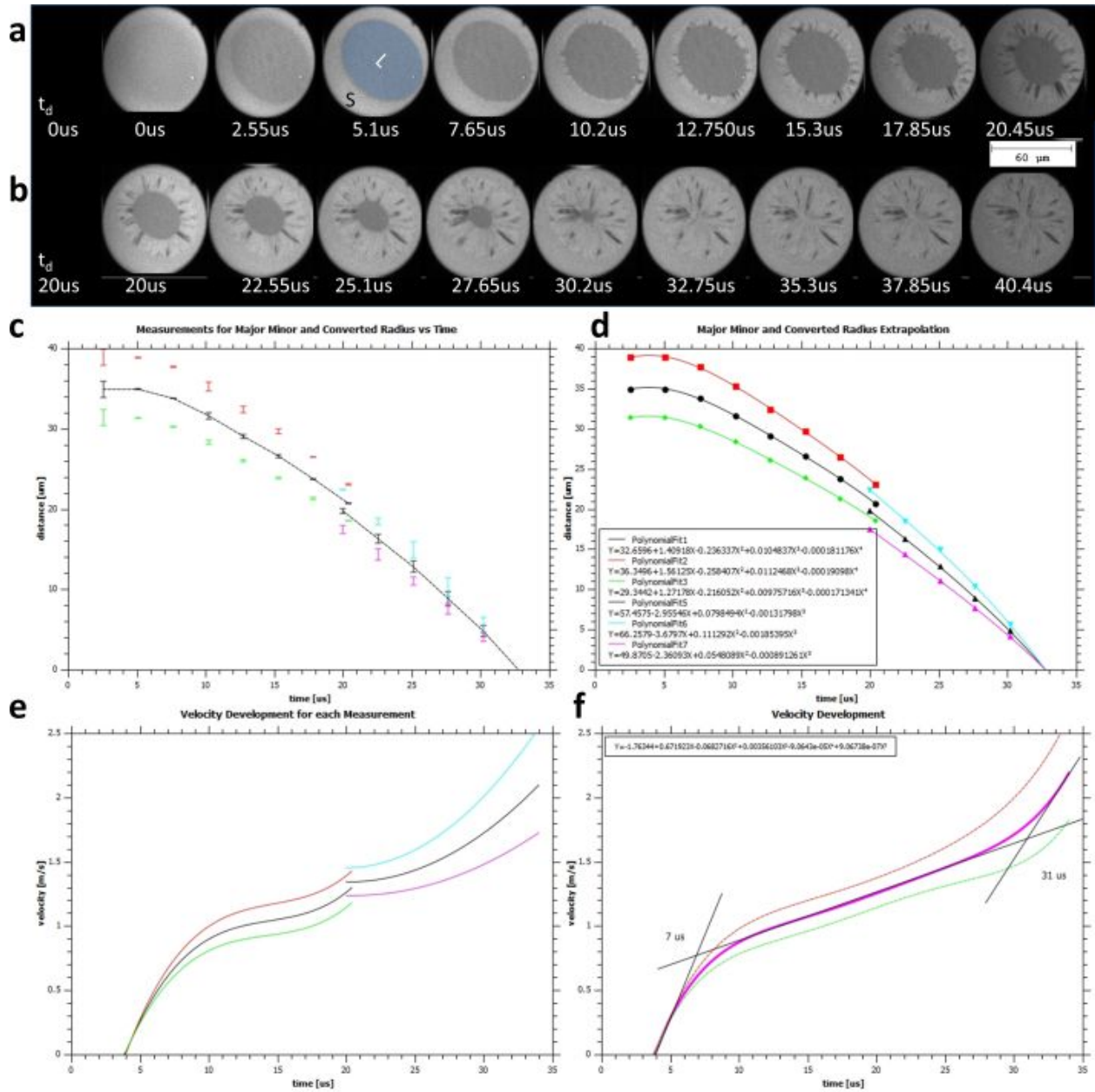


Figure 4.42: **a** Low-Spatio-temporal observation of solidifying Al-04 at %Cualloy capturing the complete solidification sequence. **b** showing the Radial change of the melt-pool (blue) and the resulting velocity plot (red)

area the elliptical shape alloy melt pools are shown by the dashed lines. The major and minor radii recordings are displayed as colored lines where the larger measurement corresponds to the major and the smaller measurement to the minor radius of the elliptical melt-pool. Fig. 4.42d shows the best-fit polynomial functions for the experimentally determined melt pool size measurements. The fitting utilized weighted measurements based on the error-bar of the experimental data. Differentiating the functions shown in Fig. 4.42d provides for determination of the velocity development for the solidification interface alloy for each of the separate DTEM experiments performed for the Al-Cu hypo-eutectic alloy. Furthermore, the individual velocity profiles were combined in Fig. 4.42f. From the continuous plot of velocity versus time after melt initiation the converted area radius (magenta) overall velocity profile for the alloy solidification process has been determined. Utilizing a simple tangent methods the critical times for distinct growth mode changes can be estimated from this temporally resolved interfacial velocity evolution profile. In the case for the Al-04 at. %Cu alloy a first growth mode change is detected at about $(7 \pm 1) \mu\text{s}$ and the second growth mode change at about $(31 \pm 2) \mu\text{s}$ after the melt initiation by PL irradiation of the thin film. The larger temporal error-bar in these analytically determined critical times for growth mode changes arises from the tangent fitting procedure. Notably, the onset of the alloy solidification sequence involves a significant time delay after the melt initiating PL irradiation at $0 \mu\text{s}$ of about $3.9 \mu\text{s}$ (intercept with the abscissa in Fig. 4.42f) and an initial very rapid acceleration stage until the first growth mode change occurs at about $7 \mu\text{s}$. The second growth mode is associated with a more moderate, constant acceleration of the transformation interface for a duration of about $24 \mu\text{s}$ until the second growth mode change at $31 \mu\text{s}$ result in further and steep acceleration for the final stage of crystal growth during the solidification of the hypo-eutectic alloy. The low-magnification spatio-temporal resolution DTEM experiments enabled determination of the time ranges for the constant acceleration related rapid solidification processes. The growth mode change associated with formation of the columnar morphology grains, labeled as Zone 3 in Fig. 4.32, has been determined to occur at about $7 \mu\text{s}$ after melt initiation. This mode of crystal growth changes again at about $31 \mu\text{s}$ after melt initiation and the transition from Zone 3 to the Zone 4 growth mode with the banded morphology grains (see. Fig. 4.32) occurs. Additional high resolution DTEM experiments have been performed

to observe the transformation interface behavior near these critical growth mode transition times, i.e., near $\approx 7 \mu\text{s}$ and $\approx 31 \mu\text{s}$ after melt initiation, for the Al-4at.%Cu alloy and are presented in Fig. 4.43. Compromising with a smaller field of view (reduced from $\approx 125 \mu\text{s}$ to $\approx 16 \mu\text{s}$ diagonal width) and shorter total durations (reduced from $20 \mu\text{s}$ to $3.3 \mu\text{s}$) afforded about one order of magnitude improved spatial and about five-fold improved temporal resolution with $550 \text{ ns} = 0.55 \mu\text{s}$ per frame in MovieMode series (Fig. 4.43a and Fig. 4.43a). The MovieMode series data shown in Fig. 4.43a captures details of the dynamic events of the irreversible solidification sequence at the onset of solidification, the first growth mode change at $\approx 7 \mu\text{s}$. The first image series frame of Fig. 4.43a at $5.55 \mu\text{s}$ after melt initiation shows that the region near the solid-liquid interface is composed of equiaxial shape grains of fine grain size scale on the order of a few hundred nanometers. The faint contrast from the inter-granular or inter-crystalline regions increases to become noticeably darker in the region marked by the red lines marks in Fig. 4.43a. The solid-liquid-interface is rough on the scale of the grain size with individual grains penetrating into the liquid. The solid-liquid interface temperature is assumed to be the temperature of the intersection between the overall composition and the liquidus line, here for the Al-4at.%Cu alloy this equates to about 650°C . For the hypo-eutectic Al-Cu alloy the α -phase with lowest possible Cu content composition can maintain stability at the corresponding solidus composition in equilibrium with liquid at 650°C . It is therefore reasonable to expect that crystalline phase observed in contact with the liquid represents Al solid solution grains. These grains would constitute the pre-existing solid or crystal from which growth directional y toward the center of the PL irradiation induced melt pool originates at the beginning of the columnar grain growth in Zone 3 of the solidification microstructure (e.g. Fig. 4.32). So, without the requirement for nucleation the directional crystal growth anti-parallel to the prevailing long-range thermal spatial gradient initiates from these coarsened equiaxial grains, establishing the Zone 2 microstructure (e.g. Fig. 4.32). The solidification interface development can be followed in the subsequent images shown in Fig. 4.43a. At times from $6.1 \mu\text{s}$ onward the grains composing the interface increase in size considerably and result in reduced in numbers of grains constituting the interface with the liquid. Furthermore the dark contrast at the inter-granular/inter-crystalline regions reduces over time. This would be consistent with an interpretation that invokes the

reasonable scenario of a phase change in these inter-crystalline regions from initially being liquid to solid as the Al solid solution grains at the perimeter of the essentially stagnant melt coarsen. Notably, the PED-OIM studies, (e.g. Fig. 4.35 and 4.36), indicated a scale change for the Al phase grains and a morphological change for the Cu enriched Al_2Cu based phase, which would be consistent with the presence of a liquation zone or mushy zone, where solid Al solid solution grains persist, while being enveloped or partially surrounded by adjacent liquid of elevated Cu content relative to the alloy composition. The latter would have a reduced melting temperature relative to the Al solid solution grains. Upon solidification the PED-OIM data indicated that equilibrium θ -phase had been replaced entirely by the metastable θ' -phase in the inter-granular regions between the Al grains in Zone 2 and parts of the HAZ, as well as in the columnar morphology Al grain matrix and the inter-granular regions in Zone 3 of the solidification microstructure (Fig. 6, 8 and 9). These post-mortem TEM observations would be consistent and supportive of the speculative interpretation offered above for the in-situ DTEM image contrast changes from quite dark to lighter gray for the inter-crystalline regions in the region of the microstructure delineated by the dashed line markers in Fig. 4.43a. Thus, for the 3.3 μ s duration of the DTEM MovieMode series shown in Fig. 4.43a the polycrystalline Al-Cu exhibits an essentially stagnant liquid-solid interface. During this period of time a liquation zone that exists of solid Al solid solution grains and liquid alloy melt enveloping or at least penetrating between them into the polycrystalline aggregate along the intergranular regions gradually reduces in its spatial extent by lateral crystal growth, coarsening of the scale, of the higher melting point Al grains until the appropriate thermal conditions are established for an accelerated rate directional growth of the latter into the bulk liquid of the melt pool. The arrow in Fig. 4.43a marks the approximate location of the average or far-field interface between the bulk liquid of the melt pool and the solid Al-Cu polycrystalline aggregate. The final image frame shown in Fig. 4.43a, label Re-solidified, is a post-solidification 50ns image that clearly indicates that directional crystal growth established the Zone 3 microstructure from the coarsening grains that persisted at the interface with melt pool during the 3.3 μ s duration MovieMode image series (Fig. 4.43a). The larger magnification TEM micrograph shown in Fig. 4.43a illustrates the details of the inter-crystalline contrast in the HAZ (Zone 1, Fig. 4.32) and transition or

occlusion zone (Zone2 in Fig. 4.32) being associated with CU-rich composition phase and the coarsening of the Al solid solution grains that persisted at the stagnant melt pool interface, defining the transition from Zone 2 to Zone 3. The growth mode change from a pro-eutectic growth of Al solid solution and Cu-rich eutectic constituent to an entirely eutectic growth mode is apparent at the top of this panel to the far-right in Fig. 4.43a. The two DTEM MovieMode series shown in Fig. 4.43b have been obtained for a post-melting-pulse delay time consistent with the time associated with the second growth mode transition that had been identified from the velocity analyses of the collated in Fig. 4.42, about 31 μs . The first MovieMode series for between 31 μs and 32 μs and second image series between 32 μs and 33 μs after the sample-drive-laser photon pulse for alloy thin film melting show select bright field images that capture details of the extremely rapid transition from Zone 3 growth mode of columnar morphology, kinetically modified eutectic to the complex growth mode establishing the banded morphology grains in Zone 4 at the very center of the Al-Cu alloy melt pool (Fig. 4.43b). The first image series in Fig. 4.43b shows columnar growing grains that grow anti-parallel to the heat extraction direction. The growth of the columnar grains, identified by the diffraction contrast related elongated features of different orientations, consumes the remaining liquid in the melt-pool with increasing velocity and propagates with an essentially flat, smooth or planar interface morphology (Fig. 4.42). The vertex of the elliptical melt-pool is clearly discernible in the in-situ observations of Fig. 4.43b. Due to the reduced and minimal radius of curvature at the vertex location of the melt-pool, the heat extraction is assumed to be higher in this region. Therefore, columnar morphology grains associated with this location might be favored to reach a composition dependent critical solidification interface velocity and develop interface instabilities. For the location where the absolute stability limit has been reached phase separated crystal growth is kinetically no longer possible and the velocity modified partition coefficient becomes unity. For such grains that have been able to initiate the critical instability partitionless growth of the crystal into the melt can progress at much higher rates that are no longer limited by diffusion in the bulk limit and constitutional effects. Repeating the nominally identical experiment at slightly longer delay time of 32 μs onward captures the growth mode change from Zone 3 to Zone 4, the development of banded region. Some grains reach critical velocity as the liquid ahead of

the interface is sufficiently under-cooled so that fast growing precipitate free bands can wrap around the melt-pool following the isotherms in the cooling melt pool. Effectively the minority of grains that reach the critical velocity will consume the majority of the melt-pool as they are able to occlude the other columnar growing grains. The central region of the former melt pool is composed of a typically less than ten grains, which can be seen, for instance, in the post-mortem BF-STEM image shown in Fig. 4.43b. The post-mortem image shows the banded region with alternating precipitate-free and precipitate-rich bands existing in a single Al matrix grain.

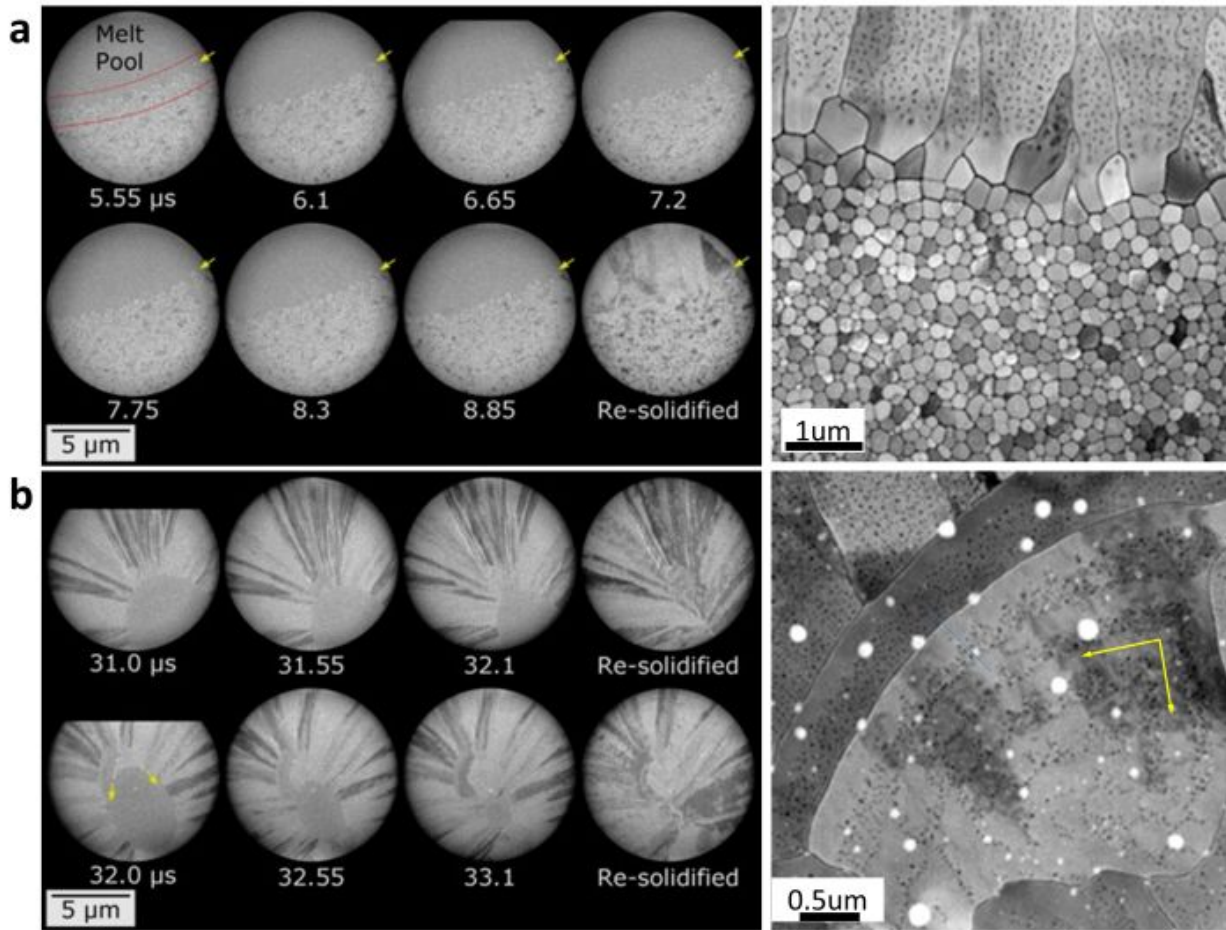


Figure 4.43: High spatio-temporal observations of occurring growth mode changes showing the transition from pro-eutectic α -cell growth into columnar kinetically modified eutectic in **a** and the transition from cellular growth to banded growth in **b**

4.2.6 Summary and Discussion

Hypo-eutectic Al-04 at. %Cu alloy thin films were deposited with a thickness of 80 nm by electron-beam evaporation (Pascal Technologies Dual E-Beam) onto 50 μm thick amorphous supported films of 500 by 500 μm windowed TEM grids (TED Pella Inc.) The alloy thin-films were deposited in high vacuum at a rate of 2-2.5 ms^{-1} with substrates held at 298 K. The as deposited film is composed of θ - and α -phase separated. The overall chemical composition was confirmed with EDS and the thin film show an average composition of 4.1%. Here copper rich clusters coincide with bright contrast features of the ADF STEM images and show elevated concentration of up to 17 at.% Cu which is still significantly lower than what is expected for equilibrium θ -phase. However, due to the precipitates being matrix embedded in the deposited film and also in the RS transformed microstructure, a reduced Cu content in the resultant EDS signal is to be expected, since the point probe (≈ 0.5 nm diameter) electron beam samples the average composition through the entire thin film thickness cross section. With the novel precession electron diffraction technique and the acquired phase- and orientation-maps the starting condition has been confirmed to be composed of nanocrystalline grains that are separated by high angle grain-boundaries and containing θ and α -phase. The Al-04 at. %Cu alloy thin films can be successfully PL irradiated and melted utilizing the in-situ instrument (DTEM) and the ex-situ experimental setup (PITT). The resulting micro-structural features and morphological zones observed are very similar to those reported for bulk CW-laser experiments for Al-base alloys in prior research [49, 50, 51, 52, 53]. The interface velocity dependent growth-modes and associated morphological Zones in Al-04 at. %Cu alloys are summarized as the heat affected zone (HAZ) (1), occlusion zone (2), columnar grown α -cell (3), and banded zone (4). Investigation of the HAZ shows that the grains affected by directional heat flow grow significantly larger (2 times) when subjected to a shallow Gaussian photon distribution field. If the laser pulse is sharply defined the surrounding grains are less subjected to equiaxed growth. The plateau in both grain size plots in Fig. 4.33a and Fig. 4.33b could possibly be related to a liquation zone, in this zone the local temperature due to in-plane heat diffusion might surpass the melting point of the grainboundary θ -phase. The difference in the occlusion zone shown in the annular

dark field STEM images (between yellow and black dashed line) in Fig. 4.33a and Fig. 4.33b are related to the initial interface velocity development. The thermal gradient in the ex-situ experimentation is steeper and thus the interface acceleration is higher allowing for a stronger suppression of the α -liquid phase field. While a slower acceleration which is assumed in the in-situ case leads to an extended occlusion zone and for overall larger morphological features. Further PED investigations of the heat affected zone around 120 μm away from the melt-pool edge show that the inherent $\langle 110 \rangle$ fiber texture is maintained and not change due to laser irradiation and thermal modification of the microstructure. The copper rich grain-boundary phase is composed of θ - and θ -phase indicating that even at a distance of 120 μm a liquid phase might have existed shortly after irradiation. The texture analysis of the HAZ shows the nano-crystalline nature of the HAZ, further it shows that the fiber texture is maintained. PED of the columnar grains in Fig. 4.37, Fig. 4.38, Fig. 4.39 and Fig. 4.40 show orientation relationships between the parent- and second-phase that can be derived from age hardening processes, but further show orientations relationship exists that stem from the rapid crystallization process. Two phases form simultaneously and are a product from rapid solidification. Low spatio temporal resolution experiments successfully demonstrated capturing the entire solidification process, and recording reproducible sub-sequential images and measuring the instantaneous velocity. The velocity development has excellent correlation between growth-mode and growth-mode changes observed. For the Al-04 at. %Cu alloy three distinct growth-modes have been determined. The first initial increase in interface velocity can be explained by the formation of the occlusion zone, initially high interface temperatures allow higher melting temperature α phase to form, as the heat diffusion through the solid is a magnitude higher than the thermal diffusion in the liquid the liquid temperature in front of the interface cools down, allowing for the interface to accelerate while forming α -phase solid with increased amounts of copper until the temperature reaches the eutectic temperature and the first growth mode change occurs. The predicted growth mode should appear after around 500-1000 nm (along minor and major axis). The EDS evaluation in Section 4.2.4 shows that the copper concentration in the α -solid solution reaches ≈ 3.2 at. %Cu and first precipitates start to form. The formed precipitates have an average composition of ≈ 15 at. %Cu surrounded by a saturated α -solid solution matrix (≈ 3.1 at. %Cu). These

non equilibrium phases found in the MS correlate nicely with the increase in the interface velocity. The formation of kinetically modified eutectic, where simultaneously θ - and α -phase crystal growth occurs and establishes the large and precipitate rich columnar growing grains in Zone 3. At first, the interface velocity along the circumference of the melt-pool moves with the same acceleration due to constitutional under-cooling of the liquid and the large heat-sink surrounding the melt pool. However, in the later stages of solidification around 20 μ s the curvature dependent heat extraction of the melt-pool changes where the minor radius shows the lowest and major radius shows the highest heat extraction. This leads to a change in acceleration along the major axis ultimately favoring growth of the grains growing along the major direction to reach the critical velocity for partitionless crystallization first and allowing these grains to change the accessed growth-mode.

High-spatio-temporal-resolution experiments successfully demonstrated capturing the kinematical process, and recording reproducible sub-sequential image series of growth-mode changes occurring in the solidification sequence of Al-04 at. %Cu alloy. Two growth mode changes were captured. Firstly, (1) the change from a stationary interface to an kinematically modified eutectic (α -cell) Fig. 4.43a growth, and secondly (2) the growth mode change towards the banded growth mode morphology Fig. 4.43b. The last growth mode change in Fig. 4.43b (32.0 μ s) shows a potential dendrite tip bulging outwards into the liquid growing roughly parallel to the isotherms (perpendicular to the heat extraction direction) consuming the melt while a parallel kinematically modified eutectic interface forms parallel to the heat extraction direction.

5.0 ACHIEVEMENT AND OUTLOOK

5.1 ACHIEVEMENT

The solidification process of nanocrystalline Al and Al-04at.%Cu alloy thin films has been successfully observed and investigated utilizing the novel DTEM and conventional TEM techniques. The resultant micro-structural morphology has been investigated regarding texture, morphology changes, grain size and grain size development, phase formation and orientations relationships.

An experimental safe zone has been established to provide reproducible pulse laser induced melting and solidification experiments that allow for a 2-D (in-plane) heat extraction. Solidification experiments should be conducted near the center of the electron transparent window, to avoid influences from the surrounding and electron opaque regions of the thin film. Simulations showed that the shallow Gaussian laser pulse should not irradiate the surrounding substrate as the resultant thermal gradient and resultant interface development will be changed. Further, in order to develop simulations of the inter-facial behavior and temperature development reproducibility is of up-most importance.

The high spatio temporal study provided direct local observation of the PL initiated melting event and subsequent columnar crystal growth of pure Aluminum. During the melting event a diminishing mushy zone was observed. In regions that did not fully melt a liquation zone was captured. During the crystallization event a rapidly evolving flat or planar interface was captured. Low spatio temporal observation reproducible captured the melt pool development and were utilized to measure instantaneous and averaged velocities for rapidly solidifying Al. PL irradiation of Al-04Cu samples produced solidification micro-structures and morphologies comparable to bulk CW-laser experiments. Measured instantaneous and

averaged velocities utilizing the low-spatio-temporal-resolution DTEM Movie Mode compare nicely with the inferred velocities studies done on bulk samples utilizing a CW-laser setup. Utilizing the velocity development functions helps predicting growth mode changes and allows for planned experiments. The high-spatio-temporal setup captured the growth mode changes and inter-facial behavior of solidifying Al-04Cu alloys. The transition from a stationary rough interface, towards α -cellular, flat, growth interface (kinetically modified eutectic) was captured. Further, the growth mode change from α -cellular to banded morphology was captured. When favored grains reach the velocity of absolute stability ($v_a \approx 1.5 - 1.7 \text{ms}^{-1}$) they can access a growth mode which denies constitutional arrangement at the interface to form alternating bands of super saturated α -phase, with precipitate rich bands.

Post-mortem results showed a present orientation relationship between the forming precipitates in the columnar growing grains with the parent α -phase to be $[001]_{\theta'} || [110]_{\alpha} + \langle 110 \rangle_{\theta'} || \langle 100 \rangle_{\alpha}$ and $[001]_{\theta'} || [100]_{\alpha} + \langle 100 \rangle_{\theta'} || \langle 100 \rangle_{\alpha}$.

5.2 OUTLOOK

Free standing Al and Al-Cu alloys show very reproducible results during PL initiated rapid solidification experiments because of excellent wetting behavior with the used, 50 nm thin, Si_3N_4 substrate materials. The wetting behavior can attributed to the excellent self passivation behavior of Aluminum. However, other material systems might de-wet during the laser irradiation, effectively rendering the study of solidification impossible. It would be preferable to understand how a potential cap-layer comprised of Si_3N_4 or SiO_2 alter the solidification behavior. Hence, a repeat of the Aluminum solidification experiments utilizing a layered structure of Al + cap layer on Si_3N_4 -substrate would quantify the influence of a cap layer.

BIBLIOGRAPHY

- [1] D.B. Williams and C.B. Carter. The transmission electron microscope. *Transmission Electron Microscopy*, pages 3–22, 2009.
- [2] Thomas LaGrange, Bryan W. Reed, Melissa K. Santala, Joseph T. McKeown, Andreas Kulovits, Jrg M.K. Wiezorek, Liliya Nikolova, Federico Rosei, Bradely J. Siwick, and Geoffrey H. Campbell. Approaches for ultrafast imaging of transient materials processes in the transmission electron microscope. *Micron*, 43(11):1108 – 1120, 2012. *in situ TEM*.
- [3] SL Sobolev. Nonlocal diffusion models: Application to rapid solidification of binary mixtures. *International Journal of Heat and Mass Transfer*, 71:295–302, 2014.
- [4] SL Sobolev. Diffusion-stress coupling in liquid phase during rapid solidification of binary mixtures. *Physics Letters A*, 378(5):475–479, 2014.
- [5] SL Sobolev, LV Poluyanov, and Feng Liu. An analytical model for solute diffusion in multicomponent alloy solidification. *Journal of Crystal Growth*, 395:46–54, 2014.
- [6] Zhaoyang Hou, Zean Tian, Rangsuo Liu, Kejun Dong, and Aibing Yu. Formation mechanism of bulk nanocrystalline aluminium with multiply twinned grains by liquid quenching: A molecular dynamics simulation study. *Computational Materials Science*, 99:256–261, 2015.
- [7] YQ Jiang, P Peng, DD Wen, SC Han, and ZY Hou. A dft study on the heredity-induced coalescence of icosahedral basic clusters in the rapid solidification. *Computational Materials Science*, 99:156–163, 2015.
- [8] A. Kulovits, R. Zhong, JMK Wiezorek, and JP Leonard. Electron microscopy of geometrically confined copper thin films after rapid lateral solidification. *Thin Solid Films*, 517(13):3629–3634, 2009.
- [9] Loren A. Jacobson and Joanna McKittrick. Rapid solidification processing. *Materials Science and Engineering: R: Reports*, 11(8):355 – 408, 1994.

- [10] M Asta, C Beckermann, A Karma, W Kurz, R Napolitano, M Plapp, G Purdy, M Rappaz, and R Trivedi. Solidification microstructures and solid-state parallels: Recent developments, future directions. *Acta Materialia*, 57(4):941–971, 2009.
- [11] J. M. Aziz. Crystal growth and solute trapping. Technical report.
- [12] A. Munitz. Microstructure of Rapidly Solidified Laser Molten Al-4 . 5 Wt Pct Cu Surfaces. *Metallurgical and Materials Transactions A*, 16(March):149–161, 1985.
- [13] W Kurz, B Giov Anola, and R Trivedi. THEORY OF MICROSTRUCTURAL DEVELOPMENT DURING RAPID SOLIDIFICATION. 34(5):823–830, 1986.
- [14] W Kurz, B Giovanola, and R Trivedi. THEORY OF MICROSTRUCTURAL DEVELOPMENT DURING RAPID SOLIDIFICATION. *Acta Metallurgica*, 34(5):823–830, 1986.
- [15] CV Thompson. Structure evolution during processing of polycrystalline films. *Annual review of materials science*, 30(1):159–190, 2000.
- [16] David A Porter, Kenneth E Easterling, and Mohamed Sherif. *Phase Transformations in Metals and Alloys, (Revised Reprint)*. CRC press, 2011.
- [17] Monde A Otoni. *Elements of rapid solidification: fundamentals and applications*. Number 29. Springer Verlag, 1998.
- [18] J.C. Baker and J.W. Cahn. Solute trapping by rapid solidification. *Acta Metallurgica*, 17(5):575–578, 1969. cited By (since 1996)44.
- [19] P.M. Smith and M.J. Aziz. Solute trapping in aluminum alloys. *Acta Metallurgica Et Materialia*, 42(10):3515–3525, 1994. cited By (since 1996)40.
- [20] Riccardo Reitano, Patrick M. Smith, and Michael J. Aziz. Solute trapping of group iii, iv, and v elements in silicon by an aperiodic stepwise growth mechanism. *Journal of Applied Physics*, 76(3):1518–1529, 1994. cited By (since 1996)49.
- [21] J.C. Baker and J.W. Cahn. Solidification. *Solidification*, 1971. cited By (since 1996)82.
- [22] M.J. Aziz and W.J. Boettinger. On the transition from short-range diffusion-limited to collision-limited growth in alloy solidification. *Acta Metallurgica Et Materialia*, 42(2):527–537, 1994. cited By (since 1996)99.
- [23] M.J. Aziz. Interface attachment kinetics in alloy solidification. *Metallurgical and Materials Transactions A: Physical Metallurgy and Materials Science*, 27(3):671–686, 1996. cited By (since 1996)79.
- [24] M.J. Aziz and T. Kaplan. Continuous growth model for interface motion during alloy solidification. *Acta Metallurgica*, 36(8):2335–2347, 1988. cited By (since 1996)171.

- [25] J. Gren. A simplified treatment of the transition from diffusion controlled to diffusion-less growth. *Acta Metallurgica*, 37(1):181–189, 1989. cited By (since 1996)56.
- [26] M. Hillert and B. Sundman. A solute-drag treatment of the transition from diffusion-controlled to diffusionless solidification. *Acta Metallurgica*, 25(1):11–18, 1977. cited By (since 1996)33.
- [27] M. Hillert and B. Sundman. A treatment of the solute drag on moving grain boundaries and phase interfaces in binary alloys. *Acta Metallurgica*, 24(8):731–743, 1976. cited By (since 1996)132.
- [28] Robert W Cahn and Peter Haasen. *Physical Metallurgy*.
- [29] G.J. Galvin, M.O. Thompson, J.W. Mayer, R.B. Hammond, N. Paulter, and P.S. Peercy. Measurement of the velocity of the crystal-liquid interface in pulsed laser annealing of Si. *Physical Review Letters*, 48(1):33–36, 1982. cited By (since 1996)36.
- [30] M.O. Thompson, G.J. Galvin, J.W. Mayer, P.S. Peercy, and R.B. Hammond. Melt dynamics of silicon-on-sapphire during pulsed laser annealing. *Applied Physics Letters*, 42(5):445–447, 1983. cited By (since 1996)6.
- [31] B.C. Larson, J.Z. Tischler, and D.M. Mills. Nanosecond resolution time-resolved x-ray study of silicon during pulsed-laser irradiation. *Journal of Materials Research*, 1(1):144–154, 1986. cited By (since 1996)42.
- [32] M. Zimmermann, M. Carrard, and W. Kurz. Rapid solidification of Al-Cu eutectic alloy by laser remelting. *Acta Metallurgica*, 37(12):3305 – 3313, 1989.
- [33] S C Gill and W Kurz. Rapidly Solidified Al-Cu Alloys 1. 41(12):3563–3573, 1993.
- [34] B.D. Cullity. *Elements of X-ray Diffraction*, 1978. cited By (since 1996) 10558.
- [35] P. Moeck, S. Rouvimov, I. Hausler, W. Neumann, and S. Nicolopoulos. Precession electron diffraction & automated crystallite orientation/phase mapping in a transmission electron microscope. In *Nanotechnology (IEEE-NANO), 2011 11th IEEE Conference on*, pages 754–759. IEEE, 2011.
- [36] Portillo J. Bultreys D. Maniette Y. Nicolopoulos S. Rauch E.F., Veron M. Automatic crystal orientation and phase mapping in TEM by precession diffraction. *Microscopy and Analysis*, (93):S5–S8, 2008. cited By (since 1996) 17.
- [37] K.J. Ganesh and P Ferreira. TEM-OIM - nanocrystalline tungsten. *Microsc. Microanal.*, in press.
- [38] ND Browning, JA Berger, GH Campbell, JS Kim, WE King, T LaGrange, DJ Masiel, BW Reed, WA Schroeder, JC H Spence, ML Taheri, and T Vecchione. Combining spatial and temporal resolution in the dynamic TEM. *Microscopy and Microanalysis*, 13:1154–1155, 8 2007.

- [39] HTG Hentzell, CRM Grovenor, and DA Smith. Grain structure variation with temperature for evaporated metal films. *Journal of Vacuum Science & Technology A*, 2(2):218–219, 1984.
- [40] Andreas Kulovits, Jörg MK Wiezorek, Thomas LaGrange, Bryan W Reed, and Geoffrey H Campbell. Revealing the transient states of rapid solidification in aluminum thin films using ultrafast in situ transmission electron microscopy. *Philosophical Magazine Letters*, 91(4):287–296, 2011.
- [41] BN Chichkov, C Momma, S Nolte, F Von Alvensleben, and A Tünnermann. Femtosecond, picosecond and nanosecond laser ablation of solids. *Applied Physics A*, 63(2):109–115, 1996.
- [42] QS Mei and K Lu. Melting and superheating of crystalline solids: from bulk to nanocrystals. *Progress in Materials Science*, 52(8):1175–1262, 2007.
- [43] YF Zhu, JS Lian, and Q Jiang. Modeling of the melting point, debye temperature, thermal expansion coefficient, and the specific heat of nanostructured materials. *The Journal of Physical Chemistry C*, 113(39):16896–16900, 2009.
- [44] Tomorr Haxhimali, Alain Karma, Frédéric Gonzales, and Michel Rappaz. Orientation selection in dendritic evolution. *Nature materials*, 5(8):660–664, 2006.
- [45] S. Mader and S. Herd. Formation of second phase particles in aluminum-copper alloy films. *Thin Solid Films*, 10(3):377 – 389, 1972.
- [46] Rong Zhong. *Microstructural study of laser-induced rapid lateral solidification of metal thin films*. PhD thesis, University of Pittsburgh, 2010.
- [47] Ian J Polmear. Light alloys- metallurgy of the light metals//((book)). *London and New York, Edward Arnold, 1989, 288*, 1989.
- [48] Terry Frederick Bower. *Dendrite morphology*. PhD thesis, Massachusetts Institute of Technology, 1965.
- [49] M. J. Aziz. Model for solute redistribution during rapid solidification. *Journal of Applied Physics*, 53(2):1158–1168, 1982.
- [50] SC Gill, M Zimmermann, and W Kurz. Laser resolidification of the AlAl 2 Cu eutectic: The coupled zone. *Acta metallurgica et materialia*, 1992.
- [51] S C Gill, M Zimmermann, and W Kurz. LASER RESOLIDIFICATION OF THE Al-Al 2 Cu EUTECTIC : THE COUPLED ZONE. 40, 1992.
- [52] J.A. Kittl, R. Reitano, M.J. Aziz, D.P. Brunco, and M.O. Thompson. Time-resolved temperature measurements during rapid solidification of si-as alloys induced by pulsed-laser melting. *Journal of Applied Physics*, 73(8):3725–3733, 1993. cited By (since 1996)23.

- [53] J.A. Kittl, M.J. Aziz, D.P. Brunco, and M.O. Thompson. Nonequilibrium partitioning during rapid solidification of sias alloys. *Journal of Crystal Growth*, 148(1-2):172–182, 1995. cited By (since 1996)38.